

UC Berkeley

UC Berkeley Electronic Theses and Dissertations

Title

Carbon Nanotube-based MEMS Energy Storage Devices

Permalink

<https://escholarship.org/uc/item/4352c6dr>

Author

Jiang, Yingqi

Publication Date

2011

Peer reviewed|Thesis/dissertation

Carbon Nanotube-based MEMS Energy Storage Devices

By

Yingqi Jiang

A dissertation submitted in partial satisfaction of the

requirements for the degree of

Doctor of Philosophy

in

Engineering- Mechanical Engineering

and the Designated Emphasis

in

Nanoscale Science & Engineering

in the

Graduate Division

of the

University of California, Berkeley

Committee in charge:

Professor Liwei Lin, Chair

Professor Albert P. Pisano

Professor Constance Chang-Hasnain

Fall 2011

Carbon Nanotube-based MEMS Energy Storage Devices

Copyright 2011

Yingqi Jiang

Abstract

Carbon Nanotube-based MEMS Energy Storage Devices

by

Yingqi Jiang

Doctor of Philosophy in Engineering - Mechanical Engineering

and the Designated Emphasis in Nanoscale Science & Engineering

University of California, Berkeley

Professor Liwei Lin, Chair

Carbon nanotube (CNT) forests have been utilized as electrodes in supercapacitors in this work for energy storage applications. High surface area to volume ratio, good electrical conductivity, and low contact resistance to a bottom metal electrode make CNT forests attractive as electrodes in supercapacitors. Several approaches have been investigated to improve the performances such as configurations, power and energy density of CNT-based supercapacitors, including the single layer architecture by utilizing interdigitated finger electrodes, pseudo capacitors based on electroplated nickel nanoparticles, ultra-long and densified CNT forests electrodes.

Vertically aligned CNT forests have been synthesized using the thermal CVD process and their sheet and contact resistances have been characterized with four distinct methods: (1) the transfer length method (TLM), (2) the contact chain method, (3) the Kelvin method, and (4) the four point probe method. Experimental results show that CNT forests of 100 μm in height and 100 μm in width have a sheet resistance of about 100 Ω/\square . The specific contact resistance to a current collector is $5 \times 10^4 \Omega \cdot \mu\text{m}^2$. Consistent results from these methods have been observed and less than 0.9% resistance deviations were measured after two months of open-air storage.

In the first development stage, planar supercapacitors based on CNT forests electrodes with interdigitated finger shapes have been fabricated using a combination of Mo/Al/Fe metal stack layers to achieve dense growth of CNT with low resistance. The specific capacitances of the prototype electrodes were measured to be about 1000 times higher than those made of flat metal electrodes. Furthermore, charging/discharging experiments show over 92% energy storage efficiency and robust cycling stability.

In the second development stage, CNT forests with embedded nickel nanoparticles have been used as electrodes for pseudo supercapacitors. A vacuum infiltration process is used in the electroplating process for the uniform deposition of 30-200nm in diameter nickel nanoparticles within the 80 μm -high CNT forests. The measured specific capacitances are up to one order of

magnitude higher than those CNT forests electrodes without nickel nanoparticles. No visual morphologic change was observed on nanoparticles after 1000 cycles of cyclic voltammetry tests.

In the third development stage, ultra long CNT forests were synthesized using a water-assisted CVD process. Experimental results confirmed the capacitance increments were linearly proportion to the height increase of CNT forests with good long term stability.

In the fourth development stage, a two-stage, self-aligned liquid densification process has applied on CNT forest to shrink the volume of CNT forests electrodes. By combining both mechanical bending and liquid densification, the height of CNT forest shrunk from 320 μm to 21 μm . Experimental results show self-aligned and continuous CNT films with preserved bottom contacts to the conductive metal layer. These densified CNT forests electrodes had similar total capacitances before and after the densification process while the volumetric specific capacitance increased from 1.07F/cm³ to 10.7F/cm³ because of the volume reductions.

Acknowledgements

First of all, I would like to thank my research advisor, Prof. Liwei Lin, for his kindness to recruit me into Linlab in 2006, five-year professional supervision on my research, and thoughtful advice for both my study and my life. At this moment that I am about to finish this thesis, I have still been benefitting from his detailed revisions and insightful comments. I sincerely thank Prof. Lin to influence my life path in a positive way.

I would also like to thank Prof. Albert P. Pisano and Prof. Constance Chang-Hasnain. They taught me in class, sat in my PhD qualification exam, and generously support me on this thesis. Without their helps, I would not have been able to complete my PhD smoothly.

I thank Pengbo Wang, a visiting PhD student from China, who was my research partner for one year. His hard working greatly accelerated the progress of this work. I thank Alina Kozinda, a junior PhD in Linlab, who has joined my work since Pengbo left. As a successor of my project, I give my best wishes. I also thank Qin Zhou, my co-worker in Linlab and the best friend at Berkeley. Discussing with him is always enjoyable and inspires me with new ideas.

I thank all the members in Linlab, and professors, students, and microlab stuffs I met at Berkeley. I sincerely thank them for making my past five years a happy memory.

Finally I would like to thank my wife and my family. No matter what challenge I may face, their support is always unconditional and their confidence on me never fades.

This project is supported in part by the DARPA N/MEMS Fundamentals Program and Siemens Inc.

Contents

| | |
|--|----|
| List of figures | v |
| List of tables | ix |
| Chapter 1 Introduction | |
| 1.1 Carbon nanotube | 1 |
| 1.1.1 Characteristics of CNTs | 1 |
| 1.1.2 CNT synthesis | 3 |
| 1.1.3 CNT major applications | 6 |
| 1.2 Supercapacitor | 6 |
| 1.2.1 Principles of EDLC | 6 |
| 1.2.2 Features and characteristics | 8 |
| 1.3 Electrode materials of supercapacitor | 10 |
| 1.3.1 EDLC | 11 |
| 1.3.2 Metal oxide | 12 |
| 1.4 CNTs as electrodes for supercapacitors | 13 |
| 1.4.1 Energy density | 13 |
| 1.4.2 Power density | 15 |
| 1.5 Motivations and thesis overview | 16 |
| 1.5.1 Motivations | 16 |
| 1.5.2 Thesis overview | 17 |
| References | 18 |
| Chapter 2 Synthesis and characterization of CNT forests | |
| 2.1 CNT synthesis | 24 |
| 2.1.1 Experimental setup | 24 |
| 2.1.2 Process optimization | 25 |
| 2.2 Material Characterization using tape masks | 30 |
| 2.2.1 Background | 30 |
| 2.2.2 Fabrication | 31 |
| 2.2.3 Results and repeatability | 34 |
| 2.3 Material characterization using photo masks | 34 |
| 2.3.1 Design | 35 |
| 2.3.2 Fabrication | 38 |
| 2.3.3 Results and discussions | 39 |
| 2.3.4 Gas sensor demonstration | 42 |

| | |
|--|----|
| References..... | 43 |
| Chapter 3 MEMS CNT supercapacitors | |
| 3.1 Introduction..... | 46 |
| 3.2 CNT growth on conductive substrate | 47 |
| 3.3 Fabrication | 50 |
| 3.3.1 Compatibility of microfabrication | 50 |
| 3.3.2 Fabrication process | 51 |
| 3.4 Results..... | 52 |
| 3.5 Discussions | 55 |
| 3.5.1 Material utilization efficiency..... | 55 |
| 3.5.2 Specific capacitance..... | 55 |
| References..... | 57 |
| Chapter 4 CNT forests with embedded nickel nanoparticles as supercapacitor electrodes | |
| 4.1. Introduction..... | 58 |
| 4.2. CNT functionalization | 59 |
| 4.2.1. Method selection..... | 59 |
| 4.2.2. Vacuum infiltration method..... | 60 |
| 4.3. Design and fabrication | 62 |
| 4.3.1 Full functionalization by electroplating..... | 62 |
| 4.3.2 Effects of electroplating parameters | 64 |
| 4.3.3 New layout and process flow..... | 66 |
| 4.3.4 Functionalized CNT supercapacitors..... | 67 |
| 4.4 Experimental results..... | 68 |
| 4.4.1 Material oxidation..... | 68 |
| 4.4.2 Voltage Sensitivity..... | 69 |
| 4.4.3 Cyclic voltammetry curves | 71 |
| 4.5. Discussions | 72 |
| 4.5.1 Reliability..... | 73 |
| 4.5.2 Preservation of structural shape..... | 74 |
| 4.5.3 Other nanoparticles | 74 |
| References..... | 75 |
| Chapter 5 Ultra long and densified CNT forests electrodes | |
| 5.1 Ultra-long CNT forests | 77 |
| 5.1.1 Motivations | 77 |

| | |
|---|-----|
| 5.1.2 Experimental setup..... | 78 |
| 5.1.3 Process discussions | 79 |
| 5.1.4 Supercapacitor application..... | 80 |
| 5.2 In-situ densification of CNT forest at large area | 81 |
| 5.2.1 Motivations | 81 |
| 5.2.2 Densification process | 82 |
| 5.2.3 Supercapacitor application..... | 86 |
| References..... | 89 |
| Chapter 6 Conclusions and future works | |
| 6.1 Conclusions..... | 91 |
| 6.2 Future directions | 93 |
| 6.2.1 Integration for complete energy storage systems..... | 93 |
| 6.2.2 Flexible energy storage systems | 93 |
| 6.2.3 Three dimensional CNT battery..... | 94 |
| 6.2.4 Applications beyond supercapacitors | 94 |
| References..... | 95 |
| Appendix A CNT forest synthesis platform | |
| A.1 Gases | 96 |
| A.2 Gas control..... | 97 |
| A.3 Thermal furnace and vacuum pumps..... | 97 |
| Appendix B Process flows of CNT supercapacitors | |
| B.1 Pristine CNT electrodes | 99 |
| B.1.1 Process flow | 99 |
| B.1.2 Layout instruction | 100 |
| B.1.3 Wafer dicing guide | 101 |
| B.2 Functionalized CNT electrodes..... | 102 |
| B.2.1 Process flowchart | 102 |
| B.2.2 Parameter settings in e-beam evaporation..... | 103 |
| B.2.3 Wafer instruction and dicing guide | 104 |
| Appendix C Silicon-coated CNT forest using LPCVD | |
| C.1 Deposition on thick CNT forests..... | 105 |
| C.2 Deposition on shallow CNT forests | 107 |

List of figures

| | |
|--|----|
| Figure 1.1. Five allotropes of carbon | 1 |
| Figure 1.2. (A) Conceptual diagram of a single-walled carbon nanotube (SWNT) and (B) a multi-walled carbon nanotube (MWNT)..... | 2 |
| Figure 1.3. Band gap of CNTs calculated with radii less than 15 Å..... | 3 |
| Figure 1.4. (A) The partial electrical breakdown of a MWNT. (B) Images of partially broken MWNTs..... | 3 |
| Figure 1.5. Bulk growth of CNTs using (a) Arc Discharge and (b) Laser Ablation. | 4 |
| Figure 1.6. CVD synthesis of CNTs | 5 |
| Figure 1.7. (a) Tip growth and (b) bottom growth of CNT depending on catalyst locations. (c) Oversized catalyst particle coated with carbon. (d) Catalyst fails to nucleate due to strong interactions between catalyst and substrate..... | 5 |
| Figure 1.8. Schematics of (a) a conventional capacitor and (b) a supercapacitor. (c) The equivalent circuit of a supercapacitor..... | 7 |
| Figure 1.9. Equivalent circuits of a supercapacitor..... | 8 |
| Figure 1.10. A generic plot of specific power (power density) vs. specific energy (energy density) for various power/energy sources..... | 9 |
| Figure 1.11. Taxonomy of supercapacitor electrode material | 10 |
| Figure 1.12. Schematic of activated carbon..... | 12 |
| Figure 1.13. Schematic diagram of pore structures of carbon aerogels..... | 12 |
| Figure 1.14. Mechanism of the redox capacitance of metal oxides in aqueous solution..... | 13 |
| Figure 1.15. The sources of the ESR. | 16 |
| Figure 1.16. Four main development stages of CNT supercapacitors in this thesis work..... | 17 |
| Figure 2.1. Experimental setup for the synthesis of CNT forests..... | 25 |
| Figure 2.2. (a), (b) and (c): top view SEMs of CNT growth samples using 1, 5, and 10nm-thick iron layers as the catalyst, respectively. (d) and (e): close view SEMS of (b) and (c)..... | 26 |
| Figure 2.3. SEM photos showing the results of CNT forests by using a 100nm Al layer..... | 27 |
| Figure 2.4. (a) and (c) are side and top views of CNTs synthesized at 650°C for 10mins. (b) and (d) are side and top views of CNTs synthesized at 720°C for 10mins. | 28 |
| Figure 2.5. Relationship between the heights of the CNT forest versus growth time. A linear relationship is obtained within the process parameters based on the experimental results..... | 29 |
| Figure 2.6. 2µm-thick CNT forest. Height control is realized by growth time. | 29 |

| | |
|---|----|
| Figure 2.7. Fabrication of CNT devices using “tape-mask” method. Yellow color represents 50nm Mo layer, orange color is the Al/Fe bi-layer, and grey color is the tape. | 32 |
| Figure 2.8. Fabricated CNT samples using “tape mask” and the test setup. (a) and (b): CNT resistors with widths of 2mm and 5mm, respectively. | 33 |
| Figure 2.9. Sample repeatability tests using two probe measurement of CNT (5mm case, four samples from different growth batches) | 34 |
| Figure 2.10. Schematic diagram of a testing structure used to characterize the electrical properties of the CNT forest and the demonstrative gas sensing application | 35 |
| Figure 2.11. Device layouts of the four testing designs to characterize the sheet and contact resistances of CNT forests: (a) transfer length method (TLM), (b) contact chain design, (c) Kelvin design, and (d) four-point probe design..... | 36 |
| Figure 2.12. Fabrication process for the CNT forest-based device. | 38 |
| Figure 2.13. Fabricated samples. | 39 |
| Figure 2.14. Experimental results from the four testing designs. | 40 |
| Figure 2.15. Resistance measurement results from initial data and after storage in open-air condition for 2 months. (a) Single-line TLM design; (b) contact chain design. | 42 |
| Figure 2.16. Gas sensing of CNT forest. (a)Homemade test setup, (b) Sensing results with different NH ₃ gas concentrations. | 43 |
| Figure 3.1. Schematic of the planar micro supercapacitor using aligned, 3D CNT forest electrodes..... | 46 |
| Figure 3.2. SEM pictures of interdigital CNT electrodes grown on the Mo/Al/Fe stack layer.. | 49 |
| Figure 3.3. Various patterns of CNT forests..... | 50 |
| Figure 3.4. Fabrication process of the MEMS supercapacitor using as-grown CNT forest electrodes..... | 51 |
| Figure 3.5. Assembled MEMS CNT supercapacitor prototypes. | 52 |
| Figure 3.6. Cyclic voltammetry curves of the samples with (green) and without (red) CNT forests electrodes. Scanning rate is 50mV/sec. | 53 |
| Figure 3.7. Effects of the scanning rate. As the scanning rate increase, the current magnitude increases accordingly..... | 53 |
| Figure 3.8. Chronocoulometry curve of the CNT supercapacitor. | 54 |
| Figure 3.9. Efficiency variation during 10 continuous charge/discharge cycles. | 54 |
| Figure 3.10. CNT Samples used to calculate the mass density. | 56 |
| Figure 4.1. Schematic diagram of a functionalized CNT supercapacitor using CNT forests with embedded nickel nanoparticles as the electrode. | 58 |
| Figure 4.2. CNT forest samples after a conventional nickel electroplating process..... | 59 |
| Figure 4.3. Vacuum infiltration procedure | 60 |

| | |
|---|----|
| Figure 4.4. Experimental setup of the vacuum infiltration system. The right side is the schematic of the left figure. | 60 |
| Figure 4.5. A serial of pictures of the CNT vacuum infiltration process..... | 61 |
| Figure 4.6. Effects of different covering liquids on the vacuum infiltration process.. | 62 |
| Figure 4.7. 150 μ m-long vertically aligned CNTs after the vacuum-assisted electroplating process (4min@ 40 mA/cm ² , room temperature). | 63 |
| Figure 4.8. EDX results of the CNT forests (a) before and (b) after nickel functionalization. (c) & (d) TEMs of the electroplated CNT samples..... | 64 |
| Figure 4.9. Electroplating results using different current density..... | 65 |
| Figure 4.10. Cross section views of nanoparticle size with different deposition time | 66 |
| Figure 4.11. Fabricated MEMS supercapacitors using new layout. | 67 |
| Figure 4.12. Test setup of Ni-electroplated supercapacitors (a) Half-cell, three electrode electrochemical cell setup; (b) electrochemical system, <i>Reference 600</i> (Gamry Instruments, Inc., Warminster, PA).) | 67 |
| Figure 4.13. (a) Nickel oxidation by cyclic voltammetry and (b) a reference test on CNT sample without nickel. | 69 |
| Figure 4.14. CV curves for different tests on the same sample with gradually increased applied voltage | 70 |
| Figure 4.15. Performance of a prototype CNT supercapacitor with embedded nickel nanoparticles..... | 72 |
| Figure 4.16. Rough estimation of the CV curve for capacitance calculation. The inset is figure 4.15(a) as a reference..... | 73 |
| Figure 4.17. SEM of CNT forest with embedded nickel nanoparticles (a) before and (b) after 1000 cycles of CV tests. | 74 |
| Figure 4.18. (a) Dried CNT forest with embedded nickel nanoparticles. (b) Close view SEM photo of the nickel nanoparticles embedded within the CNT forest with high porosity..... | 74 |
| Figure 4.19. Znic-coated CNT forests using vacuum infiltration and electroplating (40mA/cm ² , 2min)..... | 75 |
| Figure 5.1. Schematic of experimental setup for the synthesis of ultra-long CNTs..... | 78 |
| Figure 5.2. Synthesis of ultra-long CNTs. (a) Bulk growth of ultra-long CNTs. (b) CNT “thin walls”; (c) CNT “hairs” (micropillar array). | 79 |
| Figure 5.3. More uniform growth of ultra-long CNTs with and without Mo layer on aged sample. (a) top view. The inset is the schematic diagram of the metal patterns; (b) side view. | 80 |
| Figure 5.4. CNT supercapacitors with short CNT forest (~80 μ m, brown color) and long CNT forest (~300 μ m). The electrolyte is 0.1M KOH solution and scanning rate is 50mV/s. | 80 |

| | | |
|--------------|--|-----|
| Figure 5.5. | Long term (113 cycles) of cyclic voltammetry measurements with minor changes. | 81 |
| Figure 5.6. | Schematic of the two-stage, self-aligned vertical densification process for as grown CNT forests. | 82 |
| Figure 5.7. | Schematic diagrams showing the liquid densification phenomena. | 83 |
| Figure 5.8. | The two-stage, self-aligned vertical densification process for CNT forest on a silicon substrate. | 84 |
| Figure 5.9. | SEM photos of the fabricated CNT forests | 85 |
| Figure 5.10. | (a) and (b) SEM photos showing top views of CNT forest before and after the liquid densification process, respectively. (c) The thickness reduction of CNT forest of pristine CNT forest and after the liquid densification process by using Alcohol and water as the working liquids. | 85 |
| Figure 5.11. | Cyclic voltammetry curves of the supercapacitor samples using as-grown (light color) and densified (dark color) CNT forest samples, respectively. | 87 |
| Figure 5.12. | Charge and discharge characteristics of CNT forest electrodes using as-grown (red color and left Y axis), and densified electrodes (blue color and right Y axis), respectively. | 88 |
| Figure 5.13. | Cyclic tests for a densified CNT forest electrode for a total of 50 cycles. | 89 |
| Figure 6.1. | Schematic diagram of a complete and self-sustainable system using CNT forests electrodes in miniaturized supercapacitors. | 93 |
| Figure 6.2. | Schematic of a flexible CNT supercapacitor | 94 |
| Figure 6.3. | Three-dimensional CNT battery | 94 |
| Figure A.1. | Schematic of a CNT Synthesis System | 96 |
| Figure A.2. | Gases used in the experiments. | 96 |
| Figure A.3. | Two types of flowmeter used in this study | 97 |
| Figure A.4. | Thermal furnace loaded with a 2-inch quartz tube. | 98 |
| Figure A.5. | Sample loading (left) and the grown CNT samples before unloading (right) | 98 |
| Figure A.6. | Vacuum pump to purge the tube | 98 |
| Figure B.1. | Layout of CNT supercapacitors on the first development stage | 100 |
| Figure B.2. | Dicing guide of MEMS supercapacitors using pristine CNTs (the 1 st stage) | 101 |
| Figure B.3. | Layout overview of MEMS supercapacitor using functionalized CNTs | 104 |
| Figure C.1. | Silicon-coated 60 μ m-high CNT forest | 106 |
| Figure C.2. | Poly-Si thickness tuning by changing the deposition time | 107 |

List of tables

| | |
|---|-----|
| Table 1.1. Comparison chart of storage components..... | 9 |
| Table 1.2. Comparison between aqueous, organic, and ionic liquid electrolytes..... | 10 |
| Table 1.3. Typical specific capacitances of electrode materials of supercapacitors..... | 11 |
| Table 1.4. Comparison of activated carbon, carbon aerogels, and carbon nanotube forest..... | 14 |
| Table 1.5. Overview of the four key development stages of CNT supercapacitors | 18 |
| Table 2.1. General protocol for the synthesis of CNT forests | 25 |
| Table 2.2. Measurements for CNT samples made by the “tape mask” method. | 33 |
| Table 2.3. Overview of experimental results from tape mask methods..... | 34 |
| Table 2.4. Summary of the calculated results of the four designs. | 41 |
| Table 3.1. Synthesis of CNT forests on different metal substrates..... | 48 |
| Table 3.2. Density calculation of CNT forests | 56 |
| Table 5.1. Standard protocol for water-assisted ultra long CNT growth..... | 78 |
| Table B.1. Constant settings used in e-beam evaporation | 103 |

Chapter 1 Introduction

This chapter introduces synthesis mechanisms and material properties of CNTs and their possible applications as the electrodes in supercapacitors. The principles, features, and electrochemical reactions of supercapacitors are also presented. At the end of the chapter, the motivations of the study and the organization of this dissertation are presented.

1.1 Carbon nanotube

1.1.1 Characteristics of CNTs

Carbon nanotubes (CNTs) are allotropes of carbon with a cylindrical nanostructure [1]. Figure 1.1 lists the common allotropes of carbon structures. The name of nanotube comes from their long, hollow structure with the walls formed by rolled-up sheets of graphene (one-atom-thick hexagonal carbon monolayer). The ends of a nanotube may be capped with a hemisphere of the buckyball structure. The combination of the rolling angle (called "chirality") and radius determines the nanotube properties. CNTs have outstanding material properties. For example, they are stronger than steel, lighter than aluminum, more conducting than copper, better heat conductive than diamond, and very sensitive to the environment [2]

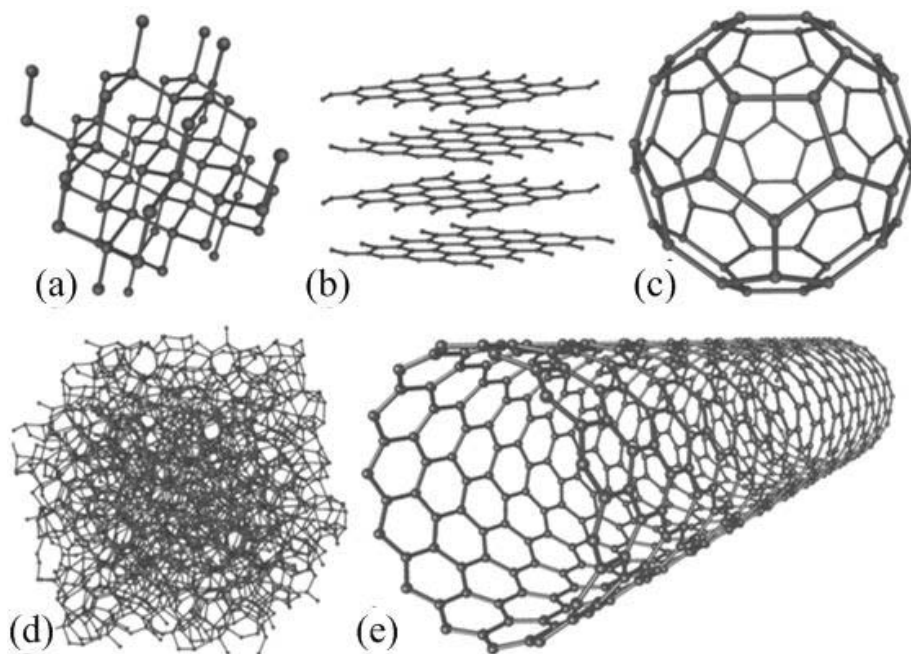


Figure 1.1. Five allotropes of carbon: (a) Diamond, three dimensional (b) Graphite, two dimensional, (d) C_{60} (Buckminsterfullerene or buckyball), zero dimensional, (d) Amorphous carbon, and (e) single-walled carbon nanotube or buckytube, one dimensional. (Adapted from [3])

There are two different forms of CNTs as shown in figure 1.2: the single-walled carbon nanotubes (SWNTs) and multi-walled carbon nanotubes (MWNTs). A SWNT is essentially a single seamlessly rolled-up graphene cylinder; a MWNT, on the other hand, is formed by

multiple concentrically-arranged graphene cylinders. The interlayer distance in MWNTs is close to the distance between graphene layers in graphite, approximately 3.6 Å [4].

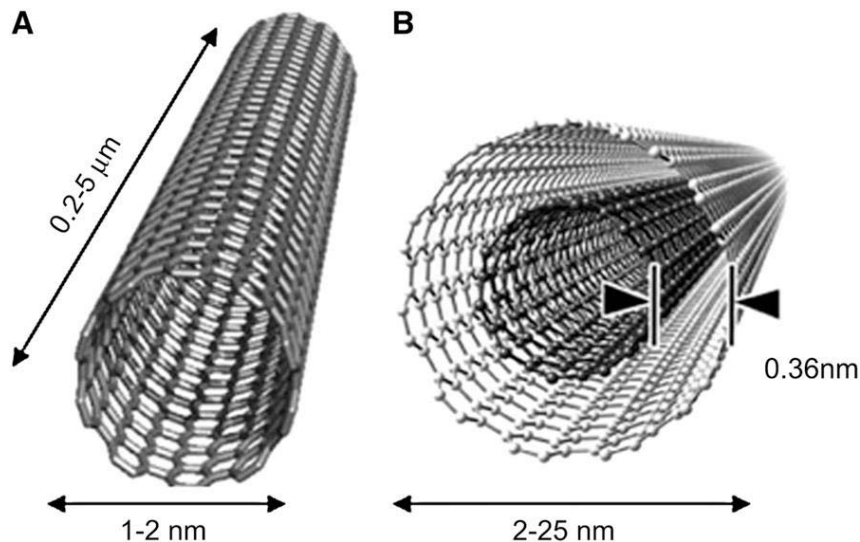


Figure 1.2. (A) Conceptual diagram of a single-walled carbon nanotube (SWNT) and (B) a multi-walled carbon nanotube (MWNT). [4]

SWNT is a true 1D-dimension nanomaterial with a diameter of usually 1-2nm. Depending on how it is rolled (“chirality”); their electrical conductivity can be metallic or semiconducting. Semiconducting property is particularly attractive as it can be the foundation of a FET (field effect transistor) similar to those constructed using silicon [5, 6]. With a diameter of close to 1 nanometer, SWNTs easily can outperform the state-of-arts Si-based FETs (22nm in 2011 and 11nm in 2015 [7]). Thanks to the existence of bang gap, the sensitivity of SWNTs to external stimulus is higher than MWNTs for sensing applications. However, there is currently no known technology on how to grow pure CNTs, how to control their diameter, chirality, and assembly processes consistently.

MWNTs can be seen as a miniaturized “graphite rob” with minimal or zero band gap. As shown in figure 1.3, when the diameter of CNTs is larger than 2nm, the effective band gap will be merely 0.2eV. The metallic shells can electrically short semiconducting ones such that MWNTs don’t have semiconducting behavior. Small diameter of 5-30nm and chemical inertness make MWNTs ideal as conductive electrodes or templates. Multiple concentrically-arranged carbon cylinders make them superior in mechanical and thermal properties. They also carry a higher current density than SWNTs. As shown in figure 1.4, the partial electrical breakdown of a MWNT (corresponding to the loss of individual carbon shells from the MWNT) led to equally-spaced current drop. MWNTs are selected in this investigation as the electrode materials for supercapacitors due to their high current carrying capability, metallic property and easiness in the synthesis processes,

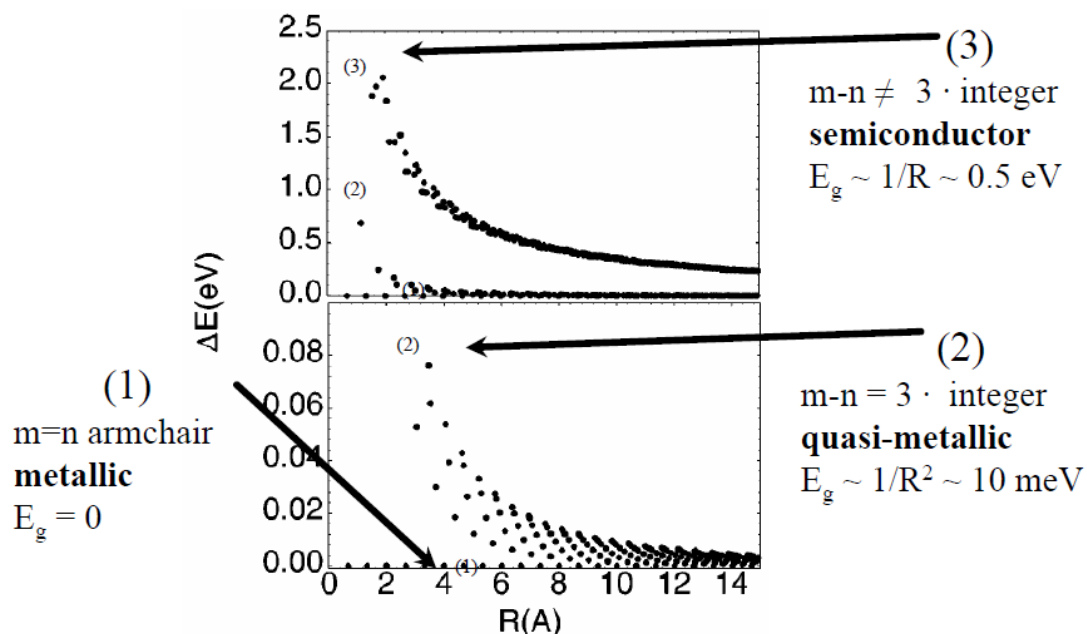


Figure 1.3. Band gap of CNTs calculated with radii less than 15 Å [8] and “m” and “n” in the figure refer to the chirality of CNTs.

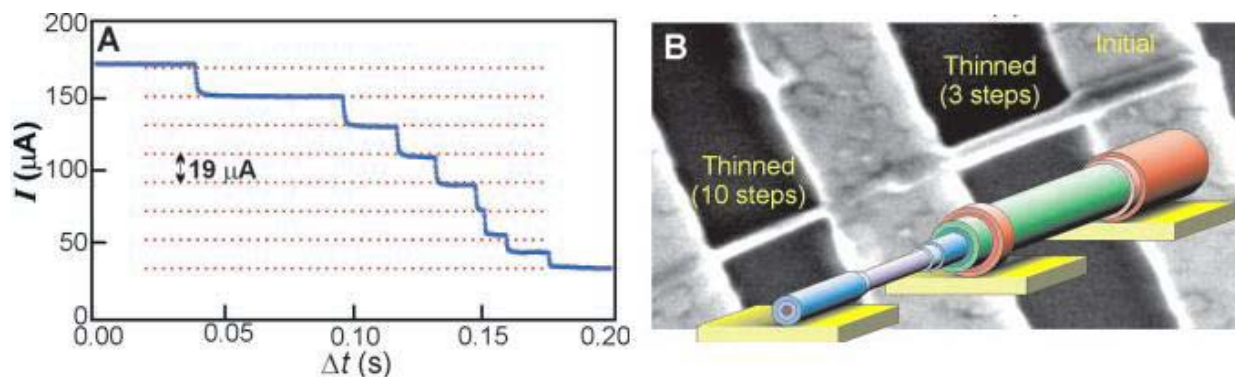


Figure 1.4. (A) The partial electrical breakdown of a MWNT at constant voltage stress proceeds in a series of discrete steps corresponding to the loss of individual carbon shells from the MWNT. Equally spaced dotted lines emphasize the surprisingly regular spacing. (B) Images of partially broken MWNTs show clear thinning, with a decrease in radius equal to the intershell spacing (0.34 nm) times the number of completed breakdown steps. [9]

1.1.2 CNT synthesis

The state-of-art major CNT growth methods are illustrated in figure 1.5 and they include: bulk growth by using arc discharge or laser ablation; and surface growth by means of chemical vapor deposition (CVD). The arc discharge setup is composed of two graphite rods placed at millimeter distance and a high amperage DC supply. During the process, high current flows through the two rods, causing an electrical arc, which vaporizes carbon atoms into plasma format. When the plasma is cooled, carbon atoms will condense into carbon nanotubes at catalyst sites. In the laser ablation process, the mechanism is similar while the heat source of carbon gasification does not come from an electric arc but a laser pulse fired at a graphite target heated

at a temperature of 1200°C. The graphite contains a small amount of catalyst (Co or Ni) to help the carbon transformed into CNTs. Bulk growth is good at producing large quantity of CNTs that could be used for bulk composites, gas storage, etc. The CNT products, however, can be both MWNTs and SWNTs with random orientations. Also, there are by-products such as amorphous carbon within CNTs. As a result, the products need to be cleaned, dispersed and purified before usage. Notably, both methods require high temperature to vaporize the solid carbon precursors into gas format.

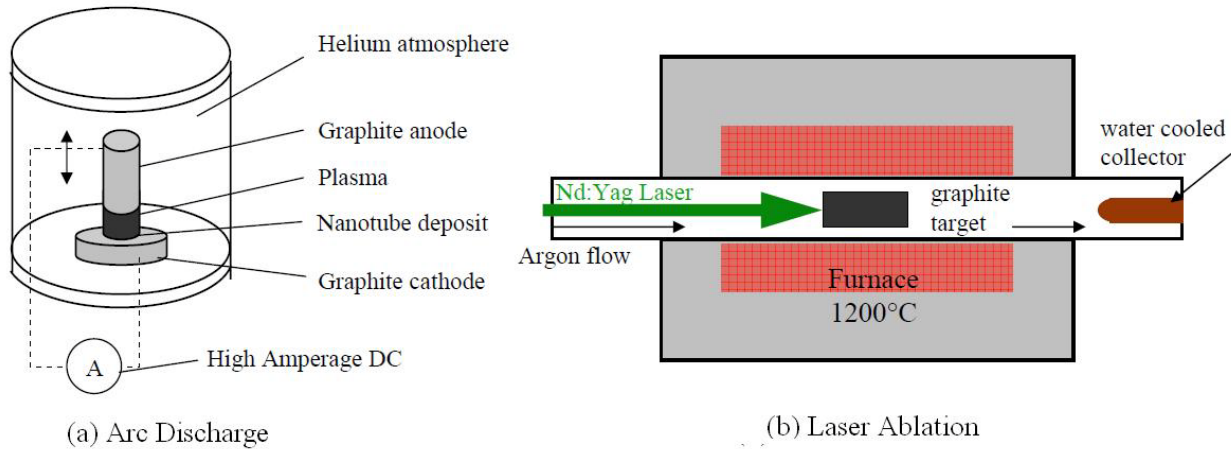


Figure 1.5. Bulk growth of CNTs using (a) Arc Discharge and (b) Laser Ablation. [2]

Chemical Vapor Deposition (CVD) method uses carbon gas precursor to generate CNTs. The process is much more controllable and requires relatively lower synthesis temperature (400-900°C). The CVD process is based on a VLS (vapor-liquid-solid) mechanism with the following eight steps as shown in figure 1.6: (a) deposition of a thin catalyst layer (e.g. 5nm Fe) on substrate (e.g. SiO₂, Al₂O₃); (b) melting and nucleation of catalysts into nanoparticles on heated substrate (e.g. at 700-900°C); (c) absorption of hydrocarbon molecules (C₂H₂ in the figure) onto the catalyst surface; (d) dissociation of hydrogen atoms from the hydrocarbon molecules and the diffusion of carbon atoms into the catalyst; (e) replications of steps (c) & (d) for the super-saturation of carbon atoms in the catalyst nanoparticles; (f) precipitation of carbon atoms from the catalyst and solidification to the lowest energy status — carbon nanotube; (g) formation of hollow nanotube as no carbon precipitates directly under the catalyst; and (h) higher carbon nanotubes as the result of longer synthesis time.

When many CNTs grow together simultaneously, they intertwine with each other and form vertically self-aligned CNT array, called “CNT forests” in this work. The best way to explain why CNTs could be “automatically aligned” is to imagine the scene where a person sits on the deck of a crowded bus. If other people have occupied the surrounding, that person can neither lean forward or backward but only stand up straightly. The same is true for each CNT. While the growth itself tends to be random, the nearby constrains from other CNTs force the individual CNT to grow in the vertical direction.

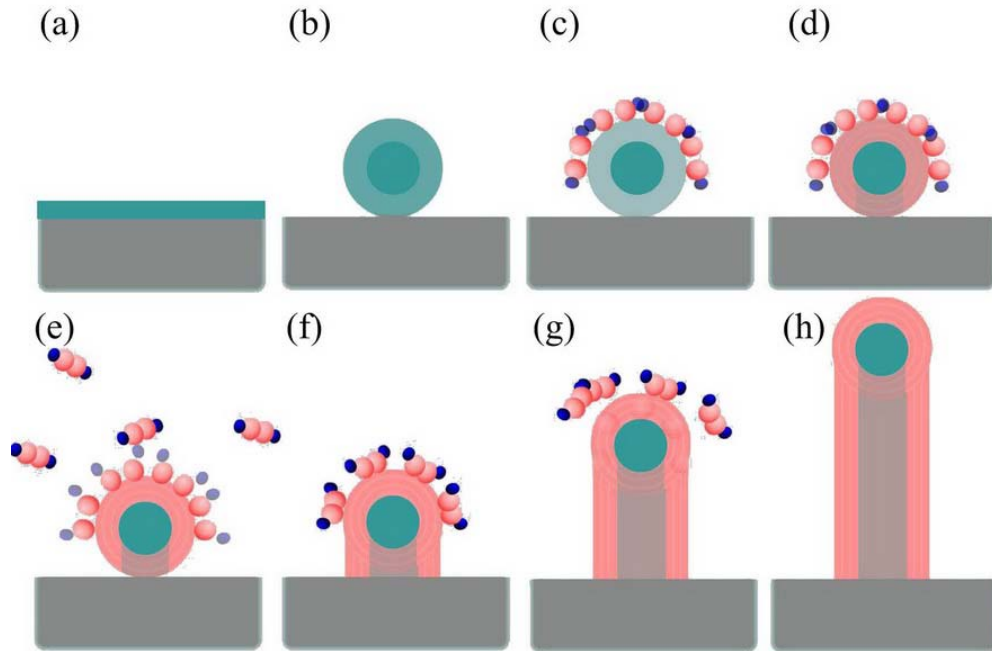


Figure 1.6. CVD synthesis of CNTs. A tip growth is assumed. (Captured and adapted from animation [10])

In the above procedure, it is imaginable that the CVD synthesis of CNTs is influenced mainly by three parameters: 1. materials such as catalyst (type, purity, thickness) and substrate (interaction force between catalyst and substrate); 2. carbon precursor: source gas type (e.g. CH_4 requires higher synthesis temperature since CH_4 has higher decomposition temperature than C_2H_4 and C_2H_2); and 3. synthesis parameters, such as temperature, gas ratio, velocity, and growth time. Detailed optimization procedure of MWNTs used in this study can be found in Chapter 2.

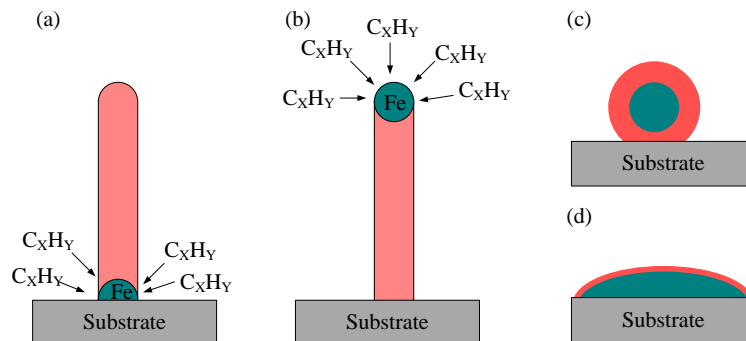


Figure 1.7. (a) Tip growth and (b) bottom growth of CNT depending on catalyst locations. (c) Oversized catalyst particle coated with carbon. Carbon stays on the surface after precipitation such that it blocks the carbon precursor from reaching the catalyst thus stop the growth. (d) Catalyst fails to nucleate due to strong interactions between catalyst and substrate. In both (c) and (d), no CNTs would grow.

The procedures illustrated in figure 1.6 are based on the tip growth mechanism, where a catalyst stays at the tip of the growing CNTs. Another possible growth type is called bottom growth, where the catalyst stays on the substrate throughout the procedure with a carbon dome cap at the tip. These two growth mechanisms are illustrated in figure 1.7. Whether a tip growth or a bottom growth would happen depend on many factors and somehow still under debate [11, 12]. The

common agreement is that, if the substrate interacts strongly with the catalyst, the bottom growth would probably happen and if the interaction between substrate and catalyst is weak, a tip growth would happen [13]. An improper substrate-catalyst relation may cause failures of CNT growth. When the substrate-catalyst interaction is weak as shown in figure 1.7(c), catalyst would nucleate into oversized particles such that CNTs could not grow out of them. In this case, carbon nanofibers (CNF, with a diameter of about 100nm and filled with carbon internally instead of on the surface) and amorphous carbon could form. On the other hand, if the substrate-catalyst interaction is strong as shown in figure 1.7(d), the catalyst may not nucleate at all. In either case, no CNTs would grow.

1.1.3 CNT major applications

CNTs are probably the most studied nanomaterials so far, and have broad practical and fundamental applications due to their excellent characteristics such as high surface area to volume ratio, semiconducting property (SWNT), high sensitivity, nanometer dimension, outstanding mechanical and thermal properties and self-aligned structure (for CNT forest). Some representative applications are listed below.

- Biological applications: DNA detection [14, 15], protein detection [16, 17] and drug delivery [18-20];
- Energy application: supercapacitors[21,] batteries [22], and fuel cell catalyst loading [23]
- Electronics: CNT-FET [24, 25], thin film transistor [26, 27]; CMOS via connections [28, 29],
- Sensor: resistive sensor [30, 31], captivate gas sensor [32], gas ionization sensors [33], humidity sensor [34]
- Optical applications: near-infrared optical sensors [35. 36], field emission devices [37, 38]
- Electrodes: neuron probes [39, 40], electrochemical probes [41, 42].
- Mechanical applications: composite reinforcements [43, 44]; nanoscale actuators [45, 46]
- Thermal applications: chip cooling [47]
- MEMS applications: high aspect ratio building material [48, 49], e.g. RF resonators [50]

1.2 Supercapacitor

1.2.1 Principles of EDLC

A supercapacitor is an energy storage device based on the phenomenon called electrochemical double layer capacitor (EDLC) [51]. Similar to a conventional capacitor, a supercapacitor has a sandwich-shape configuration: two electrodes and a middle layer. However, a close view shows their differences as shown in Figure 1.8.

A conventional capacitor is usually constructed by two flat electrodes and an insulating dielectric layer (such as SiO₂, Al₂O₃) in the middle. The capacitance is determined by:

$$C = \frac{\epsilon A_s}{d} \quad (1-1)$$

Where ϵ is the dielectric constant (also called permittivity) of the middle insulating material; A_s is the physical area of the electrode and d is the physical distance between the two electrodes. A supercapacitor is constructed similarly with a sandwich configuration. However, supercapacitors use highly porous materials such as activated carbon and carbon nanotubes as the electrode material. For the middle layer, supercapacitors use ion-conductive electrolytes. Therefore, there is ionic current flowing through the middle layer during the charge and discharge processes.

For a supercapacitor, when an external power is applied, the electrical field built up between two electrodes acts on ions in the electrolyte. As a result, the positive and negative ions separate from each other and migrate towards corresponding electrodes under the electrostatic force. When ions reach the surface, they, together with the opposite charges (electrons/holes) in the electrodes, form the electric chemical double layer. It is noted that the charges in the electrodes do not go across the interface to meet with ions (actually there is a neutral space called *Stern layer* between the two types of charges [52]). The whole procedure is a pure physical change. Furthermore, this mechanism is based on surface area instead of physical area. That is, for the same physical area, if the surface is rough, which increases the surface area, it would allow more charge to be stored than a flat surface. Therefore, a highly porous and conductive material is more favorable as a supercapacitor electrode. In figure 1.8(b), a separator layer is also used which functions similar to the proton exchange membrane in fuel cells: it blocks electrons from going through but permit ions to penetrate such that it prevents physical contact (electrical short) of the two electrodes while causing little interference on the ion transfer.

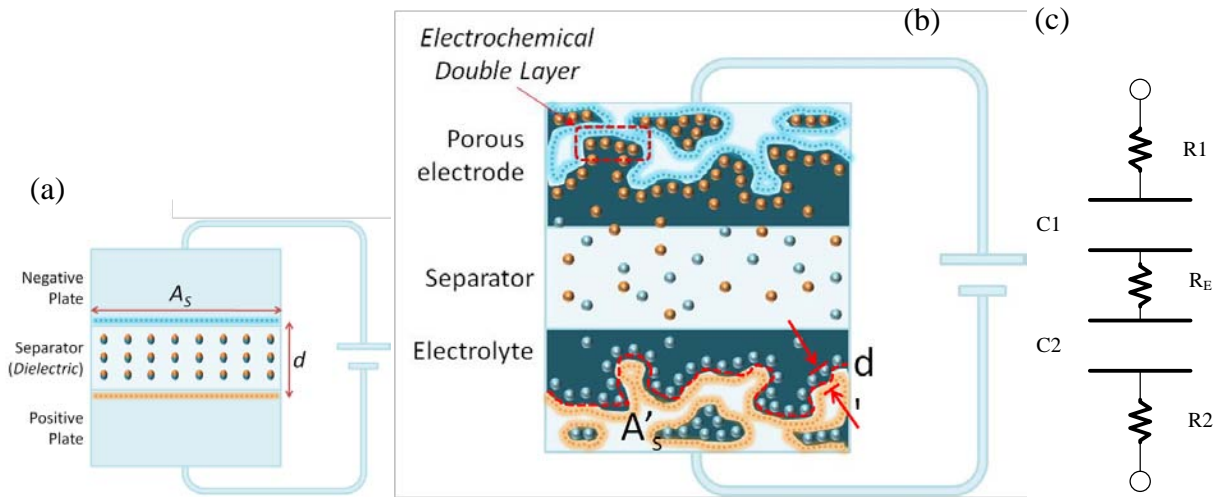


Figure 1.8. Schematics of (a) a conventional capacitor and (b) a supercapacitor. Both symbols of (A_s , d) and (A'_s , d') are used to calculate the capacitances of a capacitor and a supercapacitor, respectively. In a capacitor, A_s is the physical area and d is the physical separation distance between two electrodes; in a supercapacitor, A'_s is the surface area of the electrode, which is much larger than the physical area for a porous electrode, and d' is the distance between charges in electrolyte and those in electrodes. The physical distance of the two electrodes of a supercapacitor only affects the internal resistance and not the capacitance. (c) The equivalent circuit of a supercapacitor. An EDLC exist between the electrolyte and each of the two electrodes. Therefore, there are actually two EDLCs, C_1 and C_2 , within a supercapacitor. R_1 and R_2 correspond to the internal resistances caused by the two electrodes, respectively. R_E is the resistance contributed by the electrolyte and ion diffusion resistance within pores.

The capacitance of a supercapacitor is calculated using the same equation 1-1. However, the surface area (A'_s) and the distance between charges in the electrode and the electrolyte (d') are

used. Based on the above explanation, we can draw the equivalent circuit of a supercapacitor as shown in figure 1.8(c). The measured capacitance, C_{Total} is determined by:

$$\frac{1}{C_{Total}} = \frac{1}{C_1} + \frac{1}{C_2} \quad (1-2)$$

For most cases where the supercapacitor has a symmetric structure ($C_1=C_2$), the above equation can be simplified as:

$$C_{Total} = \frac{C_1}{2} \quad (1-3)$$

The resistances in the equivalent circuit come from electrodes and electrolyte.

To further model a supercapacitor with more conditions, the equivalent circuits in figure 1.9 are often used. Figure 1.9(a) is mostly used for theoretical calculation and analysis. “ESR” is the “equivalent serial resistance” and its value is essentially “ $R_1+R_E+R_2$ ” in figure 1.8(c). In figure 1.9(b), an equivalent parallel resistance (EPR) is added to take the leakage into consideration. EPR is usually very large and can be ignored for transient analysis. It is, however, crucial when long-term energy storage performance is a concern. A more accurate model is shown in figure 1.9(c). Other equivalent circuits also exist and the differences mostly come from simulation interests [54].

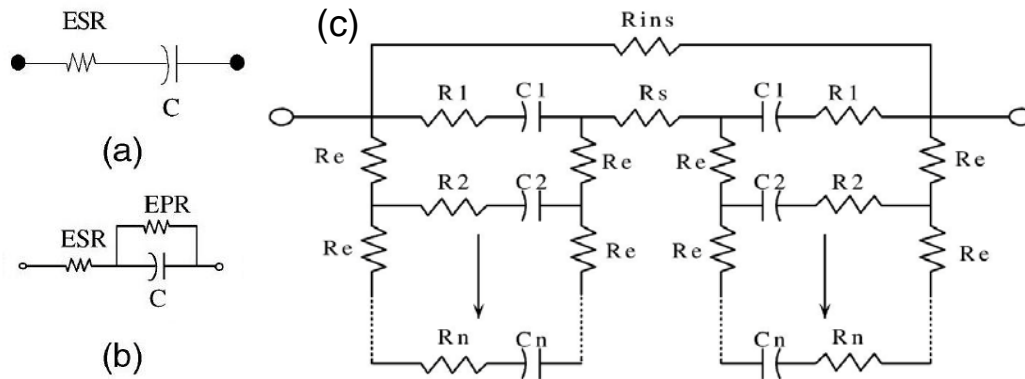


Figure 1.9. Equivalent circuits of a supercapacitor. ESR=equivalent serial resistance. EPR=equivalent parallel resistance. (a) and (b) are simplified and (c) is a distributed model. [53]

1.2.2 Features and characteristics

A general comparison between supercapacitors and common power sources are shown in figure 1.10. It is seen that supercapacitors cover the gap between a conventional capacitor (high power density but low energy density) and a battery (high energy density but low power density).

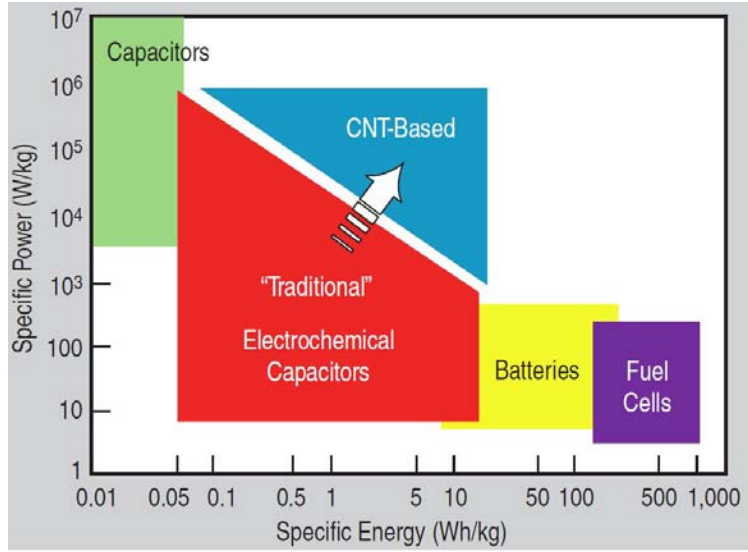


Figure 1.10. A generic plot of specific power (power density) vs. specific energy (energy density) for various power/energy sources [55].

Compared to conventional capacitors, supercapacitors rely on surface area rather than physical area so they have larger capacitances and energy density than conventional capacitors. On the other hand, unlike batteries with complex chemical reactions, supercapacitors store energy by charge movements on the interface between the electrodes and the electrolyte. In other words, the charges can be quickly stored and released, leading to high power density. As a result, supercapacitors have some advantages over other energy sources such as high efficiency (nearly 100%), long cycle life (million times), simple structure, and good stability. A detailed comparison between supercapacitors and common power sources is listed in table 1.1.

Table 1.1. Comparison chart of storage components [56]

| | Capacitors | Super-capacitor | Batteries |
|--------------------------|-----------------------|-----------------|-------------|
| Energy density [Wh/kg] | 0.1 | 3 | 100 |
| Power density [W/kg] | 10^7 | 3000 | 100 |
| Time of charge | $10^{-3} - 10^{-6} s$ | 0.3-30s | >0.3hr |
| Time of discharge | $10^{-3} - 10^{-6} s$ | 0.3-30s | 0.3hr - 3hr |
| Cyclability | 10^{10} | 10^6 | 10^3 |
| Typical lifetime [years] | 30 | 30 | 5 |
| Efficiency [%] | >95 | 85 - 98 | 70 - 85 |

The performance of a supercapacitor is directly related to the material choices of electrode and electrolyte. Generally speaking, electrolyte with high maximum tolerable (decomposition) voltage, good ionic conductivity, and good thermal stability are preferred for supercapacitors. The key differences between common electrolyte materials are listed in table 1.2.

Table 1.2. Comparison between aqueous, organic, and ionic liquid electrolytes [57]

| Property | Aqueous | Organic* | Ionic Liquid |
|-------------------------------------|------------------------|--------------------------|---------------------------|
| Ionic conductivity | 10^{-2} S/cm | 10^{-3} S/cm | 10^{-3} S/cm |
| Electrochemical window | 1 ~ 1.5 V | 3 ~ 4 V | > 5 V |
| Vapor pressure at 25 ⁰ C | 23.8 (mm Hg) | >80 (mm Hg) | Negligible |
| Volatility | High | High | Negligible |
| Viscosity | Low (1 cP) | Medium (< 6 cP) | High (>30 cP) |
| Flammability | Non-flammable | Flammable | Non-flammable |
| Thermal stability | Poor | Poor | Excellent |
| Liquid range | 0 ~ 100 ⁰ C | -55 ~ 240 ⁰ C | -100 ~ 500 ⁰ C |

*propylene carbonate as the example

1.3 Electrode materials of supercapacitor

Electrodes of supercapacitors can be made from a variety of materials. A hierarchical review on common types is shown in figure 1.11. The two common categories are: (1) Electrochemical Double Layer Capacitors (EDLC) made of pure carbon material, such as activated carbon, carbon aerogels, and carbon nanotubes and (2) pseudo-capacitors made of functionalized materials, mostly metal oxides and conducting polymer. Recently, a hybrid supercapacitor, a combination of (1) and (2) have been developed. The typical performances of different electrode materials are summarized in table 1.3.

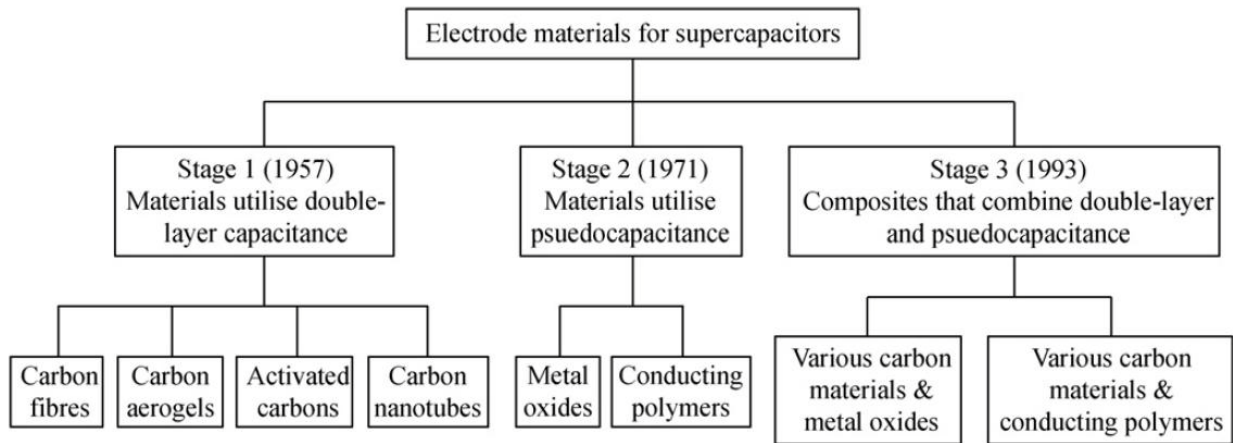


Figure 1.11. Taxonomy of supercapacitor electrode material [58]

Table 1.3. Typical specific capacitances of electrode materials of supercapacitors [57]

| Electrode Material | Specific Capacitance (F/g) |
|--|----------------------------|
| Graphite paper | 0.13 |
| Carbon cloth | 35 |
| Aerogel carbon | 30-40 |
| Activated carbon | 30-100 |
| Cellulose-based foamed carbon | 70-180 |
| RuO ₂ | 380 |
| RuO ₂ hydrate | 760 |
| Conducting polymers (e.g. polyaniline) | 400-500 |

1.3.1 EDLC

Carbon is the most common electrode material for supercapacitors because of its outstanding material characteristics such as high conductivity, electrochemical inertness, and abundance [59, 60]. Furthermore, carbon can be readily transformed into a new form with high specific surface-area. The process used to increase surface area, or, porosity, from a carbonized organic precursor is referred to as “activation” and the resulting broad group of materials is referred to as “activated carbons.” Before activation, solid carbon precursors usually have a low porosity and their structure is composed of elementary crystallites with a large number of interstices between them. The interstices tend to be filled with disorganized carbon residues that block the pore entrances. The purpose of activation is to open these pores and also to create additional porosity. There are a variety of procedures to activate the chars and the results (porosity, pore size distribution, and the nature of the internal surface) vary a lot according to the carbon precursor and activation conditions (e.g. temperature, time and gaseous environment). The activation processes can be sorted into two general categories: thermal activation and chemical activation.

Thermal activation modify the carbon char by controlled gasification and is often carried out at temperatures between 700-1100°C in the presence of suitable oxidizing gases. During gasification, the oxidizing atmosphere increases the pore volume and surface area of the material through a controlled carbon “burn-off” and the elimination of volatile pyrolysis products. Chemical activation is carried out at slightly lower temperatures (400-700°C) and involves the dehydrating action of certain agents such as phosphoric acid and potassium hydroxide. Post-activating washing is usually needed to remove residual reactants as well as inorganic residue. Figure 1.12 shows a schematic of activated carbon. There are three types of pore size within activated carbon: (1) micropore with pore size of less than 2nm; (2) mesopores with pore size of greater than 2nm but less than 50nm; and (3) macropores with pore size of greater than 50nm. As common electrolyte ions have a size about 2nm or above, micropores tend to be too small for ions to diffuse in and out. As a result, micropores are not useful to generate EDLC, although they dominate the surface-area measurements [51].

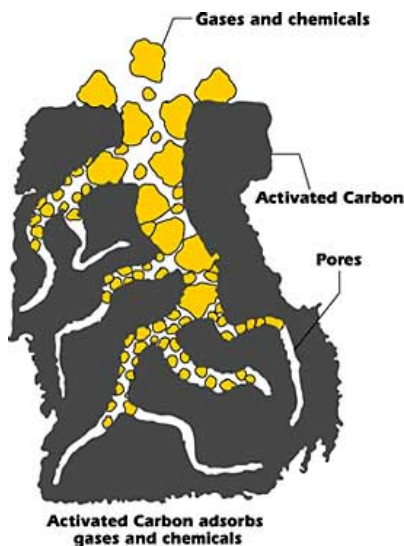


Figure 1.12. Schematic of activated carbon [61]. There are three types of pores within activated carbon: micropores (pore size $<2\text{nm}$), mesopores ($2\text{nm}<\text{pore size}<50\text{nm}$), and macropore (pore size $>50\text{nm}$). Micropores are too small for electrolytic ions to diffusion in and out; therefore they do not contribute to the EDLC.

Carbon aerogels are another commonly-used electrode material. They are usually synthesized by the poly-condensation of resorcinol and formaldehyde via a sol-gel process and subsequent pyrolysis. The schematic is shown in figure 1.13. By varying the conditions of the sol-gel process, the macroscopic properties of aerogels (density, pore size and shape) can be controlled. The aerogel solid matrix is composed of interconnected colloidal like carbon particles or polymeric chains. After pyrolysis, the resulting carbon aerogels are more electrically conductive than most activated carbon [62].

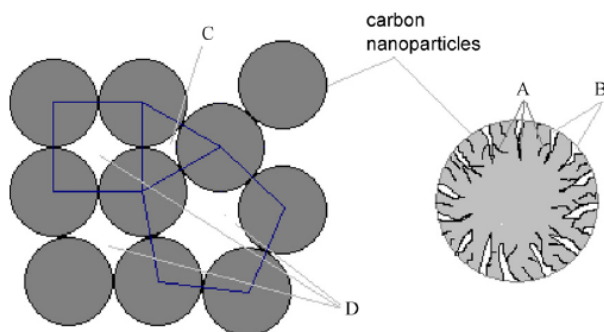
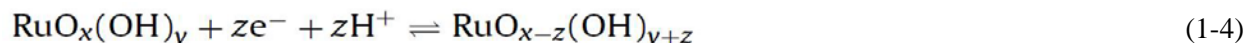


Figure 1.13. Schematic diagram of pore structures of carbon aerogels [62]. The left figure show carbon aerogels is full of carbon nanoparticles. Within each nanoparticle, as shown in the right figure, there are (A) micropores and (B) mesopores. There are also (C) large mesopores formed from the closely packed carbon nanoparticles and (D) large macropores and channels formed from the loosely packed carbon nanoparticles.

1.3.2 Metal oxide

Metal oxides or hydroxides are a family of capacitive materials used in supercapacitors, of which all exhibit redox active behaviors, giving rise to pseudo capacitance [63]. Ruthenium oxide has been studied widely since first reported as a new electrode material in 1971 [64-66].

The pseudo-capacitance of a RuO₂ electrode is caused by highly reversible redox reactions in aqueous media (Ru²⁺, Ru³⁺, and Ru⁴⁺ couples) [65]:



The RuO₂ surface is covered with a carpet of OH-groups by dissociative adsorption of water, as proposed in Figure 1.14. During anodic charging, protons are displaced from the OH sites, and oxide sites are formed.

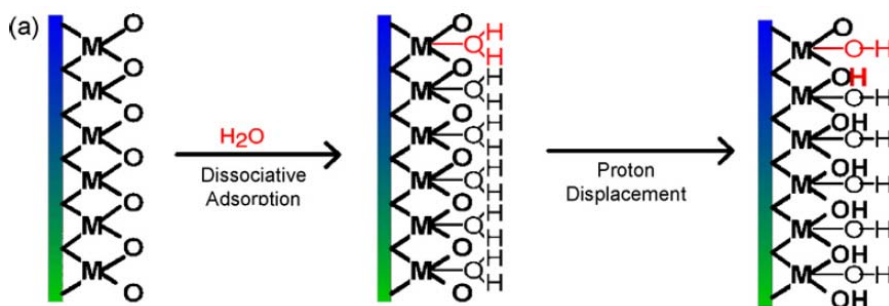


Figure 1.14. Mechanism of the redox capacitance of metal oxides in aqueous solution [65]

The fundamental difference between an EDLC and a pseudo-capacitor lies on whether the charges go through the interface between electrodes and electrolyte. There are two types of current flow in an electrochemical cell [67]. Charges transferring through the electrified interface as a result of an electrochemical reaction are called faradaic current. Non-faradaic current, on the other hand, is the result of movement of electrolyte ions, reorientation of solvent dipoles, adsorption/desorption of ions, etc. In EDLC, only non-faradaic current exists since the electrolytic ions only stay on the surface. In contrast, energy stored in metal oxide (or conducting polymer, which are not discussed in this thesis) is not electrostatic but comes from a faradaic process which takes place within the electrode materials. Non-faradaic current in EDLC is physical in nature while faradaic current in pseudo-capacitance is the result of chemical changes. Other metal oxides such as nickel and manganese oxides/hydroxides [68, 69] have also been used for supercapacitor applications. While these metal oxides are much cheaper than RuO₂, their specific capacitance is lower as a compromise, normally between 20 and 200 F/g.

1.4 CNTs as electrodes for supercapacitors

Although activated carbon and carbon aerogel are the most common electrode materials, CNT is chosen as the electrode materials in this work. The decision is made on the assessment of the two key criteria for supercapacitors: energy density (how long the stored energy can supply) and power density (how fast the energy can be released).

1.4.1 Energy density

The energy of a supercapacitor during a discharge from a voltage of V_0 to zero is equal to:

$$E = \frac{1}{2} CV_0^2 \quad (1-6)$$

E is the total energy output [J], C is the device capacitance [F] and V_0 is the initial voltage [V] that the supercapacitor holds, which is determined by the breakdown voltage of electrolyte, ranging from 1V to 5V (refer to table 1.2). From engineering perspective, V_0 is fixed once the electrolyte material is chosen. The capacitance, C, is decided as:

$$C = \frac{\epsilon_0 \epsilon_r A_s}{d} \quad (1-7)$$

ϵ_0 is the dielectric constant of vacuum [F/m]. ϵ_r is the relative permittivity [no unit] of electrolyte relative to vacuum. d is the physical distance [m] between ions in the electrolyte and the charges (electrons or holes) in the electrode. Both of ϵ_r and d are constant once the electrolyte material is chosen. Therefore, the improvement in capacitance relies on the surface area [m^2], A_s .

Table 1.4. Comparison of activated carbon, carbon aerogels, and carbon nanotube forest [62, 70-74]

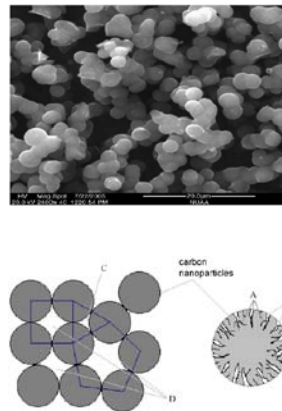


Table 1.4 compares CNT forest (since we use CVD method to grow CNTs, we always obtain CNT forest), activated carbon and carbon aerogel in possible energy storage applications. From the table, it is observed that CNT has the “poorest” nominal surface area as compared with the

activated carbon and carbon aerogel. However, surface area in common carbon materials are dominated by micro pores which are too small for electrolytic ions [59, 60]. As a result, the majority of the nominal surface areas in common carbon materials are not usable in the operation of supercapacitors. In contrast, the spaces between CNTs are usually at a range of 100nm macropores, which can be easily accessible by ions. Therefore, CNT-based supercapacitors show comparable or even better capacitance than common carbon materials in terms of specific capacitance and CNTs could be superior from energy density perspective.

1.4.2 Power density

Two governing equations are considered in calculating power density of a supercapacitor:

(1) The maximum power output P_{\max} [W], is

$$P_{\max} = \frac{V_{\max}^2}{4R_s} \quad (1-8)$$

V_{\max} is the initial voltage of a supercapacitor and it should be no more than the breakdown voltage of the electrolyte. R_s is the equivalent serial resistant (ESR) of a supercapacitor, or say internal resistance. Obviously, R_s should be as small as possible to reduce the energy losses during the operation of supercapacitors.

(2) Time required for a supercapacitor to discharge from initial V_{\max} to a low voltage, say, V' :

$$t(V') = \ln\left(\frac{V_{\max}}{V'}\right) \cdot (R_s + R_L)C \quad (1-9)$$

Here, R_L is the external load resistance. To discharge 98% of the voltage for a supercapacitor the required time is about $4 \cdot (R_s + R_L)C$. It is apparent that R_s should be minimized to reduce the discharge time.

The aforementioned discussions both imply that higher power density is in favor of smaller internal resistance, R_s . Figure 1.15, therefore, decomposes R_s into different root causes:

- Contact resistance of the electrode, R_{Contact} . It includes the internal contact resistance between electrode particles and the contact resistance between electrode material and the current collecting layer (substrate).
- The material resistance of the electrode, $R_{\text{Electrode}}$. It is mostly determined by the conductivity of the electrode material.
- The resistance within the electrolyte, $R_{\text{Electrolyte}}$. It includes the diffusion resistance for the ions to move within pores and the bulky ionic conductivity of the electrolyte.

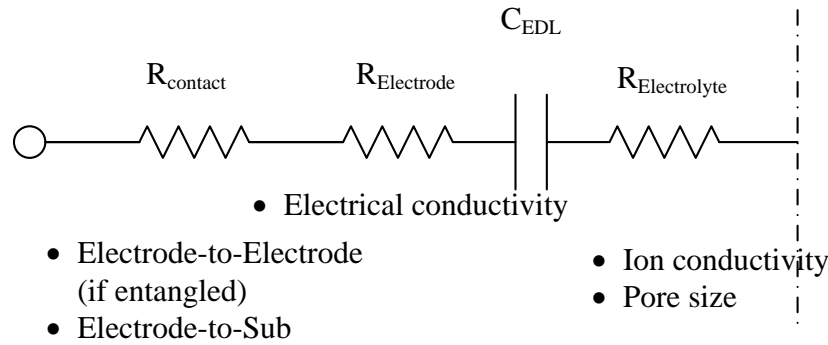


Figure 1.15. The sources of the ESR. The picture is a half-side view. In a supercapacitor, there is a mirror part on the right side of the dash line.

From the table 1.4, it is observed that:

- In term of R_{Contact} , there are numerous contact resistances within the electrode materials and between electrode and substrate for common carbon materials. In contrast, aligned CNT forests are made of long continuous and conductive CNT tube such that current can be delivered within the tube, instead of jumping around from particle to particle. Also, each CNT is in contact with the substrate which minimizes the contact resistance between the electrode and the substrate.
- In term of $R_{\text{Electrode}}$, CNTs have higher conductivity than other carbon forms.
- In term of $R_{\text{Electrolyte}}$, CNT forests have spaces in the macropore range (greater than 50nm) and the aligned structure could favor the transportation of ions. Common carbon materials are full of randomly distributed micropores which could reduce the transport efficiency for ions.

Therefore, CNT forest could provide smaller internal resistance for enhanced power density of supercapacitors.

1.5 Motivations and thesis overview

1.5.1 Motivations

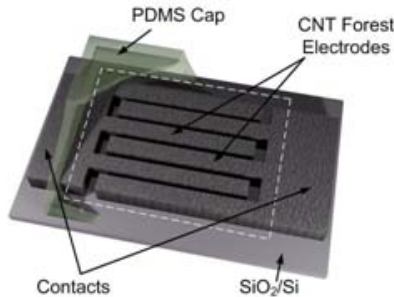
The concept of “MEMS supercapacitor” has been largely overlooked. For example, micro batteries and micro fuel cells have attracted researchers’ attention for years with numerous achievements [75, 76]. On the other hand, while the concept of a supercapacitor itself, proposed in 1957 and marketed in 1978 [77], is nothing new, a miniaturized supercapacitor has not been fully investigated. Only a few groups [78, 79] have worked on “micro supercapacitors” such that there could be tremendous research opportunities to develop miniaturized supercapacitors. Specifically, miniaturized energy storage systems that temporarily store the energy between energy harvesting sources and energy-consuming applicants would provide important breakthroughs. Supercapacitors could fit the role nicely. Also, supercapacitors have high power density such that they could be ideal power sources for pulse-power applications such as hearing

aid (need high current to improve audio quality), RF MEMS (need high current to make wireless signal strong), and optical applications (laser devices need high power to emit light).

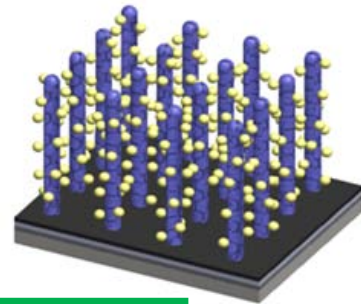
1.5.2 Thesis overview

Figure 1.16 highlights four main development stages in this thesis work and table 1.5 lists electrode materials and achievements in each stage. The common goal in all these stages is to boost the specific capacitance, C_{SP} , and, therefore, energy density of CNT supercapacitors. The key strategies are based on the highlighted area in the equation in figure 1.16: to increase surface area, electrochemical (pseudo) capacitance, and to reduce the volume.

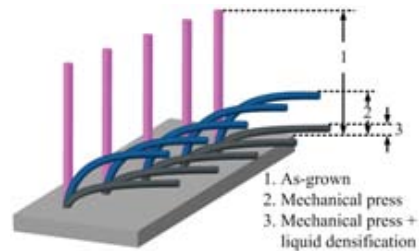
Stage 1: Pristine CNTs ($A \uparrow$)



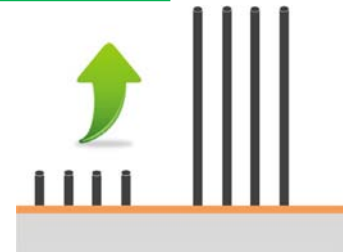
Stage 2: Functionalized CNTs ($C_{Pseudo} \uparrow$)



$$C_{SP} \uparrow = \frac{C_{EDLC} + C_{Pseudo}}{V} = \frac{\frac{\epsilon}{d} A \uparrow + C_{Pseudo} \uparrow}{V \downarrow}$$



Stage 4: Densified CNTs ($V \downarrow$)



Stage 3: Ultra Long CNTs ($A \uparrow$)

Figure 1.16. Four main development stages of CNT supercapacitors in this thesis work to increase the energy density of a supercapacitor, which is calculated based on the equation in the figure, where C_{SP} is the volumetric specific capacitance; C_{EDLC} is the electrochemical double layer capacitance (EDLC); C_{Pseudo} is the pseudo capacitance contributed by additional functionalization material; V is the electrode volume of the capacitor; ϵ is the dielectric constant of the electrolyte; d is the charge distance in the EDLC, and A is the surface area of the porous electrode.

Table 1.5. Overview of the four key development stages of CNT supercapacitors

| Stage | Electrode Material | Features | Improvement factor* | Index |
|-------|--|------------------------------------|-----------------------------|-----------|
| 1 | Pristine/as-grown CNTs | Create porous surface area | 1,000 times than flat metal | Chapter 3 |
| 2 | CNTs Electrodes with embedded nickel nanoparticles | Introduce pseudo capacitance | Up to one order | Chapter 4 |
| 3 | Ultra-long CNTs | Increase capacitance per unit area | 4 times | Chapter 5 |
| 4 | Densified CNTs | Decrease the electrode volume | 16 times | Chapter 5 |

* “Improvement factors” are defined by the capacitance ratio between the supercapacitor using current stage CNT material and those not. All the numbers are based on measured results and could potentially be higher.

As shown in figure 1.16, the dissertation is organized based on these stages for the investigations.

- In this chapter, fundamental theory and necessary knowledge on carbon nanotubes and supercapacitors are introduced.
- In chapter 2, detailed synthesis and optimization processes of CNT forest have been reported. Furthermore, material characterization works are also presented.
- In chapter 3, the first development stage to investigate supercapacitors made of pristine CNT forests is presented. A unique combination of metal stacking layer has been proposed to grow CNT forests on a conductive substrate.
- In chapter 4, CNT pseudocapacitors have been realized by depositing nickel nanoparticles within the CNT forests. A vacuum infiltration process has been used to thoroughly wet the hydrophobic CNT forests. CNT forests electrodes with embedded nickel nanoparticles offer increased energy density by nearly an order than those ones without the nickel nanoparticles in the first stage
- In chapter 5, ultra-long and densified CNTs have been demonstrated, respectively. Both of them realized increases of specific capacitance. The ultra-long CNTs can increase total surface area (stage 3). The densified CNTs forests bring down the electrode volume (stage 4).
- In final chapter 6, a summary of current achievements and possible future works are briefed.
- Some technical details and interesting results are listed in Appendix.

References

- [1] http://en.wikipedia.org/wiki/Carbon_nanotube
- [2] Lecture 8, Carbon Nanotubes: Growth, Assembly, Devices, and Applications, EE235, Spring 2007, UC Berkeley
- [3] http://en.wikipedia.org/wiki/Allotropes_of_carbon
- [4] Raymond M. Reilly, Carbon Nanotubes: Potential Benefits and Risks of Nanotechnology in Nuclear Medicine, *The Journal of Nuclear Medicine*, 2007, 48(7), pp.1039

- [5] Ali Javey, Hyoungsub Kim, Markus Brink, Qian Wang, Ant Ural, Jing Guo, Paul McIntyre, Paul Mceuen, Mark Lundstorm, and Hongjie Dai, High- κ dielectrics for advanced carbonnanotube transistors and logic gates, *Nature Materials*, 2002, 1, pp.241
- [6] Wei Lu and Charles M. Lieber, Nanoelectronics from the bottom up, *Nature Materials*, 2007, 6, pp.841
- [7] http://en.wikipedia.org/wiki/Semiconductor_device_fabrication
- [8] C. L. Kane and E. J. Mele, Size, Shape, and Low Energy Electronic Structure of Carbon Nanotubes, *Physical Review Letters*, 1997, 78(10), pp.1932
- [9] Philip G. Collins, Michael S. Arnold, Phaedon Avouris, Engineering Carbon Nanotubes and Nanotube Circuits Using Electrical Breakdown, *Science*, 2001, 292, pp.706.
- [10] http://nano.mtu.edu/TCVD_CNT_start.html
- [11] A. Gohier, C.P. Ewels, T.M. Minea, M.A. Djouadi, Carbon nanotube growth mechanism switches from tip- to base-growth with decreasing catalyst particle size, *Carbon*, 2008, 46, pp.1331
- [12] Mukul Kumar and Yoshinori Ando, Chemical Vapor Deposition of Carbon Nanotubes: A Review on Growth Mechanism and Mass Production, *Journal of Nanoscience and Nanotechnology*, 2010, 10, pp.3739
- [13] Hongjie Dai, Nanotube Growth and Characterization, *Carbon Nanotubes, Topics Appl. Phys.*, 2001, 80, pp.29, M. S. Dresselhaus, G. Dresselhaus, Ph. Avouris (Eds.), Springer-Verlag Berlin Heidelberg
- [14] Jun Li, Hou Tee Ng, Alan Cassell, Wendy Fan, Hua Chen, Qi Ye, Jessica Koehne, Jie Han, and M. Meyyappan, Carbon Nanotube Nanoelectrode Array for Ultrasensitive DNA Detection, *Nano Letters*, 2003, 3(5), pp.597
- [15] T Gregory Drummond, Michael G Hill, and Jacqueline K Barton, Electrochemical DNA sensors, *Nature Biotechnology*, 2003, 21(10), pp.1192
- [16] J. Justin Gooding, Rahmat Wibowo, Jingquan Liu, Wenrong Yang, Dusan Losic, Shannon Orbons, Freya J. Mearns, Joe G. Shapter, and D. Brynn Hibbert, Protein Electrochemistry Using Aligned Carbon Nanotube Arrays, *J. Am. Chem. Soc.*, 2003, 125, pp.9006
- [17] Joseph Wang, Guodong Liu, and M. Rasul Jan, Ultrasensitive Electrical Biosensing of Proteins and DNA: Carbon-Nanotube Derived Amplification of the Recognition and Transduction Events, *J. AM. CHEM. SOC.*, 2004, 126, pp.3010
- [18] Nadine Wong Shi Kam, Theodore C. Jessop, Paul A. Wender, and Hongjie Dai, Nanotube Molecular Transporters: Internalization of Carbon Nanotube-Protein Conjugates into Mammalian Cells, *J. AM. CHEM. SOC.*, 2004, 126, pp.6850
- [19] Wei Wu, Sebastien Wieckowski, Giorgia Pastorin, Monica Benincasa, Cedric Klumpp, Jean-Paul Briand, Renato Gennaro, Maurizio Prato, and Alberto Bianco, Targeted Delivery of Amphotericin B to Cells by Using Functionalized Carbon Nanotubes, *Angew. Chem. Int. Ed.*, 2005, 44, pp.6358

- [20] Dong Cai, Jennifer M Mataraza, Zheng-Hong Qin, Zhongping Huang, Jianyu Huang, Thomas C Chiles, David Carnahan, Kris Kempa, and Zhifeng Ren, Highly efficient molecular delivery into mammalian cells using carbon nanotube spearing, *Nature Methods*, 2005, 2(6), pp.449
- [21] Liangbing Hu, Mauro Pasta, Fabio La Mantia, LiFeng Cui, Sangmoo Jeong, Heather Dawn Deshazer, Jang Wook Choi, Seung Min Han, and Yi Cui, Stretchable, Porous, and Conductive Energy Textiles, *Nano Lett.*, 2010, 10, pp.708
- [22] Seung Woo Lee¹, Naoaki Yabuuchi, Betar M. Gallant, Shuo Chen, Byeong-Su Kim, Paula T. Hammond and Yang Shao-Horn, High-power lithium batteries from functionalized carbon-nanotube electrodes, *Nature Nanotechnology*, 2010, 5, pp.531
- [23] Cheng Wang, Mahesh Waje, Xin Wang, Jason M. Tang, Robert C. Haddon, and Yushan Yan, Proton Exchange Membrane Fuel Cells with Carbon Nanotube Based Electrodes, *Nano Letters*, 2004, 4(2), pp.345
- [24] Adrian Bachtold, Peter Hadley, Takeshi Nakanishi, Cees Dekker, Logic Circuits with Carbon Nanotube Transistors, *Science*, 2001, 294, pp.1317
- [25] Z. Chen, J. Appenzeller, Y. Lin, J. Sippel-Oakley, A. G. Rinzler, J. Tang, S. J. Wind, P. M. Solomon, and P. Avouris, An Integrated Logic Circuit Assembled on a Single Carbon Nanotube, *Science*, 2006, 311, pp.1735
- [26] Qing Cao, Seung-Hyun Hur, Zheng-Tao Zhu, Yugang Sun, Congjun Wang, Matthew A. Meitl, Moonsub Shim, and John A. Rogers, Highly Bendable, Transparent Thin-Film Transistors That Use Carbon-Nanotube-Based Conductors and Semiconductors with Elastomeric Dielectrics, *Adv. Mater.*, 2006, 18, pp.304
- [27] Sunkook Kim, Sanghyun Ju, Ju Hee Back, Yi Xuan, Peide D. Ye, Moonsub Shim, David B. Janes, and Saeed Mohammadi, Fully Transparent Thin-Film Transistors Based on Aligned Carbon Nanotube Arrays and Indium Tin Oxide Electrodes, *Adv. Mater.*, 2009, 21, pp.564
- [28] Masahiro HORIBE, Mizuhisa NIHEI, Daiyu KONDO, Akio KAWABATA, and Yuji AWANO, Carbon Nanotube Growth Technologies Using Tantalum Barrier Layer for Future ULSIs with Cu/Low-k Interconnect Processes, *Japanese Journal of Applied Physics*, 2005, 44(7A), pp.5309
- [29] Azad Naeemi and James D. Meindl, Carbon Nanotube Interconnects, *Annu. Rev. Mater. Res.*, 2009, 39, pp.255
- [30] J. Kong, N. R. Franklin, C. Zhou, M. G. Chapline, S. Peng, K. Cho, H. Dai, Nanotube Molecular Wires as Chemical Sensors, *Science*, 2000, 287, pp.682
- [31] Chen Wei, Liming Dai, Ajit Roy, and Tia Benson Tolle, Multifunctional Chemical Vapor Sensors of Aligned Carbon Nanotube and Polymer Composites, *J. AM. CHEM. SOC.*, 2006, 128, pp.1412
- [32] E. S. Snow, F. K. Perkins, E. J. Houser, S. C. Badescu, T. L. Reinecke, Chemical Detection with a Single-Walled Carbon Nanotube Capacitor, *Science*, 2005, 307, pp.1942
- [33] Ashish Modi, Nikhil Koratkar, Eric Lass, Bingqing Wei and Pulickel M. Ajayan, Miniaturized gas ionization sensors using carbon nanotubes, *Nature*, 2003, 424, pp.171

- [34] J T WYeow and J P M She, Carbon nanotube-enhanced capillary condensation for a capacitive humidity sensor, *Nanotechnology*, 2006, 17, pp.5441
- [35] Paul W. Barone, Seunghyun Baik, Daniel A. Heller, and Michael S. Strano, Near-infrared optical sensors based on single-walled carbon nanotubes, *Nature Materials*, 2005, 4, pp.86
- [36] Esther S. Jeng, Anthonie E. Moll, Amanda C. Roy, Joseph B. Gastala, and Michael S. Strano, Detection of DNA Hybridization Using the Near-Infrared Band-Gap Fluorescence of Single-Walled Carbon Nanotubes, *Nano Letters*, 2006, 6(3), pp.371
- [37] Shoushan Fan, Michael G. Chapline, Nathan R. Franklin, Thomas W. Tomblor, Alan M. Cassell, Hongjie Dai, Self-Oriented Regular Arrays of Carbon Nanotubes and Their Field Emission Properties, *Science*, 1999, 283, pp.512
- [38] W. B. Choi, D. S. Chung, J. H. Kang, H. Y. Kim, Y. W. Jin, I. T. Han, Y. H. Lee, J. E. Jung, N. S. Lee, G. S. Park, and J. M. Kim, Fully sealed, high-brightness carbon-nanotube field-emission display, *Applied Physics Letters*, 1999, 75(20), pp.3129
- [39] S. Nagasawa, H. Arai, R. Kanzaki and I. Shimoyama, Integrated Multi-fucntional Probe for Active Measurements in a Single Neural Cell, The 13th International Conference on Solid-State Sensors, Actuators and Microsystems, Seoul, Korea, June 5-9, 2005
- [40] Ke Wang, Harvey A. Fishman, Hongjie Dai, and James S. Harris, Neural Stimulation with a Carbon Nanotube Microelectrode Array, *Nano Letters*, 2006, 6(9), pp.2043
- [41] Yiming Yan, Wei Zheng, Lei Su, and Lanqun Mao, Carbon-Nanotube-Based Glucose/O₂ Biofuel Cells, *Adv. Mater.*, 2006, 18, pp.2639
- [42] Ioana Dumitrescu, Jonathan P. Edgeworth, Patrick R. Unwin, and Julie V. Macpherson, Ultrathin Carbon Nanotube Mat Electrodes for Enhanced Amperometric Detection, *Adv. Mater.*, 2009, 21, pp.1
- [43] Morinobu Endo, Shozo Koyama, Yoshikazu Matsuda, Takuya Hayashi, and Yoong-Ahm Kim, Thrombogenicity and Blood Coagulation of a Microcatheter Prepared from Carbon Nanotube-Nylon-Based Composite, *Nano Letters*, 2005, 5(1), pp.101
- [44] Vinod P. Veedu, Anyuan Cao, Xuesong Li, Kougen Ma, Caterina Soldano, Swastik Kar, Pulickel M. Ajayan, and Mehrdad N. Ghasemi-Nejhad, Multifunctional composites using reinforced laminae with carbon-nanotube forests, *Nature Materials*, 2006, 5, pp.457
- [45] Ray H. Baughman, Changxing Cui, Anvar A. Zakhidov, Zafar Iqbal, Joseph N. Barisci, Geoff M. Spinks, Gordon G. Wallace, Alberto Mazzoldi, Danilo De Rossi, Andrew G. Rinzler, Oliver Jaschinski, Siegmur Roth, Miklos Kertesz, Carbon Nanotube Actuators, *Science*, 1999, 284, pp.1340
- [46] Von Howard Ebron, Zhiwei Yang, Daniel J. Seyer, Mikhail E. Kozlov, Jiyoung Oh, Hui Xie, Joselito Razal, Lee J. Hall, John P. Ferraris, Alan G. MacDiarmid, Ray H. Baughman, Fuel-Powered Artificial Muscles, *Science*, 2006, 311, pp.1580
- [47] K. Kordás, G. Tóth, P. Moilanen, M. Kumpumäki, J. Vähäkangas, and A. Uusimäki, Chip cooling with integrated carbon nanotube microfin architectures, *Applied Physics Letters*, 2007, 90, pp.123105

- [48] Yuhei Hayamizu, Takeo Yamada, Kohei Mizuno, Robert, C. Davis, Don N. Futaba, Motoo Yumura, and Kenji Hata, Integrated three-dimensional microelectromechanical devices from processable carbon nanotube wafers, *Nature Nanotechnology*, 2008, 3, pp.289
- [49] David N. Hutchison, Nicholas B. Morrill, Quentin Aten, Brendan W. Turner, Brian D. Jensen, Larry L. Howell, Fellow, ASME, Richard R. Vanfleet, and Robert C. Davis, Carbon Nanotubes as a Framework for High-Aspect-Ratio MEMS Fabrication, *Journal of Microelectromechanical Systems*, 2010, 19(1), pp.75
- [50] Wei-Chang Li, Yingqi Jiang, Robert A. Schneider, Henry G. Barrow, Liwei Lin and Clark T.-C. Nguyen, Polysilicon-filled Carbon Nanotube Grass Structural Material for Micromechanical Resonators, IEEE MEMS 2011, Cancun, MEXICO, January 23-27, 2011
- [51] B. E. Conway, *Electrochemical Supercapacitors: Scientific Fundamentals and Technological Applications*, Kluwer Academic/Plenum Publishers, New York, 1999.
- [52] A. J. Bard, and L. R. Faulkner. *Electrochemical Methods, Fundamentals and Applications* (2nd), John Wiley & Sons, Inc, 2001
- [53] R. L. Spyker, and R. M. Nelms, Classical Equivalent Circuit Parameters for a Double-Layer Capacitor, *IEEE Transactions on Aerospace and Electronic Systems*, 2000, 36(3), pp.829
- [54] Lisheng Shi, and M. L. Crow, Comparison of Ultracapacitor Electric Circuit Models, IEEE Power and Energy Society General Meeting - Conversion and Delivery of Electrical Energy in the 21st Century, Pittsburgh, PA, USA, 20-24 July 2008
- [55] S. Arepalli, H. Fireman, C. Huffman, P. Moloney, P. Nikolaev, L. Yowell, C.D. Higgins, K. Kim, P.A. Kohl, S.P. Turano, and W.J. Ready, Carbon-Nanotube-Based Electrochemical Double-Layer Capacitor Technologies for Spaceflight Applications, *J of Mat.*, 2005, 57(12), pp.26
- [56] Adrian Schneuwly, Roland Gallay, Properties and applications of supercapacitors From the state-of-the-art to future trends, Proceeding PCIM'2000. Nürnberg, Germany, 2000
- [57] Benjamin R. Mattes, Santa Fe Science and Technology, Conducting Polymer Films and Fibers for Energy Storage and Optical Switching, Workshop Presentation to Energy and Materials: Critical Issues for Wireless Sensor Networks, Dublin City University, 30th June, 2006
- [58] Chuang Peng, Shengwen Zhang, Daniel Jewell, George Z. Chen, Carbon nanotube and conducting polymer composites for supercapacitors, *Progress in Natural Science*, 2008, 18, pp.777
- [59] A.G. Pandolfo and A.F. Hollenkamp, Carbon properties and their role in supercapacitors, *Journal of Power Sources*, 2006, 157, pp.11
- [60] Elzbieta Frackowiak, Francois Beguin, Carbon materials for the electrochemical storage of energy in capacitors, *Carbon*, 2001, 39, pp.937
- [61] <http://joejaworski.wordpress.com/2008/05/09/does-a-reef-tank-need-carbon/>
- [62] Junbing Wang, Xiaoqing Yang, Dingcai Wu, Ruowen Fu, Mildred S. Dresselhaus, Gene Dresselhaus, The porous structures of activated carbon aerogels and their effects on electrochemical performance, *Journal of Power Sources*, 2008, 185, pp.589

- [63] Patrice Simon and Yury Gogotsi, Materials for electrochemical capacitors, *Nature Materials*, 2008, 7, pp.845
- [64] <http://electrochem.cwru.edu/encycl/art-c03-elchem-cap.htm>
- [65] P. Kurzweil, Precious metal oxides for electrochemical energy converters: Pseudocapacitance and pH dependence of redox processes, *Journal of Power Sources*, 2009, 187, pp.284
- [66] K. Kuratani, T. Kiyobayashi, N. Kuriyama, Influence of the mesoporous structure on capacitance of the RuO₂ electrode, *Journal of Power Sources*, 2009, 189, pp.1284
- [67] http://www2.chemistry.msu.edu/courses/cem837/Chapter%201_notes.pdf
- [68] U.M. Patil, K.V. Gurav, V.J. Fulari, C.D. Lokhande, Oh Shim Joo, Characterization of honeycomb-like “ β -Ni(OH)₂” thin films synthesized by chemical bath deposition method and their supercapacitor application, *Journal of Power Sources*, 2009, 188, pp.338
- [69] P. Staiti, F. Lufrano, Study and optimisation of manganese oxide-based electrodes for electrochemical supercapacitors, *Journal of Power Sources*, 2009, 187, pp.284
- [70] Hao Zhang, Gaoping Cao, Yusheng Yang, Electrochemical properties of ultra-long, aligned, carbon nanotube array electrode in organic electrolyte, *Journal of Power Sources*, 2007, 172, pp.476
- [71] Deyang Qu, Hang Shi, Studies of activated carbons used in double-layer capacitors, *Journal of Power Sources*, 1998, 74, pp.99
- [72] M. Selvakumar, D. Krishna Bhat, Activated Carbon-Polyethylenedioxythiophene Composite Electrodes for Symmetrical Supercapacitors, *Journal of Applied Polymer Science*, 2008, 107, pp.2165
- [73] Jun Li, Xianyou Wang, Qinghua Huang, Sergio Gamboa, P.J. Sebastian, Studies on preparation and performances of carbon aerogel electrodes for the application of supercapacitor, *Journal of Power Sources*, 2006, 158, pp.784
- [74] S. J. KIM, S. W. HWANG, S. H. HYUN, Preparation of carbon aerogel electrodes for supercapacitor and their electrochemical characteristics, *Journal of Materials Science*, 2005, 40, pp.725
- [75] G. Pistoia, *Batteries For Portable Devices*, Elsevier, Amsterdam
- [76] Y. Jiang, X.Wang, L. Zhong, and L. Liu, Design, fabrication and testing of a silicon-based air-breathing micro direct methanol fuel cell, *J. Micromech. Microeng.*, 2006, 16, pp.s233
- [77] http://en.wikipedia.org/wiki/Electric_double-layer_capacitor
- [78] Joo-Hwan Sunga, Se-Joon Kima, Soo-Hwan Jeong, Eun-Ha Kim, Kun-Hong Lee, Flexible micro-supercapacitors, *Journal of Power Sources*, 2006, 162, pp.1467
- [79] Wei Suna, Xuyuan Chen, Preparation and characterization of polypyrrole films for three-dimensional micro supercapacitor, *Journal of Power Sources*, 2009, 193, pp.924–929

Chapter 2 Synthesis and characterization of CNT forests

In this chapter, experimental setup and processing optimization of the synthesis of CNT forests are discussed, including using masks to define the geometry of the CNT forests and the characterization of their contact and sheet resistances. Specifically, comprehensive studies on the sheet and contact resistances of vertically aligned carbon nanotube (CNT) forests with as-grown bottom contacts to the metal layer have been conducted. Using microfabrication and four distinct methods: (1) transfer length method (TLM), (2) contact chain method, (3) Kelvin method, and (4) four-point probe method, multiple testing devices have been designed to characterize the resistances of CNT forest-based devices. Experimental results show that devices based on stripe-shaped CNT forest with 100 μm in height and 100 μm in width have a sheet resistance of approximately 100 Ω/\square . The corresponding contact resistance to the molybdenum layer is roughly 50 Ω for a contact area of 1000 μm^2 . Consistency of the results from the four different methods validates the approaches. After two-month storage of CNT forest samples in open air, less than 0.9% deviations on the resistance values are observed. We further demonstrated one application of CNT forests as a NH_3 gas sensor and measured 0.5ppm of sensing resolution with a detection response time of 1 minute.

2.1 CNT synthesis

2.1.1 Experimental setup

The experimental setup of the CVD synthesis process for CNT forests is shown in figure 2.1. In the prototype experimental setup, a substrate deposited with both Al and Fe thin layers is placed in a furnace. The furnace is heated up to a desirable temperature such as, 720 $^\circ\text{C}$, and carbon precursor gases (such as ethylene, C_2H_4) and hydrogen mixture are flowed into the furnace. CNTs are synthesized with the assistance of catalysts following the reaction:



The basic VLS synthesis procedure for the CVD process has been described in chapter 1 and Appendix A details the experimental equipments.

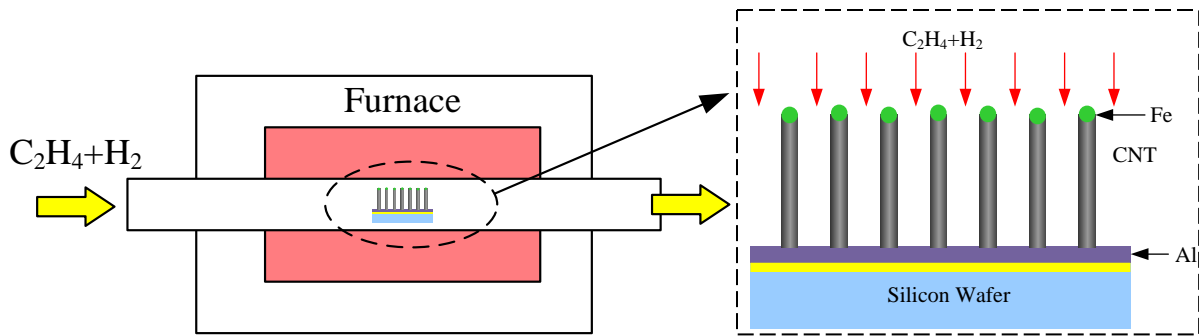


Figure 2.1. Experimental setup for the synthesis of CNT forests.

2.1.2 Process optimization

The growth of CNT forests are influenced by many factors such as the growth substrate, temperature, carbon precursor gases, pressure, and gas flow rates. The general synthesis procedure used in this work is listed in table 2.1. Key process parameters are discussed below.

Table 2.1. General protocol for the synthesis of CNT forests

| |
|---|
| 1. Thermal oxidization of silicon wafer with 1000-2000Å oxide. |
| 2. Deposition of aluminum and iron in sequence with a thickness of 10nm and 5nm, respectively using e-beam evaporation. |
| 3. Place the diced samples into a 2-inch quartz tube, pump down the tube, and then fill it with pure hydrogen. Keep hydrogen flowing at a low velocity of 50sccm and heat up furnace to 720°C. |
| 4. Once the temperature is stabilized, carbon precursor gases of C_2H_4 and H_2 are flowed into the tube with velocities of 90sccm and 611sccm, respectively. A standard growth time is 10mins. |
| 5. Pull out the tube from the furnace and cool down it with a fan until below 200°C |
| 6. Purge the system with Ar, open the tube, and unload the samples |

(1) Catalyst thickness

The CVD process is based on catalysts, and therefore, the catalyst is the most sensitive parameter to the CVD results. Under the synthesis conditions used in table 2.1, CNT forests grow densely if around 5nm in thickness of iron is deposited as the catalyst. In contrast, 1nm-thick iron layer fails to grow any CNTs and 10nm-thick iron layer generates carbon nanofibers (CNFs). Figure 2.2 are growth results of CNT samples with different iron thickness. Figures 2.2(a), (b), (c) are top views of CNT samples with 1, 5 and 10nm-thick iron as the catalyst with results of no CNTs, dense CNTs and CNFs, respectively. The close view SEM photos of Figures 2.2 (b) and (c) are shown in (d) and (e) with different morphological between CNTs and CNFs, respectively. It is observed that CNTs have relatively small diameters of about 20nm with smooth sidewalls, while CNFs have diameters of over 100nm with rough sidewalls and possible solid cores inside.

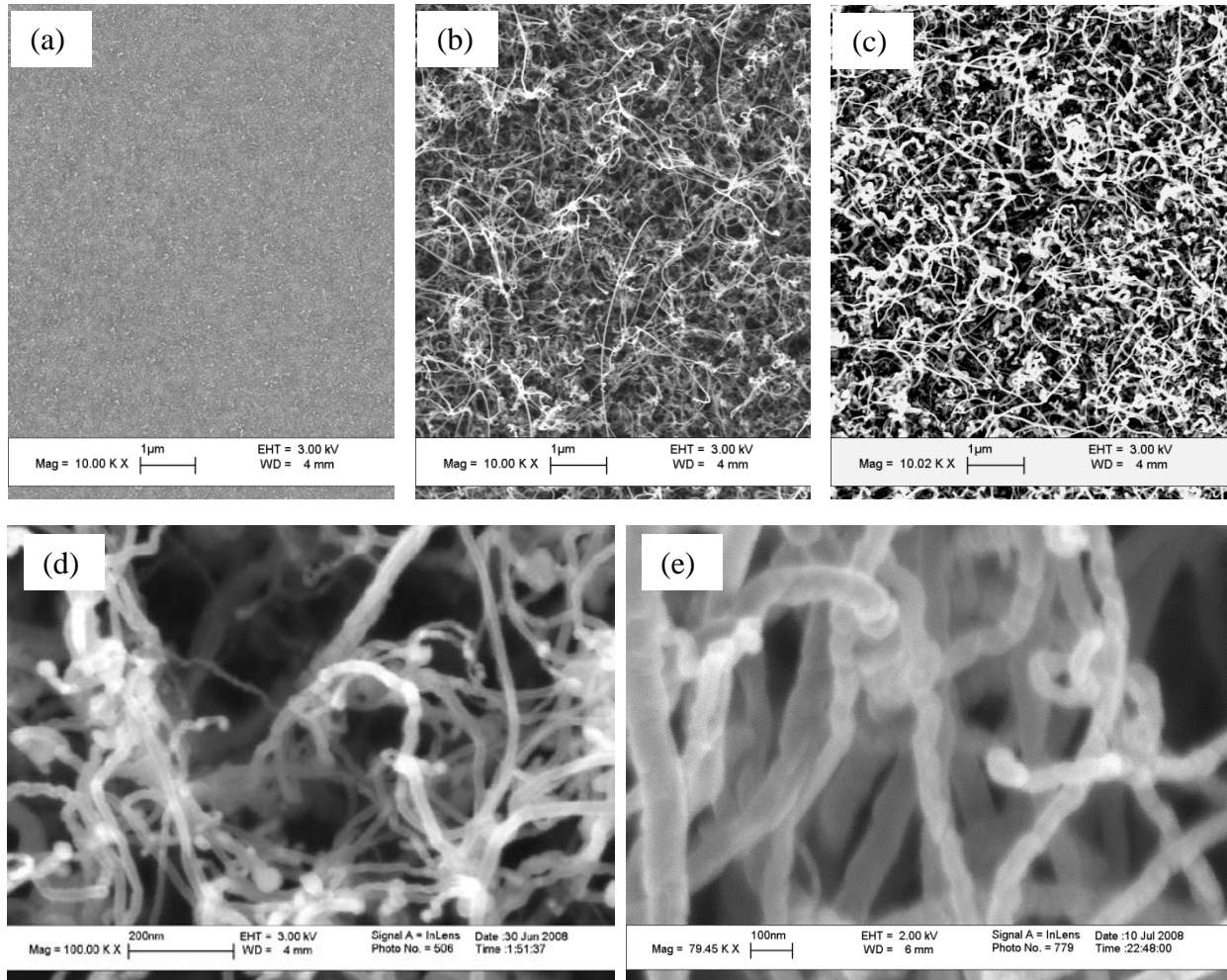


Figure 2.2. (a), (b) and (c): top view SEMs of CNT growth samples using 1, 5, and 10nm-thick iron layers as the catalyst, respectively. (d) and (e): close view SEMs of (b) and (c) showing CNTs and CNFs, respectively.

The thickness of the iron catalyst layer determines the formation of CNT or CNFs as nucleation of catalyst particles depends on the finite mobility and diffusion of metal atoms on SiO_2 at high temperatures [1]. During the heating process, deposited (originally dispersed) atoms irreversibly “hit and stick” to each other via metal-metal interactions and eventually form stationary catalyst particles. The mean diffusion distance, l_{diff} , can be approximated by the Einstein relation:

$$l_{\text{diff}} \propto D \propto \exp\left(\frac{-E_{\text{diff}}}{kT}\right) \quad (2-2)$$

where D is the diffusion coefficient and E_{diff} is the diffusion activation energy. For any given metal, clustering of atoms takes place within a radius of $r \sim l_{\text{diff}}$. Under the same conditions, the radius r is almost the same and, therefore, thicker catalyst layer means larger diameter of nucleated particles. Since CNTs with 100nm in diameter are not mechanically stable, CNFs are formed.

(2) Supporting layer (Al) thickness

In this study, aluminum (Al) is the supporting layer. Its role is to support the proper nucleation of the iron layer by affecting the E_{diff} in equation (2-2), and to prevent the interaction of the iron catalyst layer with the substrate. Generally speaking, the process is not sensitive to the thickness of Al. If Al is thicker than 5nm, there is no noticeably impact on the quality of the CNT forests. However, if Al is thicker than 100nm, problems can occur. Figure 2.3 shows the synthesis results by using 100nm-thick Al. In figure 2.3(a), the metal layer was peeled off from the substrate possibly due to the mismatch of CTEs (coefficient of thermal expansion). In figure 2.3(b), the defined aluminum features melted and spread around. It was because aluminum has a low melting temperature of 660°C and the synthesis temperature at 720°C would cause the melting and flowing of aluminum. On the other hand, thin-layer of aluminum could have been fully or partially oxidized into Al_2O_3 (though H_2 and C_2H_4 are overall reductive, there are always limited amount of oxygen in the gases [2]), which has a much higher melting temperature of 2072°C. It is also noted that thicker aluminum results in thin and non-uniform growth of CNT forests. One possible reason is that flowing aluminum may have broken the continuous Al_2O_3 layer and negatively affect the nucleation of the iron catalysts as a result.

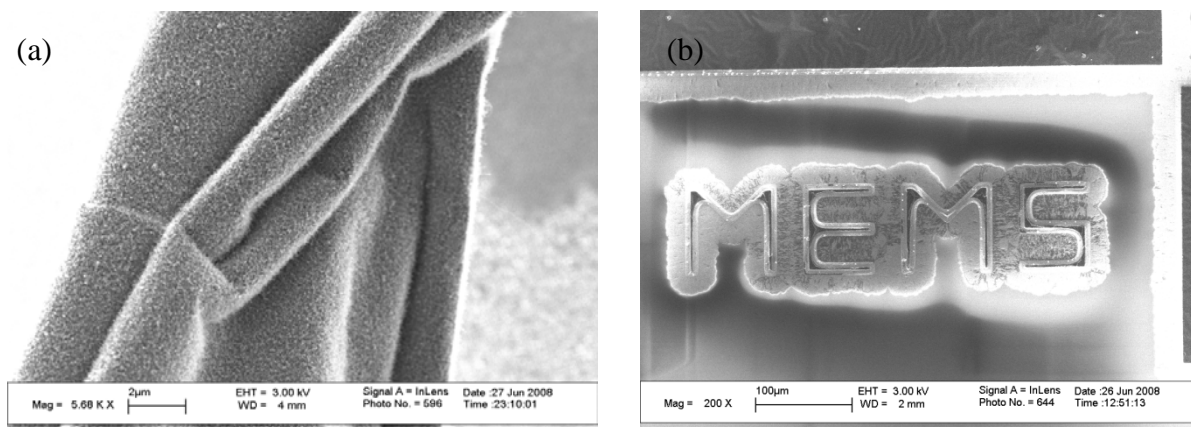


Figure 2.3. SEM photos showing the synthesis results of CNT forests by using a 100nm-thick aluminum layer. It is observed that the layer could be peeled off as shown in (a) or melt and spread as shown in (b).

(3) Synthesis temperature

The optimum synthesis temperature depends strongly on the type of carbon precursor. Three commonly-used carbon precursors are C_2H_2 , C_2H_4 , and CH_4 . CNTs can be synthesized with C_2H_2 at a temperature as low as 540°C [3]. If C_2H_2 is heated up to a high temperature, the precursor gas would decompose so quickly such that amorphous carbon could wholly cover the catalyst particles and prevent new carbon generations. In contrast, it requires a high synthesis temperature of 900°C if CH_4 is used as the reaction gas [4] as carbon precursors won't decompose at a low temperature (experimentally verified). In this study, C_2H_4 is chosen as the reaction gas because it can grow good quality CNTs (compared to C_2H_2) and has a good range of synthesis temperature (compared to CH_4). After conducting several trial experiments, it is found that synthesis temperature around 720°C produces best CNT growth results. Figures 2.4 show 10-mins growth results of CNT forests at 650°C and 720°C at atmospheric pressure with C_2H_4 and H_2 flow rate of 90sccm and 611sccm, respectively. It is observed that shorter (~10 μm) CNTs are synthesized at 650°C and longer (~60 μm) CNTs are synthesized at 720°C.

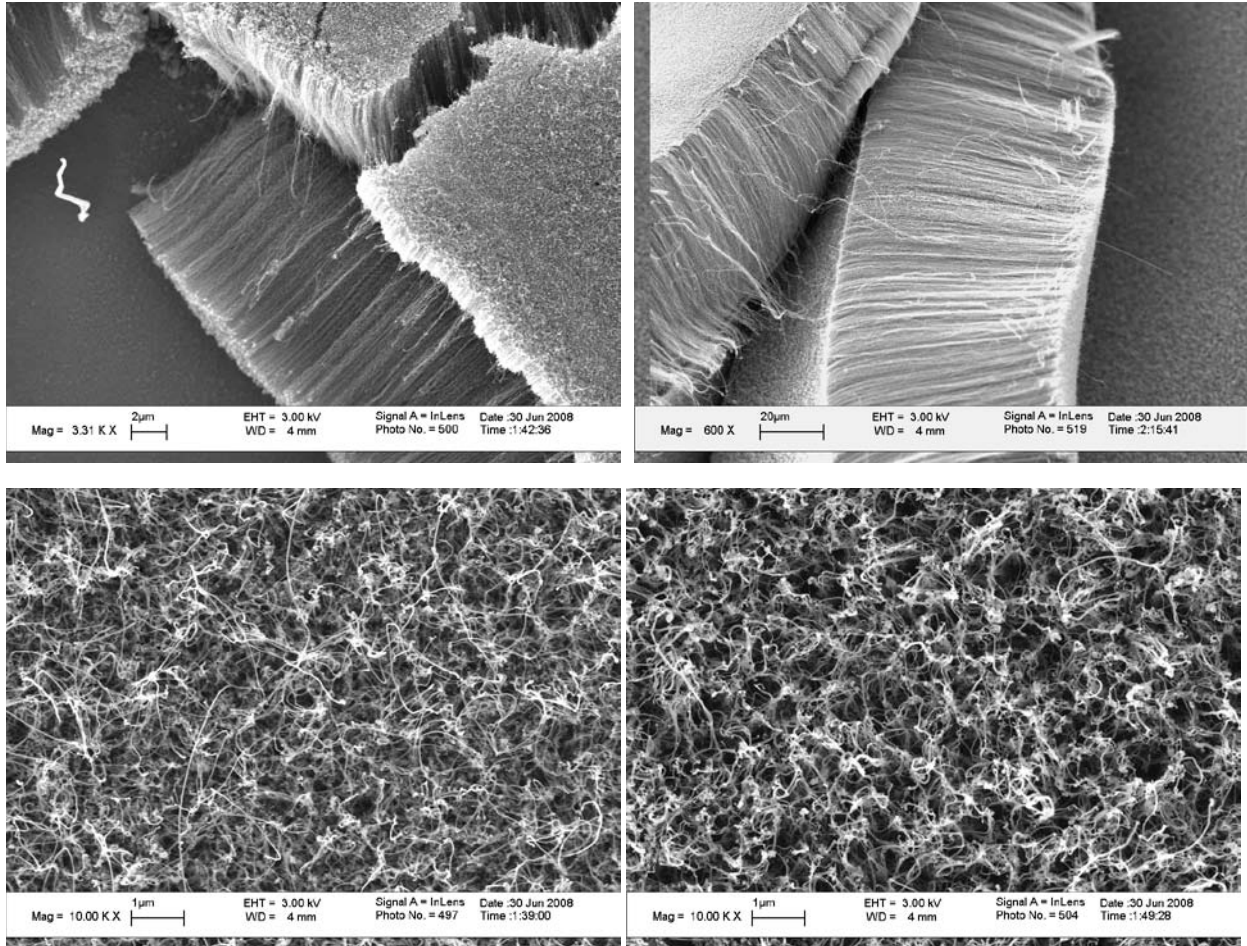


Figure 2.4. (a) and (c) are side and top views of CNTs synthesized at 650°C for 10mins. (b) and (d) are side and top views of CNTs synthesized at 720°C for 10mins. Temperature is the only difference between the two experiments and it is found that high temperature generates longer CNT (60µm vs. 10µm).

(4) Synthesis time

Figure 2.5 shows the experimental results of height of synthesized CNT forest versus growth time. A linear relationship is obtained within 10min growth and the average growth rate is about 1µm/min. Knowing this, we can synthesize precisely 2µm-thick CNT forests as shown in figure 2.6 as the building material for RF resonators [5]. However, CNTs can't grow indefinitely as numerous groups have discovered. Instead, CNTs stop their growth at certain points [6]. One popular explanation is the “catalyst-poisoning” effect that amorphous carbon is gradually cover the catalyst particle and blocks the access of additional carbon precursor gas to the catalyst particles. Actually based on this assumption, people proposed the idea of water-assisted CVD growth [7] where water is used as weak oxidant to remove amorphous carbon. In that case, CNT can grow as long as millimeter level. Chapter 5 will detail that process.

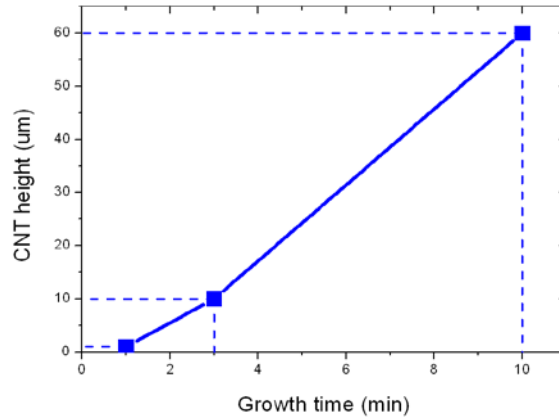


Figure 2.5. Relationship between the heights of the CNT forest versus growth time. A linear relationship is obtained within the process parameters based on the experimental results.

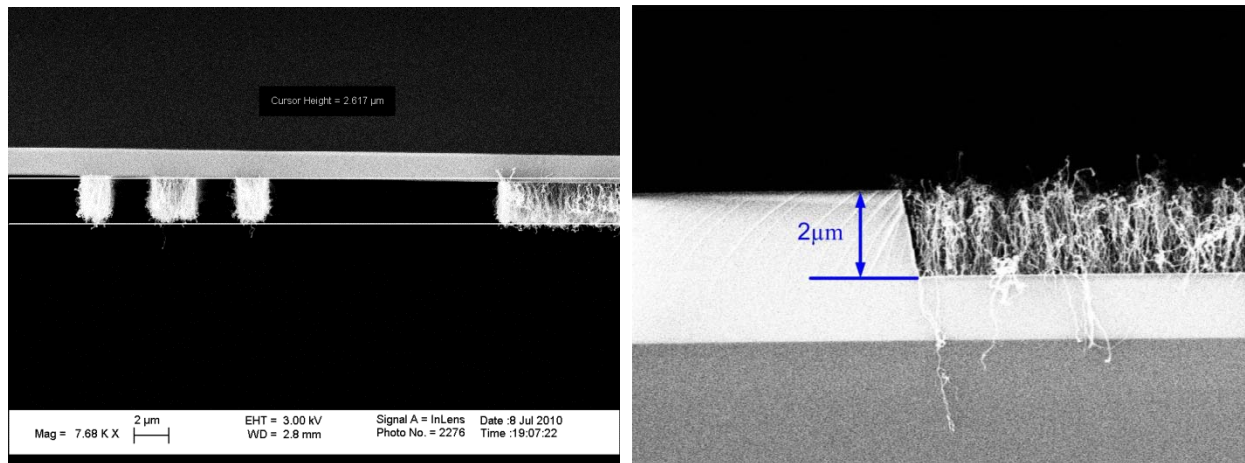


Figure 2.6. 2µm-thick CNT forest. Height control is realized by growth time.

(5) Role of hydrogen

Hydrogen is used as the gas carrier for C_2H_4 . It is noted that during the temperature ramp-up process, the Mo/Al/Fe layer (a conductive substrate used to grow CNT on) won't function as the catalyst layer if only inert gas such as argon is used in the tube and hydrogen is the necessary ingredient to activate the catalyst. However, once the growth temperature is reached, the reaction gases, including carbon precursor and hydrogen should be flowed into the reaction tube as soon as possible. Numerous trials confirm that a 4-min delay would result in no CNT growth. One possible explanation is that hydrogen is needed to form hydride with Mo as Mo alone deters the growth of CNT. However, extra hydride or strong interaction of hydrogen with Al and Fe could also degrade the synthesis of CNTs. Other groups have also reported the controversial role of hydrogen in the CVD CNT synthesis processes. One group [8] claimed that hydrogen reduces the rate of carbon production by dehydrogenation so that the more ordered and thermodynamically stable MWCNTs can be produced rather than less ordered and thermodynamically stable soot and carbon fibers. Another group [2] claimed that reactive hydrogen species could, however, damage the formation of SWNTs.

2.2 Material Characterization using tape masks

2.2.1 Background

CNTs have been widely studied for various applications due to their unique characteristics including small diameters, high electrical conductivity, high surface area to volume ratio, and outstanding mechanical and thermal properties [9, 10]. Vertically aligned CNT forests used in this study are favored over individual CNTs in terms of reliability, manufacturability, and structural architecture, which are all important practical issues for commercialization. For reliability considerations, bulk CNT forests can tolerate defects and failures of small numbers of CNTs within the matrix while such issues would result in system failure for devices based on individual CNTs. In terms of manufacturability, CNT forests can be easily produced in large quantities by methods such as chemical vapor deposition (CVD) at low cost [11]. In terms of structural architecture, aligned CNT forests could be ideal materials for applications including electrodes for energy storage systems (e.g. supercapacitors [12] and batteries [13]), sensing elements for sensors [14], and interconnects in microelectronics [15] due to their intrinsic merits in orderly arrangement, natural contacts to the growth substrate, and high surface area to volume ratio.

Prior electrical characterizations of CNTs have focused on individual CNTs [16-19]. For example, S. Frank *et al.* discovered that 4 μ m-long multiwalled carbon nanotubes (MWNTs) could tolerate high electrical current densities of larger than 10⁷A/cm² [16] and B.Q. Wei *et al.* reported an even higher current carrying capacity ($J > 10^9$ A/cm²) without detectable resistance changes [17]. A. Javey *et al.* found that contacts made of palladium (Pd) with semiconducting single-walled nanotubes (SWNTs) greatly reduced the Schottky barriers, making the ‘ON’ states similar to ballistic metallic tubes [18]. Recently, characterization studies have also been based on large number of CNT networks. For example, L. Hu *et al.* made a transparent SWNT networks by vacuum filtration and reported a sheet resistance of 1000 Ω/\square and light transmittance of 70% under visible wavelength [20]. Several research groups have also examined the properties of aligned CNT forests. D.J. Yang *et al.* studied the electrical properties of CNT forests using a simple, two-terminal I-V method with gold foil in contact with the top of the CNT forests and found the effective electrical conductance of CNT forests in the vertical and lateral directions were in the range of 10⁴ S/m and 10² S/m, respectively [21]. C. Lin *et al.* used a four-point-probe method by depositing titanium contact pads on the top of the CNT forest to measure their vertical and lateral electrical conductance [22]. Recently N. Chiodarelli *et al.* used vertically aligned CNT pillars as CMOS vias and formed the contacts by evaporating Ti/Au as top electrodes and using TiN substrate as the bottom electrode [23]. These studies provide important information on the electrical characteristics of CNT forests; however, the contacts in these studies were primarily formed by depositing or establishing contacts on the top surface of CNT forests. At present, the intrinsic contact resistance between CNT forests and the bottom substrate has not been investigated.

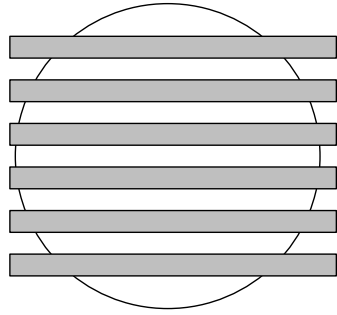
CNT forest-based devices (e.g. supercapacitor in this study or CNT gas sensor) operate quite differently from devices consisting individual CNTs and disoriented CNT networks. First, electrical current in the CNT forests flows in the horizontal direction which is perpendicular to the longitudinal direction of individual CNTs that most other studies have reported [16-20]. As a

result, the total resistance of CNT forests is strongly affected by structure properties, such as side-contacts between inter-tangled CNTs. Second, the contact between CNT forests and the external world can influence the overall electrical properties. In the case of individual CNTs and disoriented CNT networks, the electrical contacts are primarily deposited after the CNT growth to form good ohmic contacts. Electrical contacts were made similarly in previous studies for CNT forests [21-23] by adding extra metal foils or metal depositions. These top contacts are not ideal for CNT forests, because they increase the process complexity and potentially degrade the contact integrity due to mechanical fragility of the porous matrix. Furthermore, these top contacts can block external species from accessing the internal parts of CNT forest, thereby decreasing their transport efficiency. In the majority of prior studies, CNTs have been grown predominantly on non-conducting substrates [24] such that formation of the top contacts is necessary for electrical characterizations. In this and next sections, we used a unique combination of Mo/Al/Fe deposited on a silicon wafer to enable direct growth of CNT forests with the bottom molybdenum as the conductive layer [25] (the reasoning and fabrication process of using the Mo/Al/Fe layer will be described in details in chapter 3).

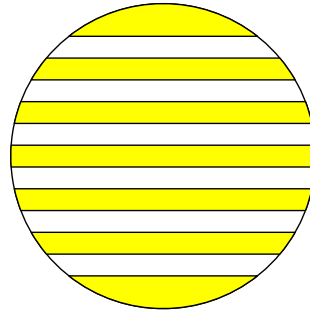
2.2.2 Fabrication

We proposed “Tape mask” method as a very convenient way to quickly evaluate the material property of CNTs. The basic principle is similar to the shadow mask and the fabrication process is shown in figure 2.7 with the following key steps: (a) to stick tapes on a silicon wafer to define the contact area; (b) to deposit 50nm Mo using e-beam evaporation and to peel off the tapes afterwards; (c) to stick tapes on the silicon wafer for a second time to define the CNT growth area; (d) to deposit 10nm Al and 5nm Fe by using e-beam evaporation and to remove the tapes thereafter; (e) to dice the wafer; (f) to grow CNTs using the CVD recipe listed in table 2.1; and (g) to carry out the experimental measurements.

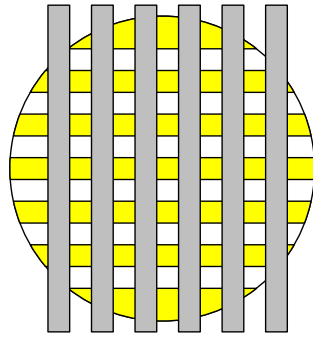
The alignments of tapes in step (a) & (c) are achieved by fixing the wafer on a larger paper that is pre-printed with design grids. By aligning the tapes with the grids on the paper, we indirectly achieve the alignment of them on the wafer. The fabricated CNT samples are shown in figure 2.8 with two types of CNT forest resistors with widths of 2mm and 5mm, respectively. The length of each segment between two Mo pads is 14.7mm (for 2mm-wide resistors) and 17.7mm (for 5mm-wide resistors), respectively.



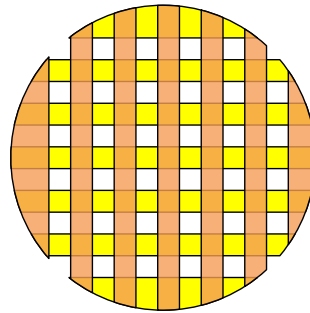
(a) Tape sticking I



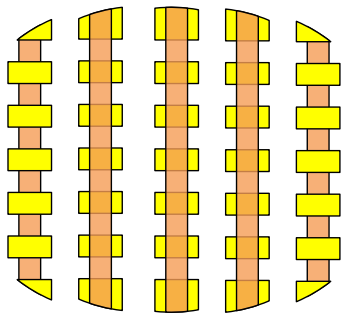
(b) Bottom electrode (Mo) deposition



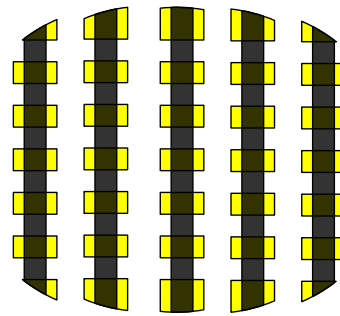
(c) Tape sticking II



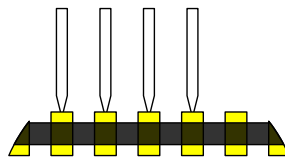
(d) Catalyst (Al/Fe) deposition



(e) Dicing



(f) furnace growth



(g) 4-probe measurement

Figure 2.7. Fabrication of CNT devices using “tape-mask” method. Yellow color represents 50nm Mo layer, orange color is the Al/Fe bi-layer, and grey color is the tape.

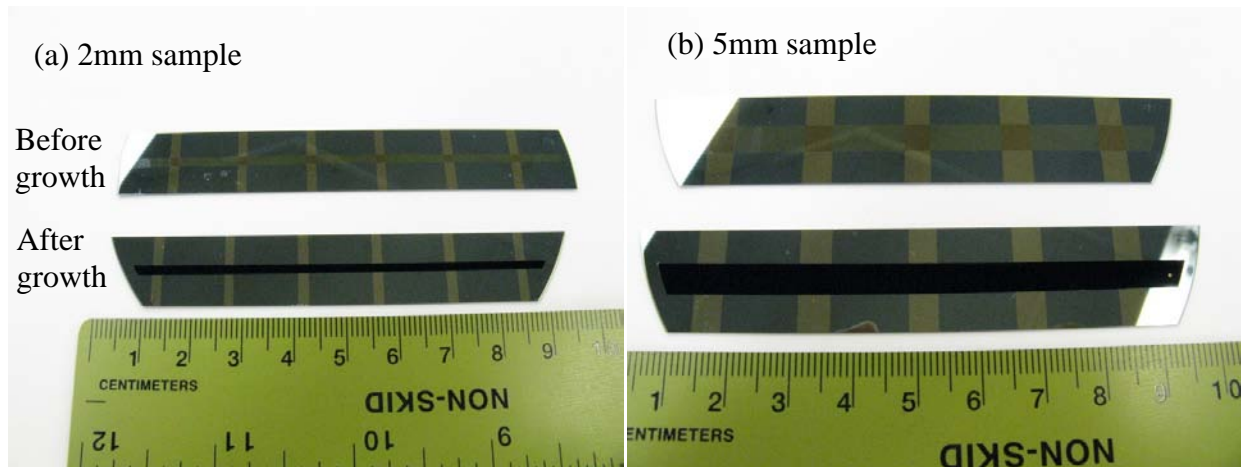
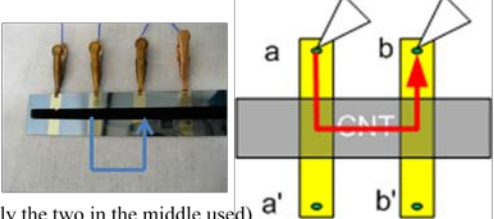
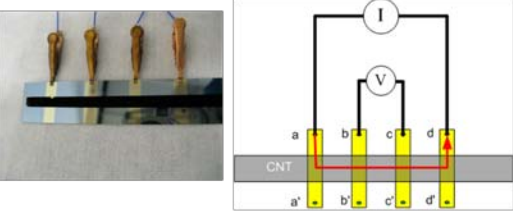
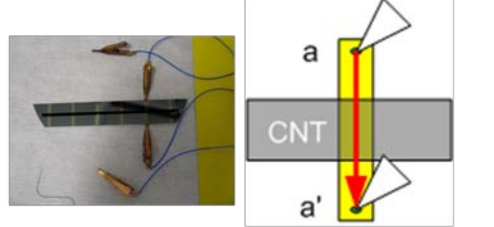
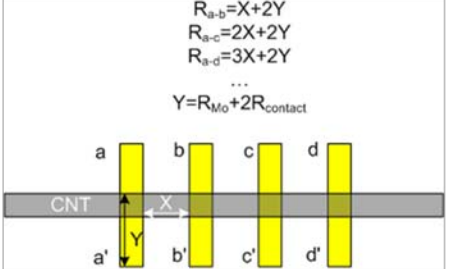


Figure 2.8. Fabricated CNT samples using “tape mask” and the test setup. (a) and (b): CNT resistors with widths of 2mm and 5mm, respectively.

Four types of measurement schemes have been conducted as listed in table 2.2, including: (1) two probe measurement to monitor the repeatability between units and batches; (2) four probe measurement to derive the sheet resistance of CNTs; (3) sheet resistance of Mo (the contact resistances between clamps and Mo pads are ignored as they are measured at about only 2Ω , much lower than the measured sheet resistance for Mo layer), and (4) contact resistances as illustrated in the table by solving the equations or plotting them in a figure.

Table 2.2. Measurements for CNT samples made by the “tape mask” method.

| | |
|--|--|
| <p>1. Two-probe measurement (R_{a-b})</p> | <p>2. Four probe measurement (sheet resistance of CNT)</p> |
|  <p>(Only the two in the middle used)</p> |  |
| <p>3. Sheet resistance of Mo ($R_{a-a'}$)</p> | <p>4. Contact resistance</p> |
|  |  $R_{a-b} = X + 2Y$ $R_{a-c} = 2X + 2Y$ $R_{a-d} = 3X + 2Y$ <p>...</p> $Y = R_{Mo} + 2R_{contact}$ |

2.2.3 Results and repeatability

Table 2.3 summarizes the measurement results. The measurements and data process are quite similar to those to be discussed in the other method in next section. As the latter method is more complex, we skip talking about the details of this method to avoid redundancy and leave the thorough discussion to next section. One possible concern on the repeatability is addressed in Figure 2.9. Four different samples grown in different batches have been characterized and results show minimum variations across these samples. These linear curves also reveal that the contacts between CNT and Mo must be ohmic.

Table 2.3. Overview of experimental results from tape mask methods

| | 5mm sample | 2mm sample |
|--|------------------------|------------------------------|
| Sheet resistance of Mo (Ω/\square) | $29.1\Omega \pm 10\%$ | $29.8 \pm 6.2\%$ |
| Sheet resistance of CNT (Ω/\square) | $122.6\Omega \pm 35\%$ | $118.0 \pm 9.8\%$ |
| contact resistance between Mo and CNT | N/A | $\sim 100\Omega$ per contact |

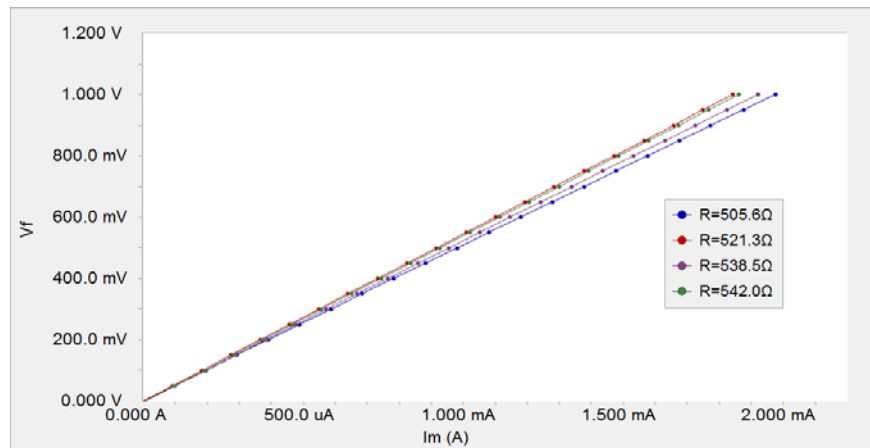


Figure 2.9. Sample repeatability tests using two probe measurement of CNT (5mm case, four samples from different growth batches)

2.3 Material characterization using photo masks

Photomasks have been used in this section to define fine features for the CNT forests testing structures. Four distinct designs have been adopted to characterize the contact and sheet resistances of vertically aligned CNT forests with bottom metal contacts. One technical challenge of the study was to extract the contact resistance out of measurements that often contain unwanted resistive components. Inspired by the traditional semiconductor industry [26], we used (1) transfer length method (TLM) design, (2) contact chain design, (3) Kelvin design, and (4) four-point probe design to measure the contact resistance. Because these designs have

certain limits due to various built-in approximations, all the four schemes have been implemented and compared.

2.3.1 Design

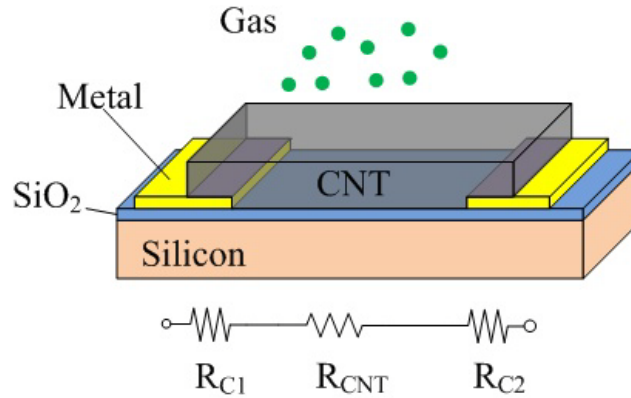


Figure 2.10. Schematic diagram of a testing structure used to characterize the electrical properties of the CNT forest and the demonstrative gas sensing application. The lateral sheet resistance of the CNT forest, R_{CNT} , and two CNT-metal contact resistances, R_{C1} and R_{C2} , are key components of the overall resistance of the device. When exposed to gas, the resistance of the CNT forest changes with respect to different species/concentrations of gases.

Figure 2.10 illustrates the basic design configuration. A silicon wafer is used as the supporting substrate and a layer of thermal oxide is grown first as the insulation layer. The metal layer, molybdenum (Mo), is used to define the contact pad areas as well as metallic interconnects. The total resistance of the device includes three components: the lateral sheet resistance of the CNT forest, R_{CNT} , and two CNT-metal contact resistances, R_{C1} and R_{C2} . For simplicity, the CNT-metal contact interface and the CNT forest on that area are treated as a whole, hereby referred to as the contact resistance in this study. The resistances of the Mo contact pads and aluminum bonding wires are small as compared to the CNT resistance and neglected. The bottom of figure 2.10 shows a simplified equivalent electrical circuit model including key elements for the overall resistance. When exposed to gas, the resistance of the CNT forest changes with respect to different species/concentrations of gases such that this structure could be readily used as a gas sensor.

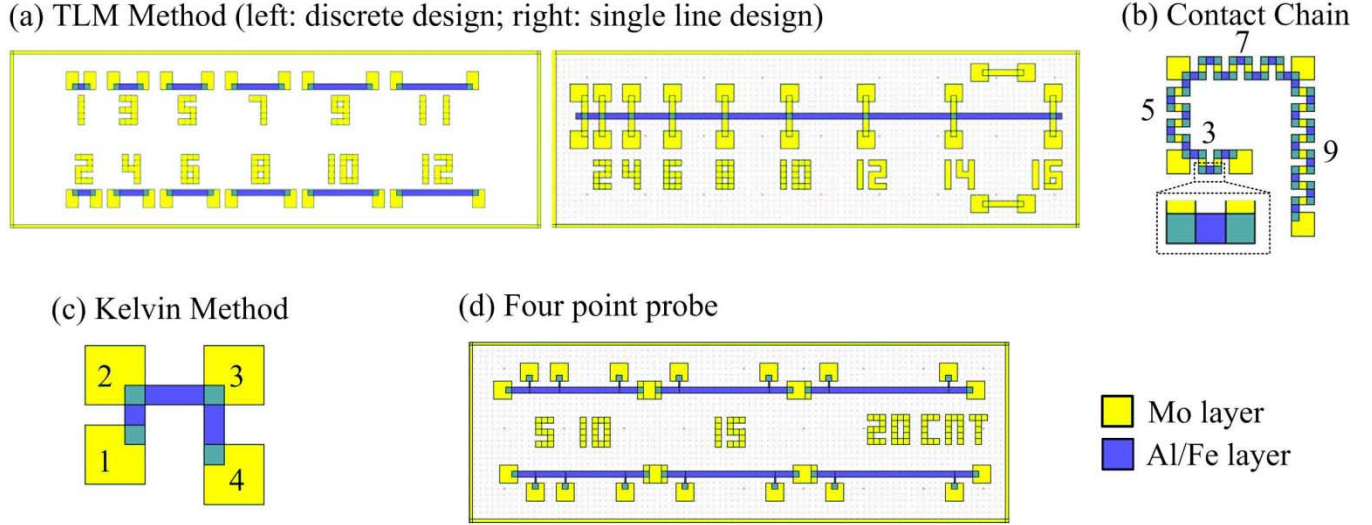


Figure 2.11. Device layouts of the four testing designs to characterize the sheet and contact resistances of CNT forests: (a) transfer length method (TLM), (b) contact chain design, (c) Kelvin design, and (d) four-point probe design. There are two design variations for the TLM design: the one on the left is the discrete case and the one on the right is the single-line case where adjacent devices share the contact pads.

Figure 2.11(a)-(d) show the layouts of the four designs used in this work to characterize the contact and sheet resistances of CNT forests. In all designs, CNT forests (blue color in figure 2.11) are $100\mu\text{m}$ in width with variable lengths; each CNT-to-Mo contact area of is $100\times 100\mu\text{m}^2$ in size, and the wire-bonding pads are $300\times 300\mu\text{m}^2$.

In figure 2.11(a), the TLM design includes a serial of CNT forest structures (devices) with identical contact pads but gradually increasing CNT resistor lengths. Therefore, the resistance of each device can be described as:

$$R_M = x \cdot R_{CNT,\square} + 2R_C \quad (2-3)$$

where R_M is the measured resistance, x is the number of squares of the CNT forest stripe between the two contact pads. One basic assumption is that the two contacts have the same contact resistance because the design configurations are symmetric and the process conditions are the same. There are two unknowns in the equation (2-3): the sheet resistance, $R_{CNT,\square}$, and the contact resistance, R_C . Mathematically, two independent equations (designs) would be enough to determine the two unknowns. However, data from only two samples often leads to large experimental errors, especially if one of the unknowns has a much smaller value than the other. Therefore, a serial of CNT samples with different CNT square numbers ranging from 1 to 16 squares have been designed to average out the possible errors. The abundant data allows us to establish a curve between the number of squares, x , and total resistances, R_M . A linear relationship is expected where the slope of the line is the sheet resistance, $R_{CNT,\square}$, and the offset of the y-axis is twice that of the contact resistance, R_C . Furthermore, two different layout designs including the discrete case and the single-line case have been implemented in the experiments. The discrete case represents the classic TLM design using separate devices, while the single-line

case uses a single long CNT stripe such that the adjacent devices can share the common contact pads. The latter design reduces the number of contact pads by half and conserves the device area. Note that the measurements in the single-line design were done only between adjacent pads (*i.e.*, there was no additional pad between the measurement pads), thereby reducing analytical complexity.

The contact chain design in figure 2.11(b) resembles the TLM design with several differences: (1) the length of the CNT stripe between the contact pads is the same as one square of the CNT forest, and (2) the bonding pads are made only at the two ends of the whole CNT stripe. Therefore, each “chain” is measured only once. For example, there are four chains in figure 2.11(b) with 3, 5, 7 and 9 repeating units with adjacent chains sharing the bonding pads. In each chain, the measurement can be quantified as:

$$R_M = x \cdot (R_{CNT,\square} + 2R_C) \quad (2-4)$$

where $(R_{CNT,\square} + 2R_C)$ is the resistance of a repeating unit, as shown in the enlarged portion of figure 2.11(b). Similar to the TLM design, the resistance contributions made by the metal (Mo) square between repeating units is ignored. Compared to the TLM design, this design increases the relative weight of the contact resistance in the final measurements, because there are multiple contacts (2^x) within a chain device, compared to only two contact areas in a TLM device. Using a similar plotting method as described for the TLM design, a linear relationship between R_M and $(R_{CNT,\square} + 2R_C)$ can be determined. The slope is the resistance of one repeating unit. By combining results from the contact chain design with the four point probe design to be discussed later that independently measures the sheet resistances, one can calculate the contact resistance, R_C . Another advantage of the chain design is the convenience of assessment for the yield and repeatability across large quantities of contacts by a single test.

The third design is the Kelvin structure which is a simple test structure to characterize contact resistance as illustrated in figure 2.11(c). A constant current (I_0) flows from pad#1 to pad#2 and a voltmeter is used to measure the voltage difference between pad#3 and pad#2. Assuming the voltmeter has an infinite internal resistance such that there is no current (voltage drop) from the CNT portion on pad#2 to pad#3, the voltage drop between pad#3 and #2 is, therefore, the same as the voltage drop through the contact interface between the CNT and pad#2. Thus, one single measurement reveals the contact resistance (R_c) as:

$$R_C = \frac{V}{I_0} \quad (2-5)$$

Similar measurements can be repeated among pad#2, #3, and #4 as well in figure 2.11(c). The length of the CNT portion between the contact pads is theoretically irrelevant to the final results. The simplicity in terms of structure and measurement makes this design very attractive. However, unlike the previous two designs where the contact resistance can be reliably extracted from a plotting method using multiple data sources, the Kelvin design only generates one independent result, leading to a relatively larger volatility. Despite the limitation, the Kelvin structure still provides an effective and simple alternative way to characterize contact resistance.

Figure 2.11(d) shows the four point probe design, which is well-known to eliminate the effect of contact resistances and the sheet resistance can be calculated by using the equation:

$$R_M = x \cdot R_{CNT,\square} = \frac{V}{I_0} \quad (2-6)$$

where x is the number of CNT squares between the two middle probes, V is the measured voltage drop between the two middle probes and I_0 is the applied constant current. Due to the advantages of microfabrication processes, the middle probes in our design are only 20 μm in width, which enables higher accuracy for measuring the voltage and counting the squares. As described previously, when combined with the contact chain design, contact resistances can be derived.

2.3.2 Fabrication

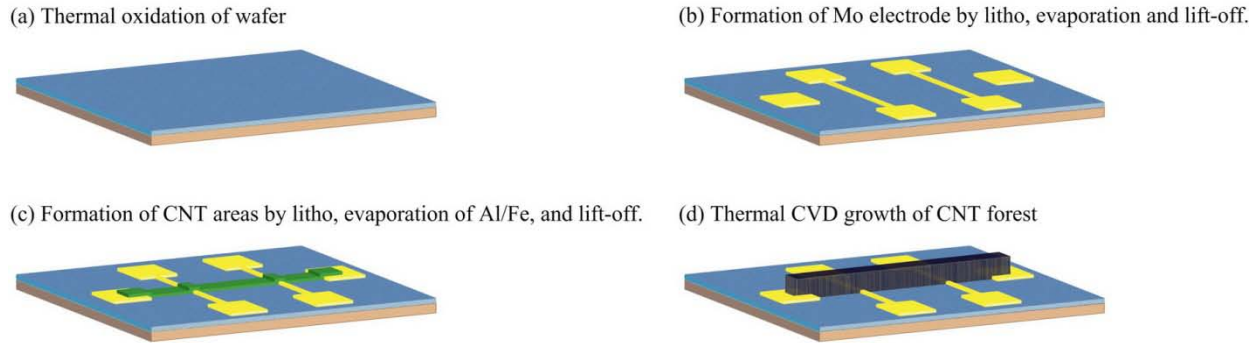


Figure 2.12. Fabrication process for the CNT forest-based device. A four point probe layout is used for illustration purposes. The main process steps are: (a) oxidation of silicon wafer, (b) deposition of patterned contact metal (Mo) for bonding pads and interconnections, (c) deposition of patterned CNT catalyst (Al/Fe), and (d) thermal CVD growth of CNT forest.

Figure 2.12 shows the fabrication process. First, a silicon wafer is thermally oxidized to provide an electrically insulating substrate. Afterwards, the first lithography step is used to define the bonding pads as well as other electrically conductive areas. Using the lift-off process, 50nm-thick molybdenum (Mo) is deposited by evaporation and patterned. The CNT growth areas are defined by a second aligned lithography. Using a second lift-off process, aluminum (Al) and iron (Fe) are evaporated with a thickness of 10nm and 5nm, as supporting and catalyst layer, respectively. Finally, thermal CVD growth of the CNTs is achieved in a 2-inch quartz tube with pre-mixed ethylene (C_2H_4) and hydrogen (H_2) gas flow at a ratio of 611:90 (unit: sccm). The growth temperature is set at 720 $^\circ\text{C}$ and the growth time is controlled to be 10min. These parameters result in CNT forests of approximately 100 μm in height. The device is finally mounted to a ceramic package and connected using wire bonding. Figure 2.13(a) shows a ready-to-test sample that was mounted onto a bread board and Figure 2.13(b) is the cross-sectional view at the bottom corner of a patterned CNT forest stripe. Vertically aligned CNTs can be clearly identified. The optical picture in figure 2.13(c) shows TLM samples with different lengths and the numbers in the photo correspond to the number of squares of different samples. The major problem we experienced in the process is that some CNT stripes incidentally broke at the edge between the regions with and without the Mo bottom layer possibly due to uneven

growth caused by the bottom Mo layer. Fortunately, most fabrication runs don't have this problem and we believe this issue can be eventually eliminated by optimization of the fabrication process.

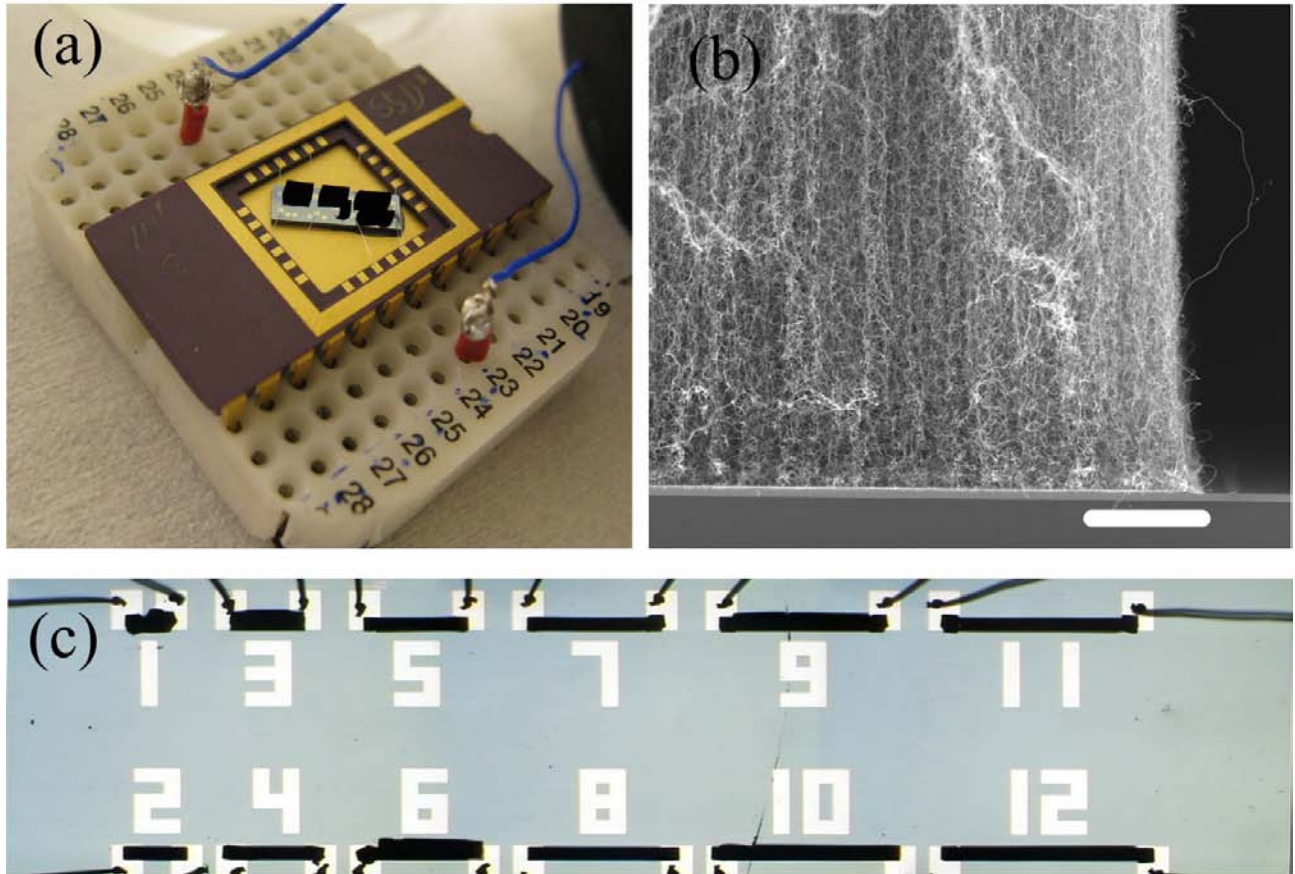


Figure 2.13. Fabricated samples. (a) A ready-to-test sample mounted onto a bread board. For visualization purposes, the CNT samples are grown much longer than $100\mu\text{m}$ in height in this example. (b) The cross sectional view at the bottom corner of a patterned CNT forest structure. The bar is $6\mu\text{m}$. (c) Optical picture of TLM samples (discrete case) with varying number of CNT squares. The width of CNT stripes is $100\mu\text{m}$. The numbers on the substrate correspond to the total number of squares of the CNT forest devices.

2.3.3 Results and discussions

Measurement results are presented in figures 2.14(a)-(d). Figure 2.14(a) shows results from the TLM design (single line case) with a linear relationship between R_x and the total number of squares. The slope of the line is the sheet resistance of the CNT forest and the y-axis offset represents the value of $2R_C$. Two sets of up to 16-square resistor samples have been measured, and minor fluctuations along the best linear fit line have been observed. The unusual large deviations in sample #1 for tests on the “12” and “16 square” samples are due to the formation of cracks of the CNT forest at the intersection between the oxidized substrate and the metal pads as discussed previously. Figure 2.14(b) shows results from the contact chain design. A linear relationship between R_x and the number of repeating units was clearly observed as expected. Because these contacts were connected in serial, any single bad contact would have resulted in accumulative large measurement errors. However, since only small fluctuations were observed,

this implies good repeatability of the contacts between the CNT forests and the metal. Measurement results from the Kelvin design are shown in figure 2.14(c) and these data were collected from individual samples which results in relatively large fluctuations. The measured contact resistances are in the range of 30-80 Ω for 10 individual samples and the average contact resistance is calculated as 49 Ω . Finally, results from the four-point probe design are plotted in figure 2.14(d) with expected linear behavior and the sheet resistance is calculated as 95.5 Ω/\square .

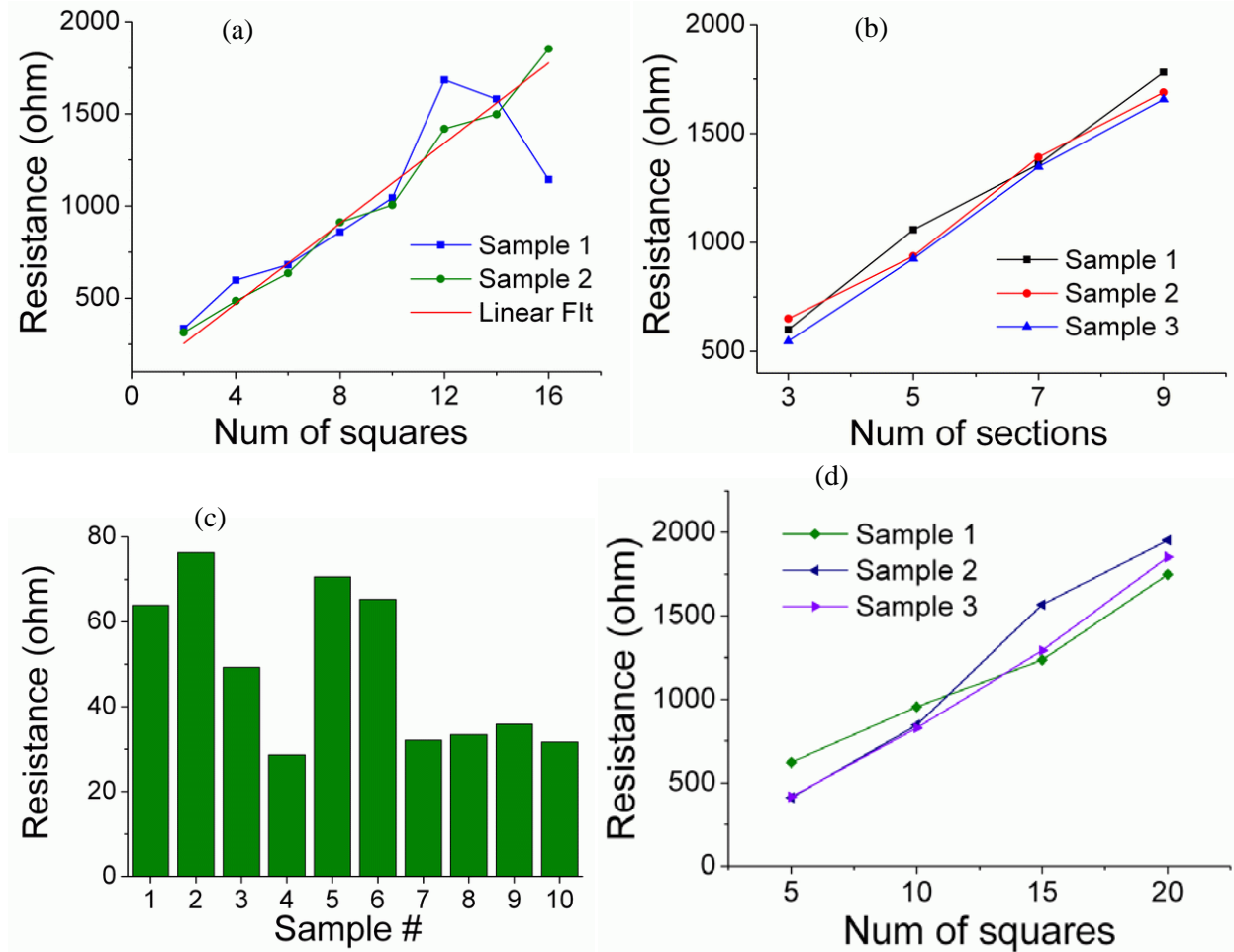


Figure 2.14. Experimental results from the four testing designs. (a) TLM design using different lengths of CNT forest samples and two contacts. (b) Contact chains design using repeating units comprised of two metal contacts and one square of CNT forest. (c) Kelvin design. A known current flows through CNT-metal contacts while the voltage drop through the interface is measured from nearby pads. (d) Four point probe design.

Table 2.4 summarizes the calculated results and standard deviations based on the data shown in figure 2.14 from the four different designs. In general, the sheet resistance of the 100 μm (H) \times 100 μm (W) CNT forest is approximately 100 Ω/\square from both the TLM and four point probe designs. The contact resistance of the CNT forest and Mo is roughly 50 Ω for a contact area of 100 \times 100 μm^2 from the TLM, contact chain, and Kelvin designs. From the results presented in ref [23] which used CNT forest with evaporated Ti/Au as top electrode and TiN substrate, a contact resistance of 4.72 $\times 10^4 \Omega \cdot \mu\text{m}^2$ can be calculated, which is about one order of magnitude lower than this work at 5 $\times 10^5 \Omega \cdot \mu\text{m}^2$. The major reason is that CNT contacts with different metal

layers could make big differences. Other parameters in the growth process (temperature, gas concentration ...) are also factors to result in different contact resistance. The single-line case of TLM design has standard deviation of 30Ω for contact resistance, larger than the measured contact resistance value, 18Ω. This comes from the fact that contact resistance is relatively small compared to the CNT forest's bulky resistance such that the possible measurement errors for the CNT sheet resistance dominate the calculations. This can be cleared by considering results from other designs as presented in this work. Therefore, measurements from multiple independent designs, instead of a single design, provide more reliable characterizations results.

Furthermore, the resistivity of the CNT forest can be calculated from the sheet resistance equation:

$$R_{CNT,\square} = \frac{\rho_{CNT}}{H_{CNT}} \quad (2-7)$$

where ρ_{CNT} represents the resistivity of the CNT forest and H_{CNT} is the height of the forest. One can obtain a CNT forest resistivity of about 1Ω·cm (alternatively, a conductivity of 1 Ω⁻¹·cm⁻¹), which is consistent with some of the prior reports [21, 22]. The sheet resistance of the same type CNT forest with different heights can be calculated accordingly.

Table 2.4. Summary of the calculated results of the four designs. The contact area is 100×100μm² in all samples. The CNT forest test sample is 100μm in height and 100μm in width.

| Design | TLM (discrete) | TLM (single line) | Contact Chain | Kelvin Design | Four Probe Design |
|-------------------------------|----------------|-------------------|---------------|---------------|-------------------|
| Sheet resistance (Ω/□) | 99.3(±3.3) | 108(±6) | N/A | N/A | 95.5±4.7 |
| Contact resistance (Ω) | 62(±12) | 18(±30) | <43.5(±4) | ~49 | N/A |

For practical applications, it is important to further investigate the long-term stability of the CNT samples. For this purpose, resistance characterizations were conducted again after the initial measurements and the storage of the samples in an unsealed box for two months. Figures 2.15(a) and (b) show representative experimental results of the samples using the single-line TLM and contact chain designs, respectively. In general, resistance changes after 2 months were minimal, with slight increase and decrease of resistance in figures 2.15(a) and (b), respectively. The relatively larger variations in figure 2.15(a) for the “2” and “4 square” samples were likely caused by pre-existing cracks on the CNT forests. Without counting these two data, the maximum resistance changes in both samples are only 0.9%. Considering the small variations in these experiments, as well as the possible influences of gas and moisture in the air, the CNT forest structures were able to maintain their resistance values remarkably well.

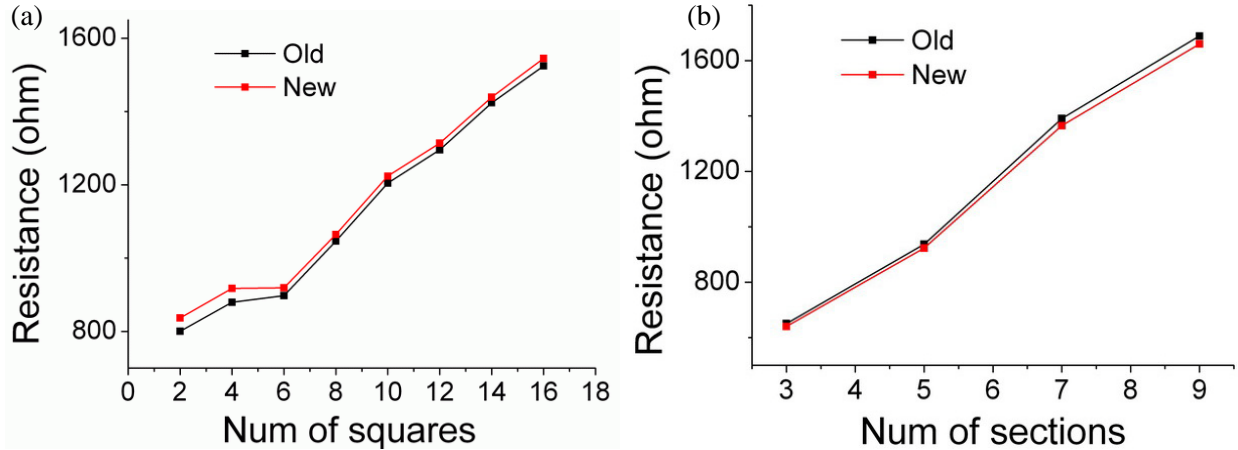


Figure 2.15. Resistance measurement results from initial data and after storage in open-air condition for 2 months. (a) Single-line TLM design; (b) contact chain design.

2.3.4 Gas sensor demonstration

Many research groups have used individual CNT and disoriented CNT networks as a sensing material [27-32]. J. Kong *et al.* made chemical sensors based on individual SWNTs and observed the conductance of the SWNT sample to significantly decrease with response times of 1-2 min after exposure to 1% NH_3 [27] but the sensor required hours to recover most of its original resistance under the ambient condition. Electrothermal effects of a single MWNT have also been demonstrated for pressure and gas sensing applications [28]. Recently researchers have used disoriented CNT network as gas sensors with good sensitivity and stability [29, 30] and both sensitivity and selectivity of CNT-based sensors have been further enhanced by the functionalization of the CNTs [31, 32]. Compared to the gas sensors based on individual CNTs or CNT networks, vertically aligned CNT forests could be beneficial in terms of yield and reproducibility. For example, M Penza *et al.* have reported a miniaturized gas sensor to monitor landfill gases using metal-modified, aligned CNT forests [33]. The CNT forest samples presented in this work can be readily employed as chemiresistor gas sensors. In contrast to the aforementioned prior works where electrodes were deposited on top of the CNT forest [33], this work can use the metal bottom electrodes without extra deposition.

NH_3 was chosen for gas sensing demonstration and possible comparison with results from other similar works. Figure 2.16(a) shows the experimental setup where a prototype device was placed inside a sealed bottle. The chamber was filled with NH_3 of different concentrations and vented with air alternatively. A constant voltage was applied on the CNT samples and the current was monitored simultaneously to obtain the CNT resistance values. When exposed to NH_3 , a rapid increase of CNT resistance was observed. Afterwards, air was used to purge the chamber and the resistance of the CNT sample returned to the initial value, as shown in figure 2.16(b). The experimental results suggest that the absorption of NH_3 gas molecules on CNTs hinders the electron transfer process within the tubes such that the resistance is increased. Conversely, desorption process of NH_3 molecules during the air venting process leads to a recovery of the initial resistance. Furthermore, the detection process is quick and reversible. Preliminary results show that the sensor responding time is about 1~2 minute with a broad sensing range for NH_3 concentration from 0.5 to 1000ppm and a minimum demonstrated resolution of 0.5ppm.

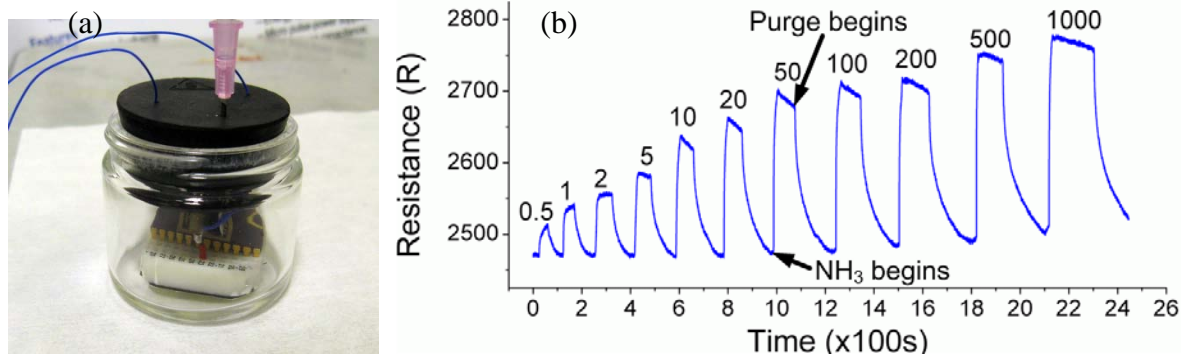


Figure 2.16. Gas sensing of CNT forest. (a)Homemade test setup, (b) Sensing results with different NH₃ gas concentrations. The arrows give the example when the NH₃ and air were pushed in. The unit of NH₃ in the figure is ppm.

Based on a single semiconductor SWNT (single-walled CNT) device, ref [27] has reported about 100 times conductance reduction when it was exposed to 1% NH₃ and only 1.5 time reduction for SWNT mat. The CNT forest gas sensor here has about 1.12 times resistance increment at 1000ppm (0.1%) NH₃. Several differences between these devices contribute the variations. First, semiconducting SWNT could be much more sensitive to exterior influences than either metallic SWNT or MWNT as much reduced sensitivity was reported in ref [27] by using a single metallic SWNT. Second, in contrast to longitudinal electron moving direction along the SWNT, electrons move laterally on the vertically-aligned CNT forest or perpendicular to the longitudinal direction of CNTs. Nevertheless, the sensitivity of the prototype device is in the same order of magnitude as the SWNT mat. Furthermore, the prototype device has a time response of 1~2 mins which is also comparable with the previous report in ref [27] of 2min for a single semiconducting SWNT, yet better than 10min for SWNT mat. One possible reason is that MWNT forest has large intervals between individual CNTs for fast transports of gas molecules.

References

- [1] Ali Javey and Hongjie Dai, Regular Arrays of 2 nm Metal Nanoparticles for Deterministic Synthesis of Nanomaterials, *J. AM. CHEM. SOC.*, 2005, 127, pp.11942
- [2] Guangyu Zhang, David Mann, Li Zhang, Ali Javey, Yiming Li, Erhan Yenilmez, Qian Wang, James P. McVittie, Yoshio Nishi, James Gibbons, and Hongjie Dai, Ultra-high-yield growth of vertical single-walled carbon nanotubes: Hidden roles of hydrogen and oxygen, *PNAS*, 2005, 102(45), pp.16141
- [3] Masahiro Horibe, Mizuhisa Nihei, Daiyu Kondo, Akio Kawabata and Yuji Awano, Carbon Nanotube Growth Technologies Using Tantalum Barrier Layer for Future ULSIs with Cu/Low-k Interconnect Processes, *Japanese Journal of Applied Physics*, 2005, 44(7A), pp.5309
- [4] Nathan R. Franklin, Qian Wang, Thomas W. Tomblor, Ali Javey, Moonsub Shim, and Hongjie Dai, Integration of suspended carbon nanotube arrays into electronic devices and electromechanical systems, *Applied Physics Letters*, 2002, 81(5), pp.913

- [5] Wei-Chang Li, Yingqi Jiang, Robert A. Schneider, Henry G. Barrow, Liwei Lin and Clark T.-C. Nguyen, Polysilicon-filled Carbon Nanotube Grass Structural Material for Micromechanical Resonators, *IEEE MEMS 2011*, Cancun, MEXICO, January 23-27, 2011
- [6] YeoHeung Yun, Vesselin Shanov, Yi Tu, Srinivas Subramaniam, and Mark J. Schulz, Growth Mechanism of Long Aligned Multiwall Carbon Nanotube Arrays by Water-Assisted Chemical Vapor Deposition, *J. Phys. Chem. B*, 2006, 110, pp.23920
- [7] Kenji Hata, Don N. Futaba, Kohei Mizuno, Tatsunori Namai, Motoo Yumura, Sumio Iijima, Water-Assisted Highly Efficient Synthesis of Impurity-Free Single-Walled Carbon Nanotubes, *Science*, 2004, 306, pp.1362
- [8] Wahed Wasel, Kazunori Kuwana, Peter T.A. Reilly, Kozo Saito, Experimental characterization of the role of hydrogen in CVD synthesis of MWCNTs, *Carbon*, 2007, 45, pp.833
- [9] R. H. Baughman, A. A. Zakhidov, and W. A. de Heer, Carbon nanotubes—the route toward applications, *Science*, 2002, 297, pp.787
- [10] A. Jorio, G. Dresselhaus and M. S. Dresselhaus, *Carbon nanotubes: synthesis, structure, properties and applications*, Berlin: Springer, 2008
- [11] A. M. Cassell, J. A. Raymakers, J. Kong and H. Dai, Large scale CVD synthesis of single-walled carbon nanotubes, *J. Phys. Chem. B*, 1999, 103, pp.6484
- [12] V. L. Pushparaj, M. M. Shaijumon, A. Kumar, S. Murugesan, L. Ci, R. Vajtai, R. J. Linhardt, O. Nalamasu and P.M. Ajayan, Flexible energy storage devices based on nanocomposite paper, *Proc. Natl. Acad. Sci.*, 2007, 104, pp.13574
- [13] D. T. Welna, L. Qu, B.E. Taylor, L. Dai, M. F. Durstock, Vertically aligned carbon nanotube electrodes for lithium-ion batteries, *J. Power Sources*, 2011, 196, pp.1455
- [14] Y. Jiang, P. Wang and L. Lin, Contact and sheet resistances of carbon nanotube forest in gas sensing applications, *IEEE MEMS conf. 2011*, Cancun, Mexico, January 2011
- [15] K. Banerjee, H. Li and N. Srivastava, Current Status and Future Perspectives of carbon nanotube interconnects, *8th IEEE Conf. on Nanotechnology*, Arlington, TX, August 2008
- [16] S. Frank, P. Poncharal, Z. L. Wang and W. A. de Heer, Carbon nanotube quantum resistors, *Science*, 1998, 280, pp.1744
- [17] B. Q. Wei, R. Vajtai and P.M. Ajayan, Reliability and current carrying capacity of carbon nanotubes, *Appl. Phys. Lett.*, 2001, 79, pp.1172.
- [18] A. Javey, J. Guo, Q. Wang, M. Lundstrom and H. Dai, Ballistic carbon nanotube field-effect transistors, *Nature*, 2003, 424, pp.654
- [19] T. Kawano, D. Christensen, S. Chen, C.Y. Cho and L. Lin, Formation and Characterization of Silicon/Carbon Nanotube/Silicon Heterojunctions by Local Synthesis and Assembly, *Appl. Phys. Lett.*, 2006, 89, pp.163510.
- [20] L. Hu L, D. S. Hecht and G. Gru1ner, Percolation in transparent and conducting carbon nanotube networks, *Nano Lett.*, 2004, 4, pp.2513

- [21] D.J. Yang, S.G. Wang, Q. Zhang, P.J. Sellin and G. Chena, Thermal and electrical transport in multi-walled carbon nanotubes, *Phys. Lett. A*, 2004, 329, pp.207
- [22] C.T. Lin, C.Y. Lee, T.S. Chin, R. Xiang, K. Ishikawa, J. Shiomi and S. Maruyama, Anisotropic electrical conduction of vertically-aligned single-walled carbon nanotube films, *Carbon*, 2011, 49, pp.1446
- [23] N. Chiodarelli, S. Masahito, Y. Kashiwagi, Y. Li, K. Arstila, O. Richard, D. J. Cottl, M. Heyns, S.D. Gendt, G. Groeseneken and P.M. Vereecken, Measuring the electrical resistivity and contact resistance of vertical carbon nanotube bundles for application as interconnects, *Nanotechnology*, 2011, 22, pp.085302
- [24] S. Talapatra, S. Kar, S.K. Pal, R. Vajtai, L. Ci, P. Victor, M.M. Shaijumon, S. Kaur, O. Nalamasu and P.M. Ajayan, Direct growth of aligned carbon nanotubes on bulk metals, *Nature Nanotech.*, 2006, 1, pp.112
- [25] Y. Jiang, Q. Zhou and L. Lin, Planar MEMS supercapacitor using carbon nanotube forests, *IEEE MEMS 2009 conf.*, Sorrento, Italy, January 2009.
- [26] D.K. Schroder, *Semiconductor material and device characterization 3rd ed.*, John Wiley & Sons: Hoboken, New Jersey, 2006.
- [27] J. Kong, N. R. Franklin, C. Zhou, M. G. Chapline, S. Peng, K. Cho and H. Dai, Nanotube molecular wires as chemical sensors, *Science*, 2000, 287, pp.622
- [28] T. Kawano, H.C. Chiamori, M. Suter, Q. Zhou, B. D. Sosnowchik and L. Lin, An electrothermal carbon nanotube gas sensor, *Nano Lett.*, 2007, 7, pp.73686
- [29] J. Li, Y. Lu, Q. Ye, M. Cinke, J. Han and M. Meyyappan, Carbon nanotube sensors for gas and organic vapor detection, *Nano Lett.*, 2003, 3, pp.929
- [30] E. S. Snow, F. K. Perkins, E. J. Houser, S. C. Badescu, T. L. Reinecke, Chemical detection with a single-walled carbon nanotube capacitor, *Science*, 2005, 307, pp.1942
- [31] A. Star, V. Joshi, S. Skarupo, D. Thomas and J. P. Gabriel, Gas, Sensor array based on metal-decorated carbon nanotubes, *J. Phys. Chem. B*, 2006, 110, pp.21014
- [32] T. Zhang, S. Mubeen, E. Bekyarova, B. Y. Yoo, R. C. Haddon, N. V. Myung and M. A. Deshusses, Poly(m-aminobenzene sulfonic acid) functionalized single-walled carbon nanotubes based gas sensor, *Nanotechnology*, 2007, 18, pp.165504
- [33] M. Penza, R. Rossi, M. Alvisi and E. Serra, Metal-modified and vertically aligned carbon nanotube sensors array for landfill gas monitoring applications, *Nanotechnology*, 2010, 21, pp.105501

Chapter 3 MEMS CNT supercapacitors

In this chapter, single-layer, planar MEMS supercapacitors utilizing CNT forests electrodes are described. One technical challenge is the synthesis of CNT on top of silicon substrates with a conductive under layer for possible integration with MEMS structures. It is found that the combination of Mo/Al/Fe metal stack has good CNT forest synthesis results and high electrical conductivity. Prototype devices show measured specific capacitances about 1000 times higher than those with plain metal electrodes without CNT forests. Furthermore, charging/discharging experiments show over 92% efficiency and very robust cycling stability. As such, these planar MEMS supercapacitors could be applicable in various systems including energy harvesters, pulse-power supplies and advanced microelectronics as on-chip capacitors.

3.1 Introduction

Supercapacitors have simple configuration, stable performance (millions cycles vs. ~1000 cycles of Li-ion batteries [1]), and less temperature dependency, making them suitable as the main power sources for short-term, high power-density usages in many applications. The possibility of making “single-layer, planar” supercapacitors instead of conventional sandwiched structures could inspire interesting applications in the area of on-chip supercapacitors for advanced microelectronics. Previously, the concept of “planar supercapacitor” has been investigated. For example, Sung et al. have used conducting polymer-coated planar metal layers [2] to make supercapacitors. In another work, In et al used KOH etching to increase the surface area of silicon where gold layer and carbon paint were deposited as the electrodes [3]. Carbon nanotubes (CNT) are well-known for its high surface area-to-volume ratio and good conductivity such that several groups have been investigating the possibility for applications in large-scale supercapacitors. For example, An et al. have deposited random CNT network as electrodes [4], in which contact resistance among tubes as well as contact to the substrate are major technical challenges. Pushparaj et al. have proposed and demonstrated a sophisticated process by transferring CNT arrays to a conductive substrate after the synthesis process [5]. So far no CNT-based planar architecture has been yet demonstrated.

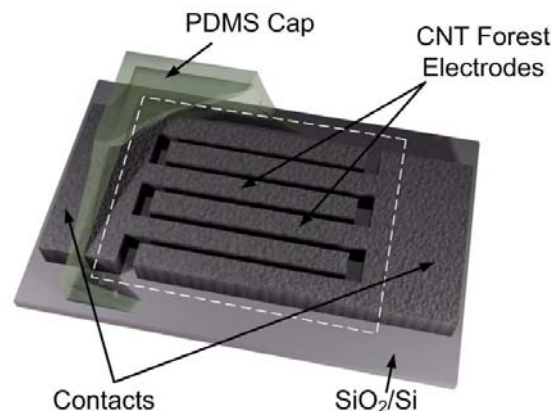


Figure 3.1. Schematic of the planar micro supercapacitor using aligned, 3D CNT forest electrodes.

In this chapter, we present a simple yet versatile planar MEMS supercapacitor using porous CNT forests as electrodes with low contact resistance. Figure 3.1 shows the schematic diagram of a planar supercapacitor with a top cap to contain liquid electrolyte. Unlike the conventional sandwich structure, the two electrodes are made on the same plane for possible on-chip integration with MEMS devices and/or CMOS microelectronics. Other advantages of this design include height reduction and simplification of the fabrication process (no electrode assembly). The travelling distance of ions in the electrolyte, a major performance factor in supercapacitors, can be well defined by the finger distance while eliminating the necessity of a separator.

3.2 CNT growth on conductive substrate

In chapter 2, CNT forests have been synthesized using Al (10nm, supporting layer) and Fe (5nm, catalyst layer), respectively (refer to table 2.1). However, it is found that the resistance of the metal layer goes up drastically, e.g. from 7.5Ω to $16.7K\Omega$ (two-probe measurement), after the CNT growth. The high resistance value significantly degrades the performance of a supercapacitor by increasing the internal resistance. Therefore, it is crucial to reduce this resistive hurdle. However, CNTs grow predominantly on non-conducting substrates [6]. Some groups avoid the issues by synthesizing CNTs on non-conducting substrates and transferring CNT forest to a conductive substrate [5], or conducting a post-growth metal deposition process [7] to achieve low resistance. However, for our device, the silicon substrate is important for possible direct integration with other MEMS or microelectronics. Therefore, existing methods are not suitable for us. A way of directly growing CNT on conductive layer and silicon substrate is first studied.

Extensive experiments have been conducted to investigate the quality of CNT and their contact resistance to the substrate. To make condition consistent, thermally oxidized silicon wafers were used as the common insulating substrate and 5nm Fe layer as the common catalyst. Table 3.1 summarizes the experimental results. Resistances were measured with a pair of probes with constant distance of about 5mm on $2cm \times 2cm$ CNT samples. Two trends were observed and Al and Mo were the representative metals. Al is a well-known metal suitable for the synthesis of CNT as described in chapter 2 for thick and densely aligned CNT forest. However, although the Al layer initially exhibited low resistance of about 10Ω , its resistance jumped to $16k\Omega$ at the end of the CNT synthesis process. In the similar high temperature process, the resistance of Mo layer reduced from $\sim 200\Omega$ to 40Ω . However, Mo is experimentally proved not to be a good substrate material for the growth of CNTs. Other metals have also been investigated such as Ti, Cr and Ni and they showed resistance characteristics somehow between the behaviors of Al and Mo. None of them could produce densely grown CNT forests plus low conductive substrate. The combination of Mo/Al layer, however, produced very satisfactory results with densely grown CNTs and low resistance. It is possible that the insertion of Al layer prohibits the alloying of Mo and Fe, which would otherwise make Fe lose its catalytic activities on the formation of CNTs. Meanwhile, the thin layer of aluminum could produce Al_2O_3 , a well-known material for the growth of CNT as described in chapter 2. It is noted that similar success has also been achieved by using the recipe of W/Al stack layer. Further study should be investigated for better understandings of the role of these materials.

Table 3.1. Synthesis of CNT forests on different metal substrates with the same synthesis conditions of 720°C, with reaction gas of C₂H₄ and H₂ at a flow rate of 90 and 611 sccm and atmospheric pressure. The number in the brackets is the thickness of the metal layer (unit: nm). The resistance unit is ohm. All SEMs are at the same scale and the bar in Ti SEM is 2μm.

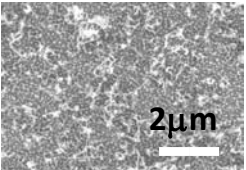
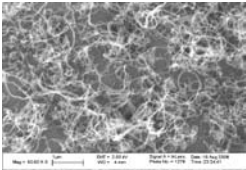
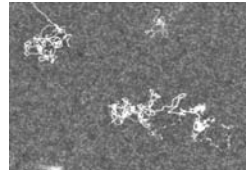
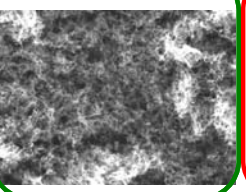
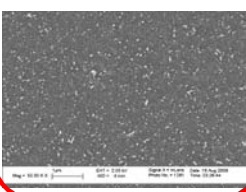
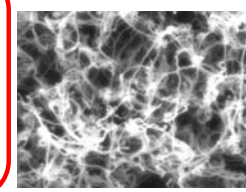
| Metal type | Ti (50) | Cr (50) | Ni (50) |
|------------------------------|--|---|--|
| Resistance before growth, R1 | 145 | 140 | 21 |
| Resistance after growth, R2 | 11.7k | 49.6k | 373 |
| Ratio of R2/R1 | >80 | >354 | >17 |
| CNT profile | Short and sparse | Long but sparse | Hardly any |
| SEM pictures |  |  |  |
| Metal type (cont.) | Al (50) | Mo (50) | Mo/Al (50/10) |
| Resistance before growth, R1 | 7.5 | 233 | 216 |
| Resistance after growth, R2 | 16.7k | 40 | 26 |
| Ratio of R2/R1 | >15560 | ~0.17 | ~0.12 |
| CNT profile | Thick and dense | No at all | Thick and dense |
| SEM pictures |  |  |  |

Figure 3.2 shows synthesized CNT forests by using the combination layer of Mo/Al/Fe. The width/gap of the porous CNT electrodes was 40μm/20μm in (a) and (b) and 60μm/30μm in (c) and the height is about 80μm in all photos. Figure 3.2(d) shows a broader overview of a sample of 2mm in width, with very uniform growth of CNT forests. A close view in figure 3.2(e) shows that each individual CNT is directly connected to the substrate and the “dense” forests are highly porous. Figure 3.2 (f) is a close-up view of the CNTs to show their diameters of only around 20nm.

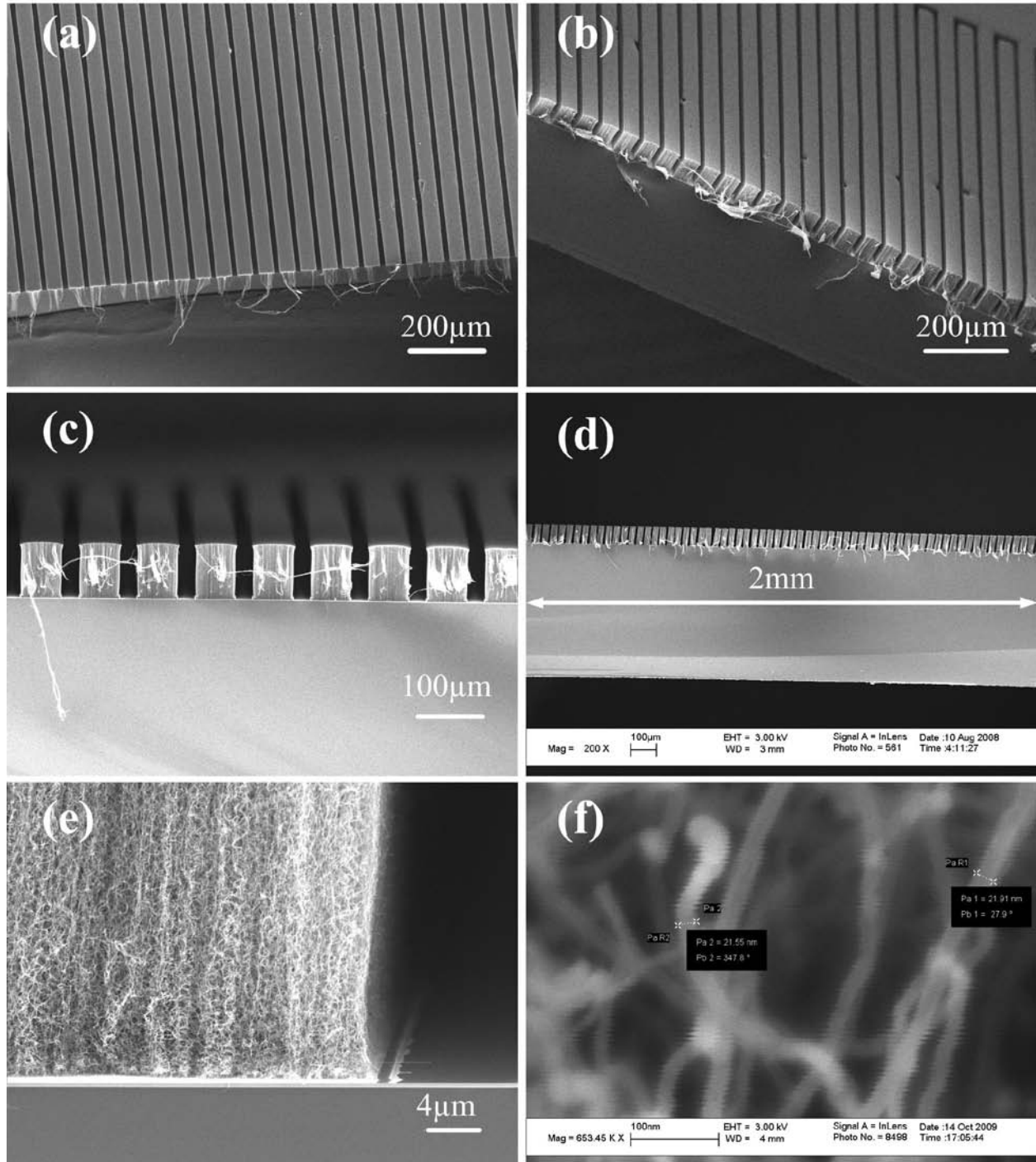


Figure 3.2. SEM pictures of interdigital CNT electrodes grown on the Mo/Al/Fe stack layer. (a) Top view; (b) oblique view; (c) cross-section view; and (d) a broader 2mm-wide cross-sectional view. (e)& (f) Close views of the contact section and individual CNTs, respectively.

3.3 Fabrication

3.3.1 Compatibility of microfabrication

One unique advantage of CNT forests over other nanomaterials is that it could be easily fabricated into micro-scale patterns by using standard lithography process to pattern the catalyst layer. CNTs forests only grow where catalyst layer exists. Figure 3.3 shows some growth examples: (a) “wall”-shape as thin as $4\mu\text{m}$ in thickness; (b) letters; (c) pillars with $3\mu\text{m}$ in diameter; and (d) close view of (c) showing the diameter is uniform. These samples demonstrate the capability of making MEMS structures using CNT forests.

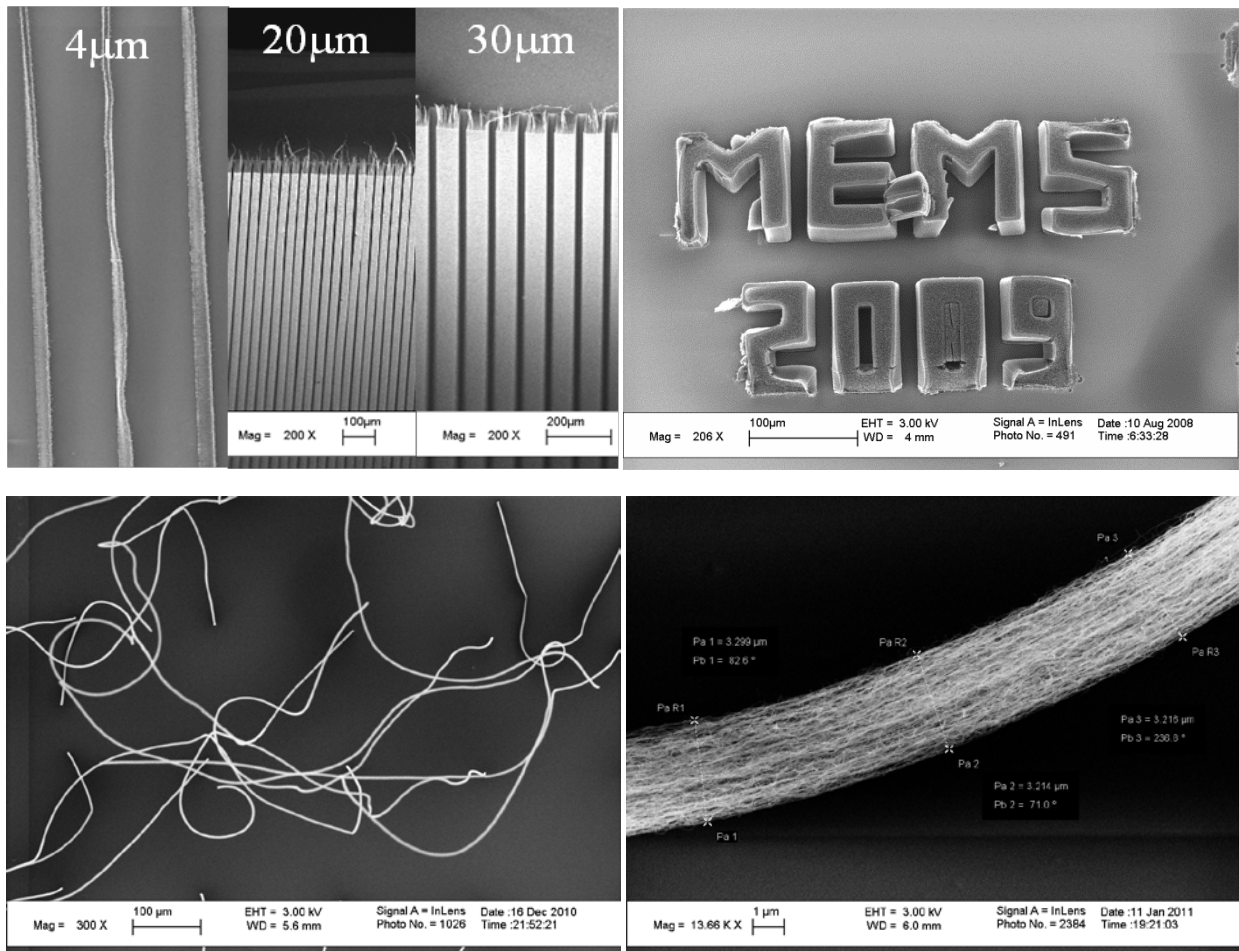


Figure 3.3. Various patterns of CNT forests. (a) Walls with thickness of $4\mu\text{m}$, $20\mu\text{m}$, and $30\mu\text{m}$, respectively. (b) “MEMS” letters. (c) CNT pillars with a diameter of $3\mu\text{m}$. (d) Close view of a section of pillar showing dense deposition of CNTs.

3.3.2 Fabrication process

The fabrication process of a CNT MEMS supercapacitor, as shown in figure 3.4, begins with thermal oxidation of a bare silicon wafer to isolate the substrate from the electrodes in Fig. 3.4(a). Lithography is followed in Figs. 3.4 (b)&(c), to pattern two comb-shape interdigital electrodes. Afterwards, Fig. 3.4 (d) illustrates that Mo, Al, and Fe are evaporated onto the substrate in sequence with a thickness of 50nm, 10nm, and 5nm, respectively. A photo resist lift-off is followed to remove the metals on unwanted areas in Fig. 3.5(e). Thermal chemical vapor deposition (CVD) furnace (Lindberg/Blue M® three-zone tube furnace, Thermo Electron Corp., Asheville, NC) is used to grow the CNTs in Fig. 3.5(f). The furnace is firstly pumped to vacuum to remove air, then filled with pure hydrogen, and heated up to 720°C. Subsequently, the mixed gas of ethylene and hydrogen with flow rates of 90sccm and 611sccm is flowed through the quartz tube for 10 minutes. Finally the tube is cooled down to room temperature with the help of a fan. Appendix A shows the detailed experimental setup. Electrical contacts were formed by bonding wires to the CNT electrodes with silver epoxy paste. 1-Butyl-3-methylimidazolium tetrafluoro-borate ([BMIM][BF₄]) ionic liquid (Sigma-Aldrich inc., MO) was used as the electrolyte and the final assembly was done by covering the sample with a PDMS cap (or ring). Ionic liquid is preferred over aqueous electrolyte because of its high breakdown voltage of ionic liquid. Detailed fabrication protocol and layout explanation can be found in Appendix B.

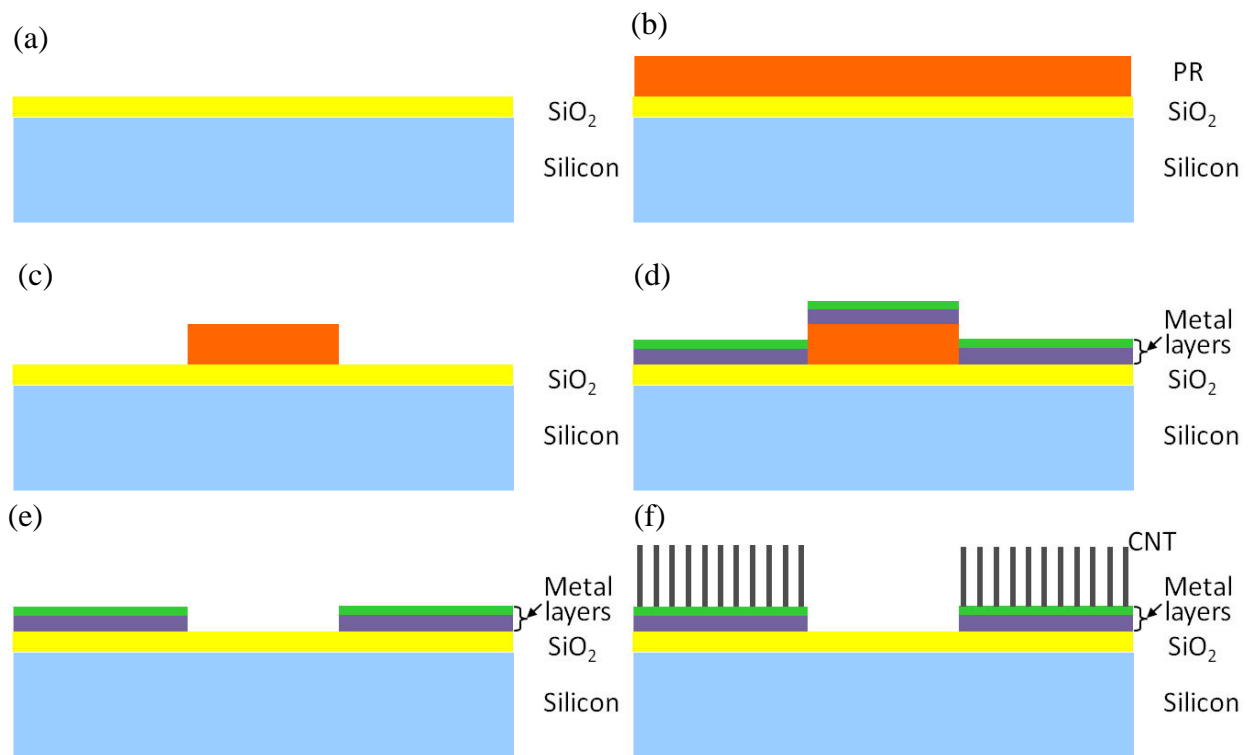


Figure 3.4. Fabrication process of the MEMS supercapacitor using as-grown CNT forest electrodes. (a) Thermal oxidation; (b)&(c) lithography processes to pattern the electrodes; (d) e-beam evaporation of Mo/Al/Fe catalyst layer (Al and Fe are represented together as the green color); (e) lift-off; and (f) thermal CVD furnace growth.

Figure 3.5 shows the assembled prototype. The CNT electrode area was 5mm×7mm with about 30 comb fingers on a single electrode. As demonstrated in section 3.3.1, the CNT MEMS structures can be easily scaled down by using smaller mask patterns.

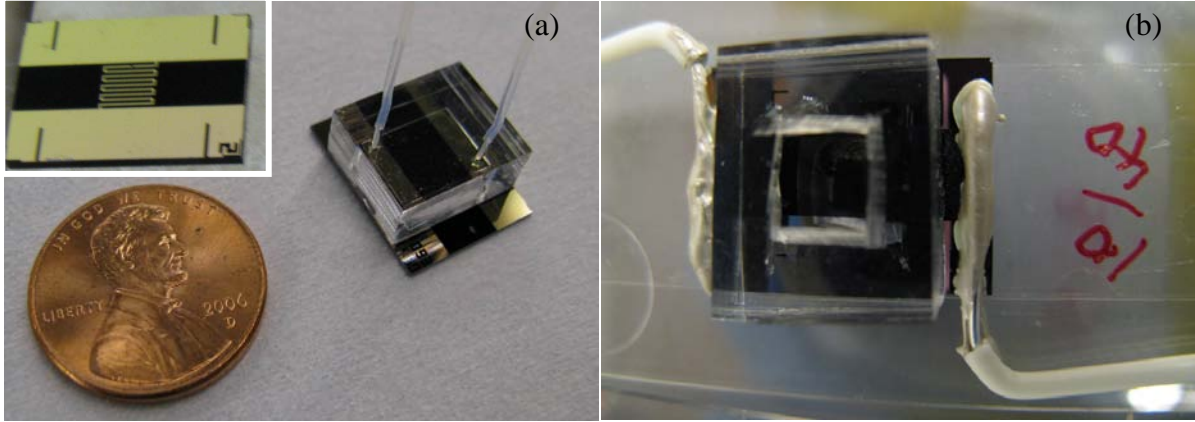


Figure 3.5. Assembled MEMS CNT supercapacitor prototypes. A PDMS cap (a) or ring (b) was used to contain the electrolyte. The inset in (a) shows an uncovered sample. The device is connected to the test equipment by bonding wires with silver paste to the CNTs. The whole devices are mounted onto a glass slide using double-side tapes.

3.4 Results

The characterization of the CNT supercapacitor was conducted by the CHI 750A electrochemical workstation (CH Instruments, Inc. USA). Figure 3.6 shows the cyclic voltammetry curves of supercapacitors using CNT forest electrodes. As can be seen, these supercapacitors has a very symmetric rectangular shape (the ideal supercapacitor should have a perfect rectangular shape). When normalized to the unit area, the specific capacitance of the CNT-based supercapacitor can be calculated by:

$$C_{sp} = \frac{I}{dV/dt} \cdot \frac{1}{A} \quad (3-1)$$

Here, I is the current at $V=0$; dV/dt is set manually on the equipment and 50mV/sec is used in all experiments as shown in Figure 3.6. A is the effective CNT forest area exposed to electrolyte, 26.7mm^2 (this value is less than the visible $5\text{mm} \times 7\text{mm}$ area because we exclude the artificial gap area between two electrodes.). Therefore, the capacitance of a single device was calculated as $149.7\mu\text{F}$ and specific capacitance as $428\mu\text{F}/\text{cm}^2$. As a comparison, we also plot the supercapacitor using the identical Mo/Al/Fe electrode but without CNT forests in the same coordinate system. It is observed that the CV curve with no CNT forests was squeezed into a “straight line”. An enlarged view is shown on the upper left corner. Comparing the current level, the CNT supercapacitor has roughly three orders of magnitude higher than those with plain metal electrodes. It is noted that this ratio was consistent among dozens of tested samples and it confirms the benefit of using CNT forests as the electrodes.

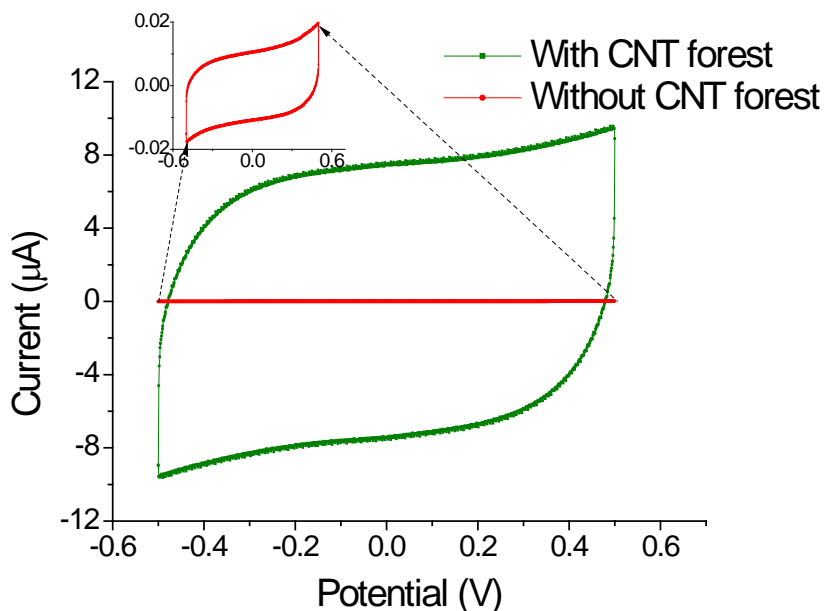


Figure 3.6. Cyclic voltammetry curves of the samples with (green) and without (red) CNT forests electrodes. Scanning rate is 50mV/sec. The inset shows an enlarged view of the curve of bare-metal sample. The units are the same in both coordinates.

The profiles of CV curves could be changed by simply changing the scanning rate. According to Eq. (3-1), if the scanning rate, dV/dt , is increased, the current magnitude increases accordingly. Figure 3.7 shows experimental results on a prototype CNT electrode (note different from the one used in figure 3.6). A close look indicates that the current and the scanning rate don't have a perfect linear relationship as predicted by Eq. (3.1). The main reason is that it is more difficult for the ions in the electrolyte to catch up the scanning speed as the scanning rate increases.

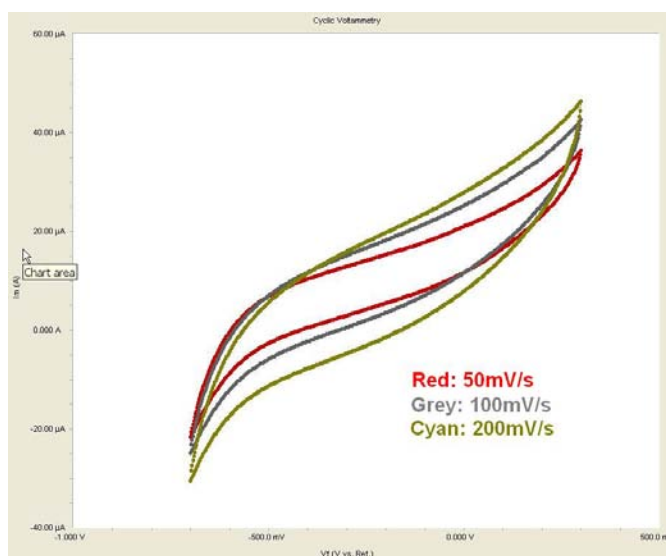


Figure 3.7. Effects of the scanning rate. As the scanning rate increase, the current magnitude increases accordingly.

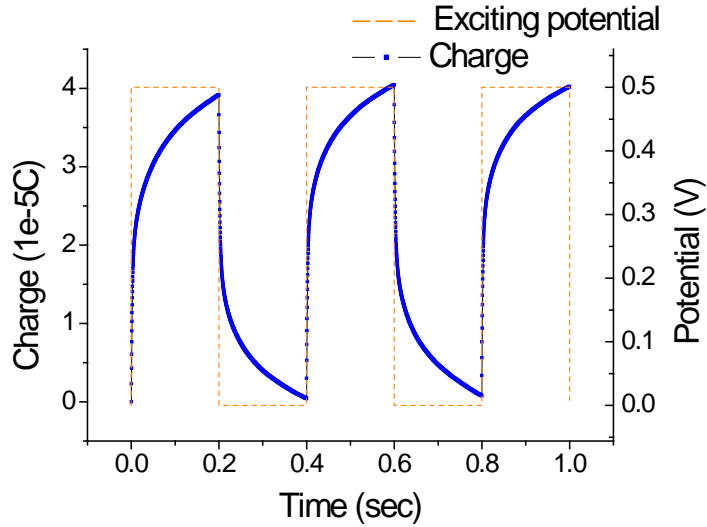


Figure 3.8. Chronocoulometry curve of the CNT supercapacitor. The device was charged and discharged under a square-wave voltage toggling between 0.5V and 0V at a period of 0.4s per cycle.

Figure 3.8 shows the chronocoulometry curve, presenting the charge/discharge capacity of our device. It is observed that the prototype supercapacitor has high charge/discharge efficiency which is defined as the charge entering the device and the charge moving out of the device (the difference is consumed by internal consumption) of more than 92%. Furthermore, an average power density of $0.28\text{mW}/\text{cm}^2$ was calculated using the following equation.

$$\bar{P} = \frac{\Delta Q V_0}{\Delta t} \cdot \frac{1}{A} \quad (3-2)$$

where ΔQ is the charge accumulated during the charge session, Δt is the time for the charge period, V_0 is the applied constant charge voltage, and A is the effective plane electrode area. Figure 3.9 shows the charge efficiency for 10 continuous cycles. The results seem to improve over time, probably due to better penetration/diffusion of electrolyte into the CNT forests.

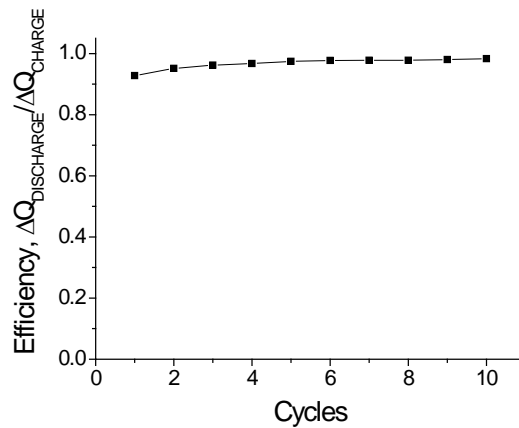


Figure 3.9. Efficiency variation during 10 continuous charge/discharge cycles. An excellent efficiency of over 92% was observed for robust operations.

3.5 Discussions

3.5.1 Material utilization efficiency

To investigate how well the ionic liquid interacts with CNT forest, we evaluate the theoretical maximum capacitance for our current device. The capacitance of the supercapacitor can be expressed based on a parallel-plate capacitor as:

$$C = \frac{\varepsilon_0 \varepsilon_r A}{d} \quad (3-3)$$

where ε_0 is the permittivity of the vacuum, $8.854 \times 10^{-12} \text{F/m}$. ε_r is the relative permittivity of the electrolyte, 11.7 for [BMIM][BF₄] [8]; d is the double-layer thickness, also electrolyte-dependent parameter at 0.69nm [9], and A is the overall surface area of electrodes. Because CNT forests are made of multi-walled carbon nanotubes with a diameter of about 30nm in this work, a value of $110 \text{m}^2/\text{g}$ is used as an approximation of surface-to-mass ratio [10]. Experimentally, the mass of CNT forests on a prototype device of $5 \times 7 \text{mm}^2$ in size with effective electrode area of 26.7mm^2 and CNT forest thickness of $80 \mu\text{m}$ is at about $3 \times 10^{-5} \text{g}$, which results in an estimated total surface area of $3.3 \times 10^{-3} \text{m}^2$. Noticing this mass include both electrodes, such that the area in Eq. (3-3) should be $1.65 \times 10^{-3} \text{m}^2$. Substituting these values into the equation, we get the theoretical supercapacitor capacitance as $248 \mu\text{F}$ for a single electrode. Therefore, the theoretical measured value should be $124 \mu\text{F}$ (due to two EDLC connected in serial). It is actually smaller than the measured value of $149.7 \mu\text{F}$. The more than 100% usage may be because the value of $110 \text{m}^2/\text{g}$ underestimates the true situation. However, pretty good match itself suggests that the CNTs are indeed close to be fully wetted in ionic liquid electrolyte.

3.5.2 Specific capacitance

In literature, instead of total device capacitance, volumetric or mass specific capacitance (or say normalized capacitance) is often used. Figure 3.6 presents a close-to-ideal rectangular shape. Previously we have calculated the total capacitance is $149 \mu\text{F}$ using the equation

$$C_{total, bare \text{ CNT}} = \frac{I}{\frac{dV}{dt}} \quad (3-4)$$

$C_{total, bare \text{ CNT}}$ is the device capacitance; I is the current (half of the gap); and dV/dt is the scanning rate and calculated the CNT area is 26.7mm^2 . Because the height (thickness) of CNT forests is $80 \mu\text{m}$, the total volume of CNT electrode is:

$$V_{CNT} = 26.7 \text{mm}^2 \times 80 \times 10^{-6} \text{m} = 2.14 \times 10^{-3} \text{cm}^3 \quad (3-5)$$

When specific capacitance is considered, only the data on a single electrode should be used. For capacitance part, $C_{EDLC} = 2 \cdot C_{TOTAL}$ (C_{EDLC} is the EDLC generated by one electrode. C_{TOTAL} is the measured capacitance) because C_{TOTAL} is the total capacitance of two C_{EDLC} in serial. For volume part, the volume of a single CNT electrode is half of the total, $V_{CNT}/2$. Therefore,

$$C_{sp,bare\ CNT} = \frac{2 \cdot C_{total}}{\frac{V_{CNT}}{2}} = \frac{4 \times 149\mu F}{2.14 \times 10^{-3} cm^3} = 278mF/cm^3 \quad (3-6)$$

To calculate the mass energy density, the mass density of the CNT forests is estimated by measuring a large area CNT electrode and calculating the smaller CNT electrode area accordingly.

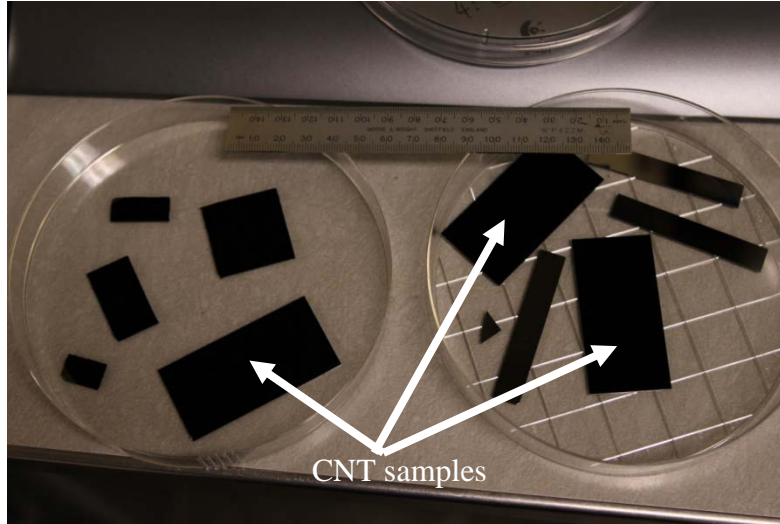


Figure 3.10. CNT Samples used to calculate the mass density.

The large CNT forest samples as shown in Figure 3.10 have a size of 5cm (L) ×2cm (W) and their thicknesses (H) were estimated under SEM. The mass of each CNT forest sample was estimated by calculating the mass difference before and after the CNT growth process as listed in Table 3.2 for different CNT heights.

Table 3.2. Density calculation of CNT forests

| Before(g) | After(g) | Δm (mg) | H(um) | V(cm ³) | Density(10 ⁻³ g/cm ³) |
|-------------------|---------------|-----------------|-------------|---------------------|--|
| S1: 2.1791/2.1794 | 2.1848/2.1850 | 5.65 | 717 | 1.2906 | 4.378 |
| S2: 2.1773/2.1771 | 2.1833/2.1830 | 5.95 | 453 | 0.8154 | 7.297 |
| S3: 2.1862/2.1862 | 2.1888/2.1890 | 2.7 | 145.2/158.4 | 0.27324 | 9.881 |
| S4: 2.1826/2.1826 | 2.1865/2.1865 | 3.9 | 233.2/241.2 | 0.42696 | 9.134 |

Based on these results, a conservative number of 10mg/cm³ or 0.01g/cm³ is used in this study and the number is consistent with other published values for CNT forests [11]. This approach would underestimate our energy density calculations as:

$$C'_{sp,bare\ CNT} = \frac{C_{sp,bare\ CNT}}{\rho} = 27.8F/g \quad (3-7)$$

References

- [1] B. E. Conway, *Electrochemical Supercapacitors: Scientific Fundamentals and Technological Applications*, Kluwer Academic/Plenum Publishers, New York, 1999.
- [2] J.H. Sung, S.J. Kim, and K.H. Lee, Fabrication of microcapacitors using conducting polymer micro- electrodes, *J. Power Sources*, 2003, 124, pp.343
- [3] H.J. In, S. Kumar, Y. Shao-Horn, and G. Barbastathis, Nanostructured Origami™ 3D Fabrication and Assembly of Electrochemical Energy Storage Devices, *Proc 2005 IEEE on Nanotechnology*, Nagoya, Japan, July 2005
- [4] K.H. An, W.S. Kim, Y.S. Park, Y.C. Choi, S.M. Lee, D.C. Chung, D.J. Bae, S.C. Lim, and Y.H. Lee, Supercapacitors Using Single-Walled Carbon Nanotube Electrodes, *Adv. Mater.*, 2001, 13, pp.497
- [5] V.L. Pushparaj, M.M. Shaijumon, A. Kumar, S. Murugesan, L.J. Ci, R. Vajtai, R.J. Linhardt, O. Nalamasu, and P.M. Ajayan, Flexible energy storage devices based on nanocomposite paper, *PNAS*, 2007, 104, pp.13574
- [6] S. Talapatra, S. Kar, S.K. Pal, R. Vajtai, L. Ci, P. Victor, M.M. Shaijumon, S. Kaur, O. Nalamasu and P.M. Ajayan, Direct growth of aligned carbon nanotubes on bulk metals, *Nature nanotechnology*, 2006, 1, pp.112
- [7] C. T. Lin, C. Y. Lee, T. S. Chin, R. Xiang, K. Ishikawa, J. Shiomi and S. Maruyama, Anisotropic electrical conduction of vertically-aligned single-walled carbon nanotube films *Carbon*, 2011, 49, pp.1446
- [8] C. Wakai, A. Oleinikova, M. Ott, and H. Weingartner, “How Polar Are Ionic Liquids? Determination of the Static Dielectric Constant of an Imidazolium-based Ionic Liquid by Microwave Dielectric Spectroscopy”, *J. Phys. Chem. B*, 2005, 109, pp.17028
- [9] http://www.utexas.edu/research/chemed/lagowski/WSSP/houston_2006_paper_maass_katie.pdf
- [10] <http://www.cheaptubes.com/MWNTs.htm>
- [11] Zu-Po Yang, Lijie Ci, James A. Bur, Shawn-Yu Lin, and Pulickel M. Ajayan, Experimental Observation of an Extremely Dark Material Made By a Low-Density Nanotube Array, *Nano Letters*, 2008, 8(2), pp.446

Chapter 4 CNT forests with embedded nickel nanoparticles as supercapacitor electrodes

MEMS supercapacitors using pristine CNT forest electrodes have been described in the previous chapter. In order to further increase the energy density of the supercapacitor, the idea of CNT pseudo capacitor is proposed and demonstrated in this chapter. Integrated (functionalized) with metal oxide or conducting polymer, a pseudo capacitor could produce higher capacitance than the traditional EDLC-based supercapacitor [1-3]. In this chapter, the functionalization of CNT forests with uniform nickel nanoparticles is discussed as shown in figure 4.1. When the CNT electrode decorated with nickel hydroxide nanoparticle is immersed in KOH electrolyte, the energy storage capability of the supercapacitor is further enhanced by utilizing the reversible chemical reactions of nickel hydroxide, Ni(OH)_2 to NiO(OH) as shown in equation (4-1) [4-6]. The energy density of the supercapacitor using functionalized CNT electrodes was measured up to one order higher than those with pristine CNT electrodes. After robust operation of more than 1000 times of charge/discharge tests, little degradation is observed on the CNT forest electrodes or the embedded nickel nanoparticles.

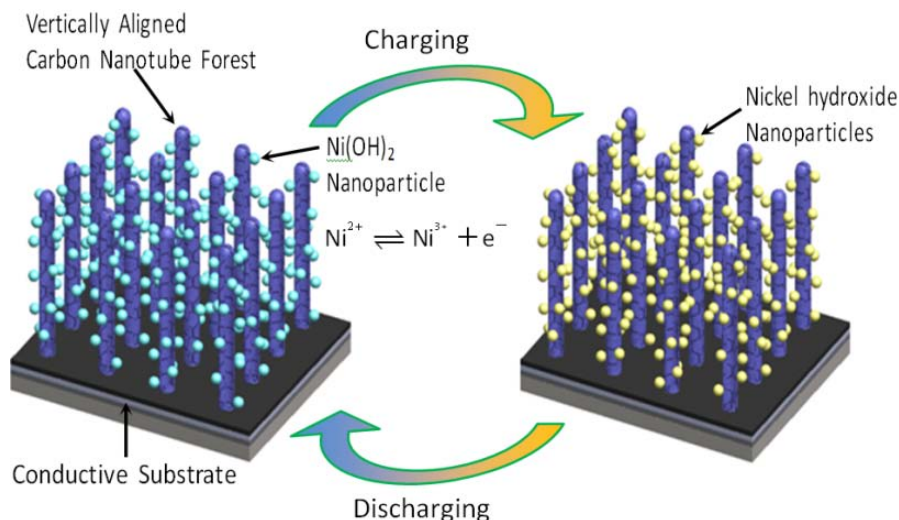
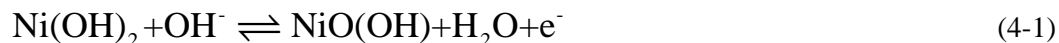


Figure 4.1. Schematic diagram of a functionalized CNT supercapacitor using CNT forests with embedded nickel nanoparticles as the electrode. The charge storage and release processes are realized by reducing and oxidizing nickel ions between Ni^{2+} and Ni^{3+} , respectively.



4.1. Introduction

The EDLC (surface area-based) type supercapacitors can be further improved in the area of their energy density by the idea of pseudo-capacitors [1-3], where metal oxide or conducting polymer is added into the electrode to introduce pseudo capacitance. The possible energy density enhancement could be many times or even orders of magnitude higher than EDLC-based

structures. For this work, our goal is to realize fully functionalized high aspect ratio of CNT forests. Similar directions have been explored before but not suitable for our case. Many of the publications reported on functionalized CNTs using only individual CNTs [7] or disoriented CNT films [8]. Mechanical stirring is the common method to combine large amounts of CNTs with functionalization materials [9], yet it could destroy the alignment and MEMS structure of CNT forests that are valued in this study. Physical depositions, such as evaporation and sputtering, can only form a thin-film of several micrometers on the top surface of the CNT forests [10]. Gas based methods such as LPCVD have been demonstrated success using silicon [11] and parylene [12], but none of them are among the interested functionalization materials. As a result of above, liquid-based depositions, particularly electroplating process, could be a good scalable process suitable for this work.

4.2. CNT functionalization

4.2.1. Method selection

The well-known hydrophobicity of CNT forests [13] makes the electroplating process difficult. Figure 4.2 shows a set of pictures CNT samples after conventional electroplating of nickel. It is observed that nickel was deposited on the top surface of the CNT forest but didn't reach further inside the forest.

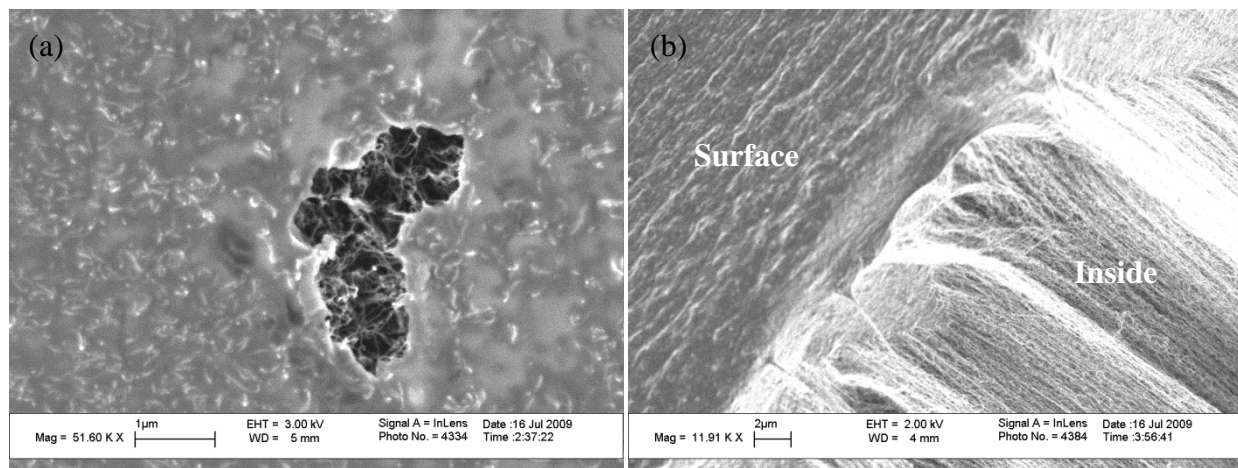


Figure 4.2. CNT forest samples after a conventional nickel electroplating process. (a) Top view SEM photo of the CNT forests with an opening as the result of manual scratch by a metal tip. (b) Cross-sectional view of the CNT forests due to a natural crack as the result of the drying process. Both photos demonstrate that the electroplating process only occurs on the surface of the CNT forests.

Four possible methods have been tested to overcome the issue of hydrophobicity: (1) surface oxidation to turn hydrophobic surface to hydrophilic surface; (2) ultrasonic excitation to drive liquid electrolyte deep into the CNT forest; (3) IPA mixture as the liquid media for lower surface tension and possible better liquid penetration into the CNT forest; and (4) the vacuum infiltration process. The first approach has utilized a combination of $\text{HNO}_3 + \text{H}_2\text{SO}_4$ and solely H_2O_2 as the oxidants, respectively. In both cases, CNTs can easily peel off from the substrate as these oxidants might have attacked and etched the bottom metal layers (Mo or Al). In the process of

ultrasonic excitation, the mechanical vibration was too strong for the CNT forests to break themselves into pieces. In the process of using IPA (a bi-polar solvent) as the media, we disappointedly found that IPA is also difficult to penetrate into CNT forests. So there was no success story on the first three approaches.

4.2.2. Vacuum infiltration method

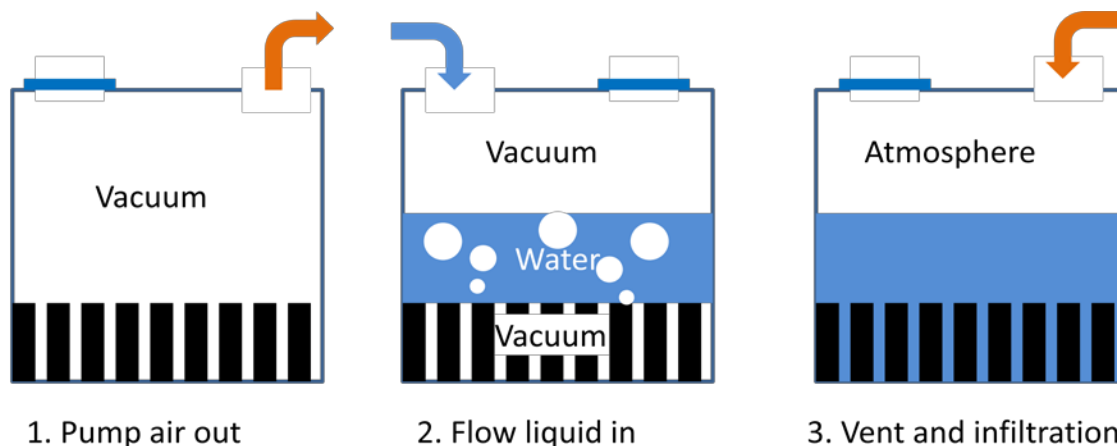


Figure 4.3. Vacuum infiltration procedure

The procedure of the vacuum infiltration method is shown in figure 4.3, which is composed of three steps: (1) pumping air out of CNT forests in a vacuum chamber, (2) applying DI (de-ionized) water to cover the sample, and (3) venting the chamber and the air pressure pushes liquid into the forest. The DI water is then replaced with the electroplating solution for the electroplating process. Figure 4.4 shows the vacuum chapter of the infiltration process. Vacuum pump (not shown, Emerson, Motor Division St Louis, MO, USA) was used to pump down the system to 3.1mbar within 9mins.

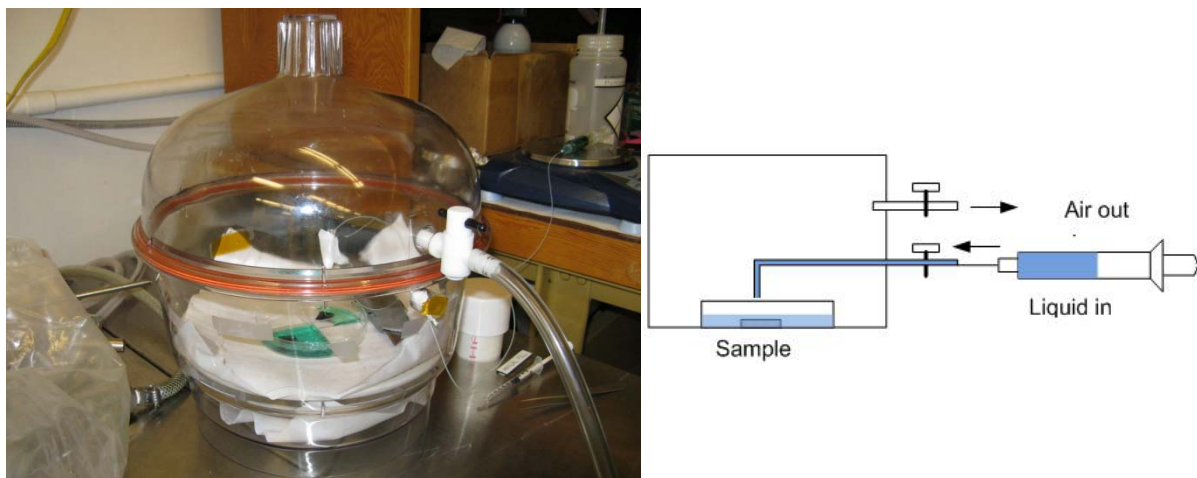


Figure 4.4. Experimental setup of the vacuum infiltration system. The right side is the schematic of the left figure.

A set of pictures recording the vacuum infiltration procedure is shown in figure 4.5. The sample with a size of about 8cm×2cm (figure 4.5(a)) was loaded into the vacuum chamber and covered with DI water and the pictures were taken when:

- (b) One hour after the vacuum pumping down;
- (c) One and a half hour after the vacuum pumping down;
- (d) Immediately after (c) and the only change is that system was vent.

As can be seen, even though half hour passed, there was no big difference between (b) and (c). We can see grey color “air film” on top of the CNT forests, indicating the system has reached a balance and the situation would not change without interference. The “air film” trapped on the CNT surface also indicated that, at the two moments (b) & (c), the CNTs were still not wetted. However, after the system was vented, we immediately notice the surface color of the CNT sample became darker, and the grey-color “air film” was gone. There are two possible ways to explain why the “air layer” disappeared: (1) diminished to negligible volume due to pressure increase according to the well-know equation for gas: $PV = const$; (2) the water in the dish experienced de-gassing during the long vacuum pump down, when the pressure increased, the restored gas solubility might have absorbed the trapped air into the water. In either case, the vacuum difference between inside of CNT and outside (atmosphere pressure) would guarantee the DI water be pushed into the forests. A good thing is that, though the pressure overall is large, from local point view, the pressure difference within water is small (surrounding pressure is the same). It means CNTs would not be harmed under the huge pressure.

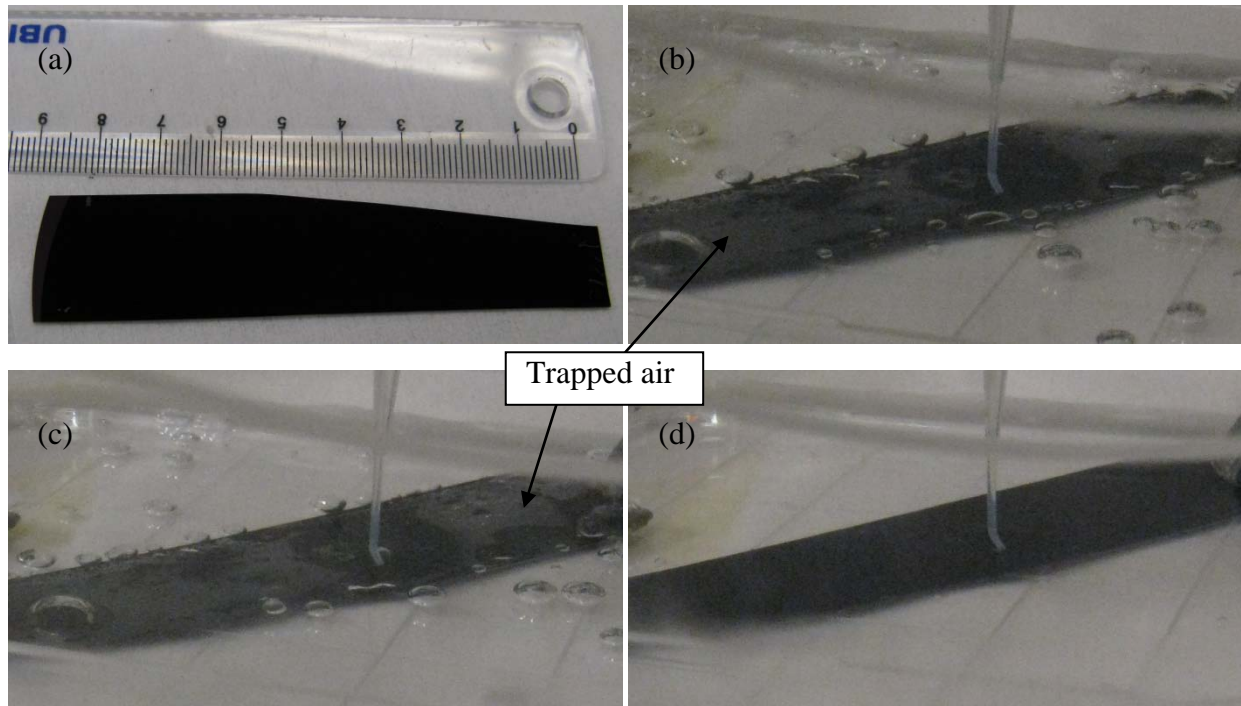


Figure 4.5. A serial of pictures of the CNT vacuum infiltration process. (a) Fabricated sample before loading; (b) 1hr in vacuum; (c) 1.5hr in vacuum; (d) when system was vent immediately after (c) was taken.

One interesting phenomenon is that the vacuum infiltration process is sensitive to the type of covering liquid. Our first trial used the electroplating solution for nickel (Nickel Sulfamate RTU, Product: 030175); however that resulted in precipitations as seen in figure 4.6(a) probably due to the solubility change under vacuum environment. Also cracks were observed on originally continuous CNT film. DI water, as shown in figure 4.6(b), didn't have such issues and was used for all the rest tests.

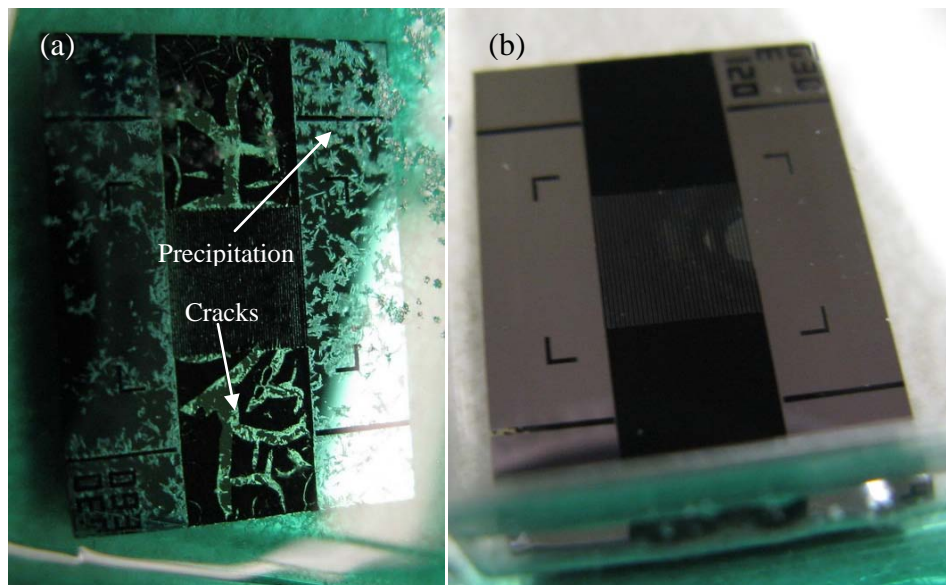


Figure 4.6. Effects of different covering liquids on the vacuum infiltration process. (a) Nickel electroplating. (b) DI-water as the filling liquid. (a) is seen to produce cracks and precipitations that destroy and contaminate the samples.

4.3. Design and fabrication

4.3.1 Full functionalization by electroplating

Nickel Sulfamate RTU (Technic Inc.) was used as electroplating solutions and the standard current density was $40\text{mA}/\text{cm}^2$ and time was between 20 sec to a few minutes. Figure 4.7(a) shows the cross-sectional view from a $150\mu\text{m}$ -height CNT forest structure which has gone through a 4min electroplating process. The top (figure 4.7(b)), middle (figure 4.7(c)) and bottom (figure 4.7(d)) portions of the CNT forest have been decorated with similar size of nickel nanoparticles. Discrete nanoparticles instead of continuous thin film have been deposited probably due to defects on the sidewalls of CNTs [7]. Further tests on EDX (figure 4.8 (a) & (b)) and TEM (figure 4.8 (c)&(d)) provide information on the size of these nanoparticles at about 30nm in diameter, and their chemical compositions.

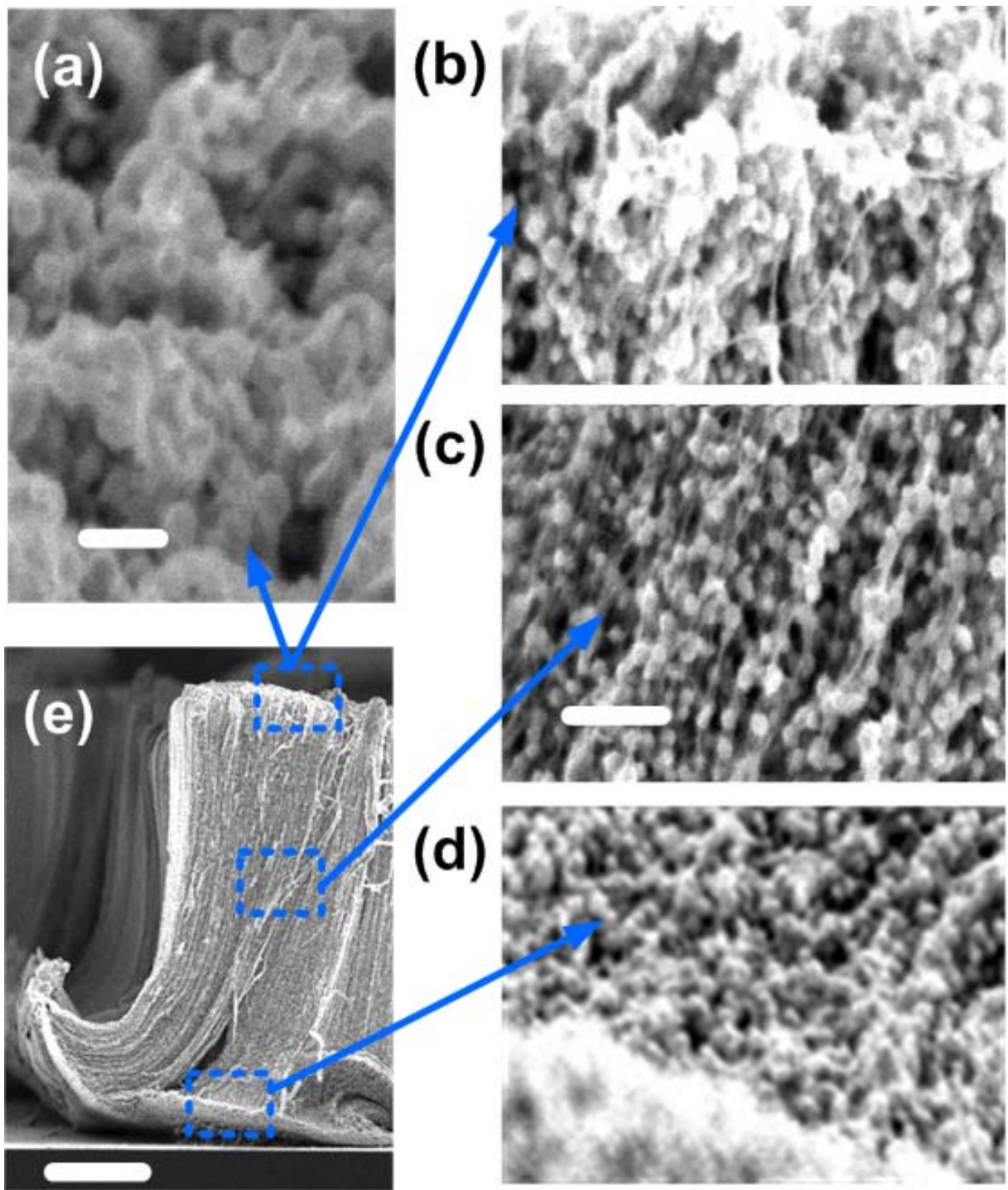


Figure 4.7. 150 μm -long vertically aligned CNTs after the vacuum-assisted electroplating process (4min@ 40 mA/cm², room temperature). (a) Top view, (b)-(d) Cross sectional views of top, middle and bottom regions of CNTs, respectively. These cross sections were obtained by splitting a fresh CNT sample. (e) Far cross sectional view. The scale bars are 200nm for (a), 500nm for (b)-(d), and 20 μm for (e). The height of (e) is less than 150 μm due to volume shrinking during the drying.

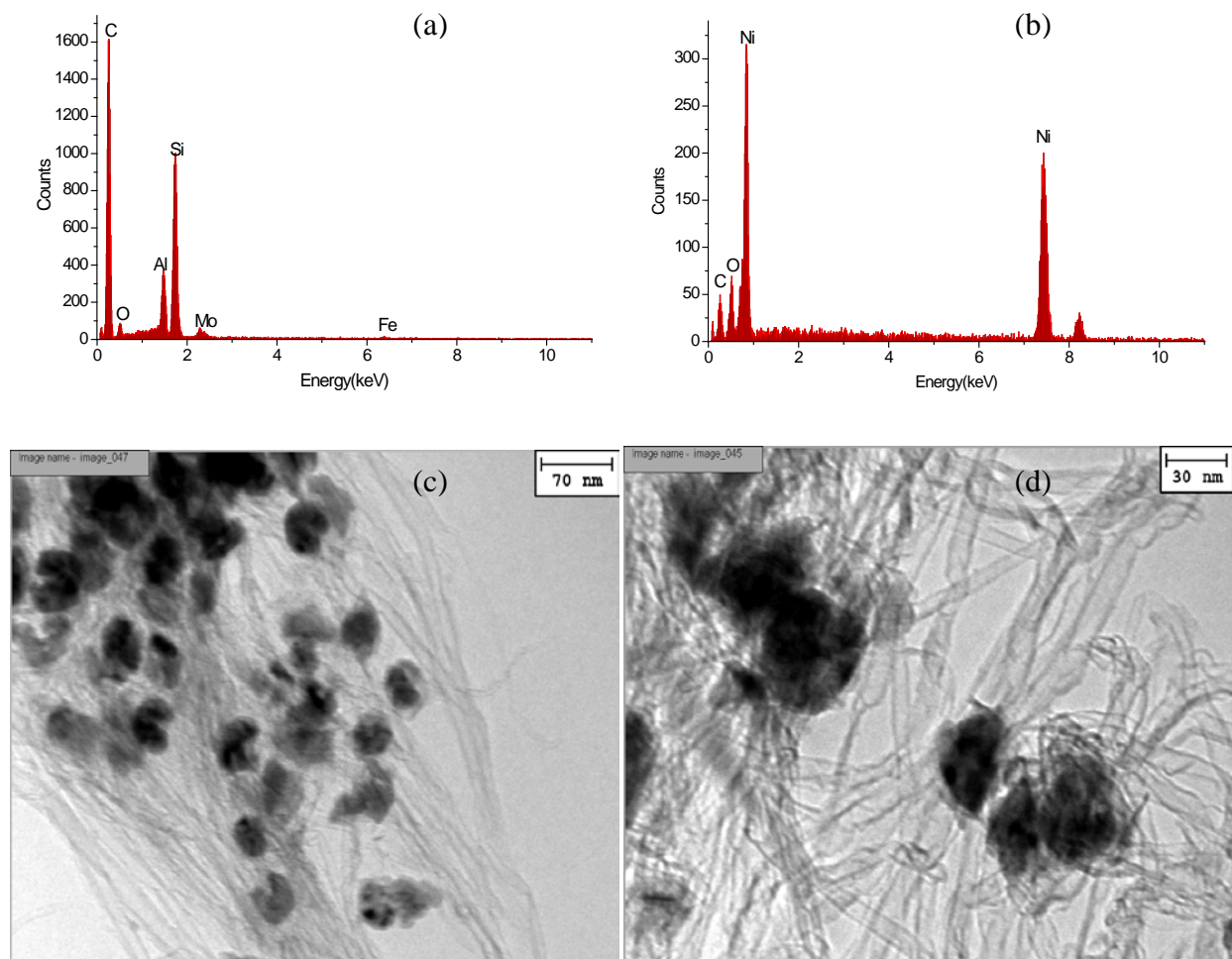


Figure 4.8. EDX results of the CNT forests (a) before and (b) after nickel functionalization. (c) & (d) TEMs of the electroplated CNT samples.

4.3.2 Effects of electroplating parameters

Figures 4.9(a)-(d) show top views of the deposition results under different current densities of 5, 50, 100, and 200 mA/cm² for the same deposition time of 2min. The possible corresponding schematics are illustrated in Figures 4.9(e)-(h), respectively. It is observed that the CNT forests experience impressive morphological change from sparse decorations to solid nanocomposites at the top surface of the CN forests. Furthermore, the size of nanoparticles changes from 30nm to 100nm in diameter when the by electroplating time changes from 10 sec to 3min as shown in Figure 4.10.

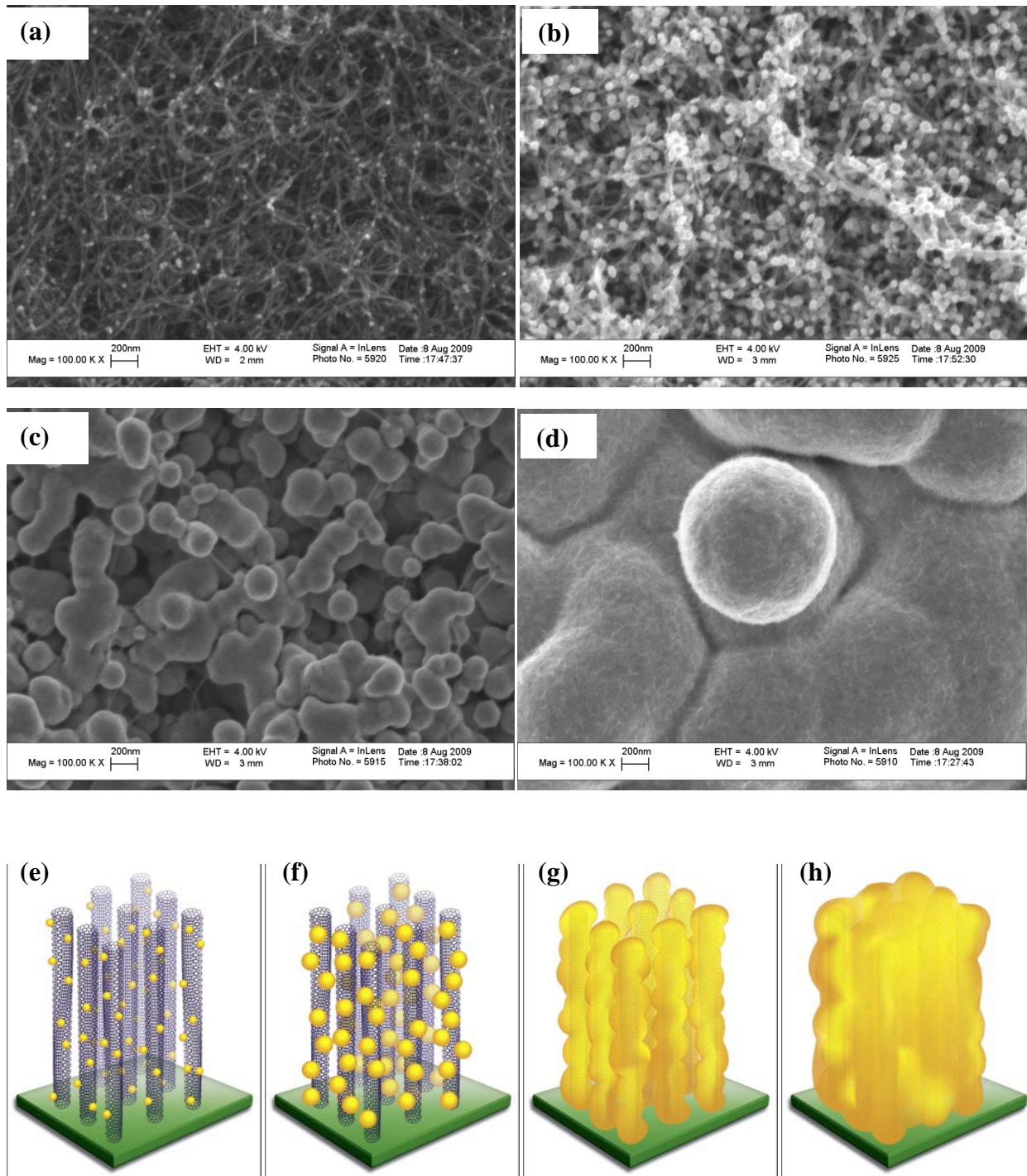


Figure 4.9. Electroplating results using different current density. (a)-(d): Ni nanoparticles deposited with increasing current density of 5, 50, 100, and 200 mA/cm² for the same amount of deposition time of 2mins. (e)-(h) the corresponding structure schematics for (a)-(d), respectively.

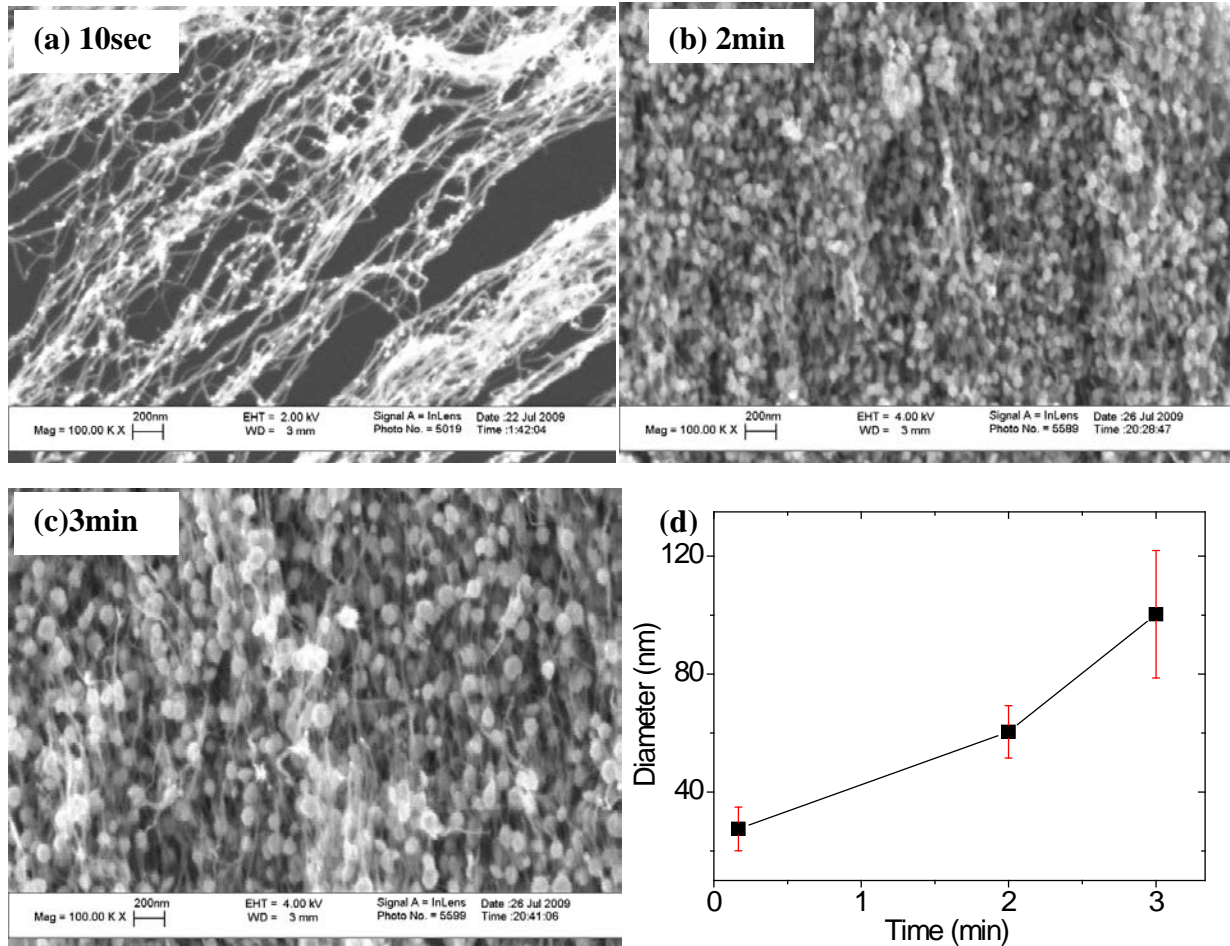


Figure 4.10. Cross section views of nanoparticle size with different deposition time: (a)10sec, (b) 2min, and (c) 3min, respectively. (d) Plot of nanoparticle diameters versus deposition time (estimated based on SEM pictures)

4.3.3 New layout and process flow

When CNT forests are used for either electrical or energy applications, efficient current collection and/or transportation will be vital for the device performances. Previously, CNT forests were grown predominantly on nonconductive substrates [14] and conductive layers had to be added in a later transfer process [15]. As introduced in Chapter 3, CNT forests in this work are synthesized directly on a silicon substrate with a conductive molybdenum metal layer, which provides good CNT growth results and low internal resistance. Meanwhile, aluminum acts as the intermediate buffer layer for the iron catalyst. A measured low sheet resistance of $100\Omega/\text{sq}$ for a $100\mu\text{m}$ -thick CNT forest has been accomplished [16]. A new layout of MEMS supercapacitor was designed as shown in figure 4.11 to accommodate the electroplating process. More details about the new process flow can be found in Appendix B.

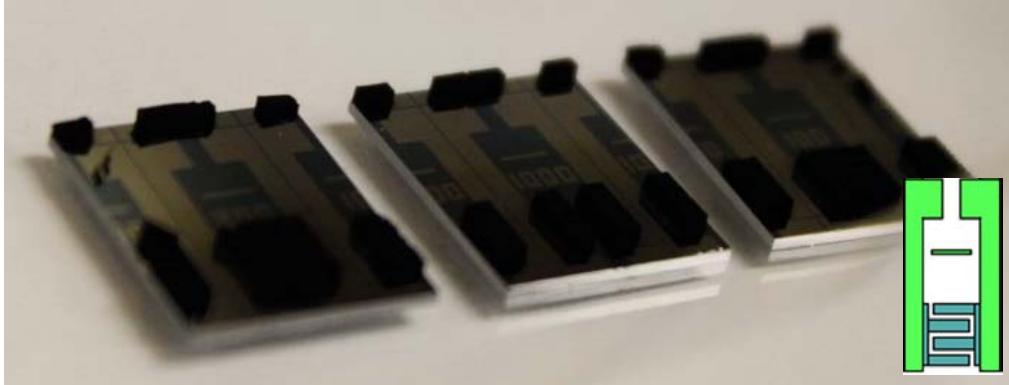


Figure 4.11. Fabricated MEMS supercapacitors using new layout. The inset shows the layout example. During the electroplating process, the area below the horizontal bar would be inserted into the electrolyte solution. The fabricated samples have millimeter-high CNT forests for easy visual observation (actually made with the technique to be discussed in next chapter). However, all experimental data discussed in this chapter, unless otherwise mentioned, were based on about 150 μm -high CNT forest.

4.3.4 Functionalized CNT supercapacitors

CNT forests deposited with nickel nanoparticles have been utilized for supercapacitor electrodes. In the experimental measurements, a simplified half-cell test system is used, composed of a 10mm \times 5mm rectangular-shaped CNT sample, Pt-wire counter electrode, and Ag/AgCl reference electrode as shown in figure 4.12(a). During the test, half (5mm \times 5mm) of the CNT area was inserted into electrolyte and the upper half was used to contact with test equipment (via clamps). The reason that simplified samples instead of the comb-shape electrode patterns were used is simply because of process convenience (no lithography needed) and good yield (one wafer provides hundreds of test samples). However, the results can be easily scaled down to smaller size. All measurements have been carried out on Reference 600TM Potentiostat (figure 4.12(b), Gamry Instruments, Inc., Warminster, PA). The scanning rate of cyclic voltammetry is 100mV/s for all tests unless specified. The results presented here are from the same-batch CNT samples grown with a height of about 150 μm . In this study, the standard recipe (2min , 40mA/cm²) was chosen for all demonstration tests.

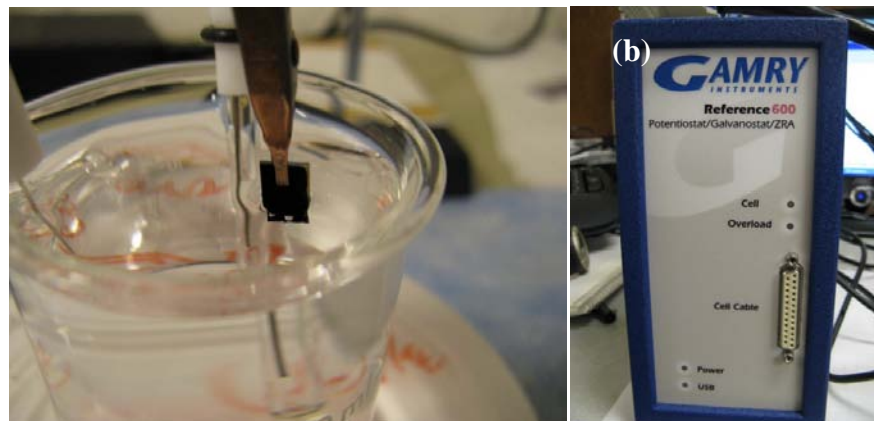


Figure 4.12. Test setup of Ni-electroplated supercapacitors (a) Half-cell, three electrode electrochemical cell setup; (b) electrochemical system, Reference 600 (Gamry Instruments, Inc., Warminster, PA).

4.4 Experimental results

4.4.1 Material oxidation

After the electroplating process, nickel nanoparticles were synthesized within the CNT forests. Since the pseudo capacitor needs nickel hydroxide, a routine method is used [17]: the electrical potential was applied twenty times from -1.2V to +0.8V (high voltage windows than normal tests) to ensure complete formation of the nickel hydroxide. Figure 4.13(a) shows the first five cycles of the oxidation process. As can be seen, an apparent electrical current “valley” (reducing reaction) at -0.1V formed gradually. A high current “peak” (oxidizing reaction) at high voltage (0.8V) can be identified, indicating that nickel has been oxidized at high voltage and reversible redox reaction was happening. At the 4th and 5th cycles, the curves began to show stability. Figure 4.13(b) shows the responses of a CNT supercapacitor without nickel nanoparticles. Initially, a high peak (oxidizing reaction) is also observed possibly due to the oxidation of active carbon such as amorphous carbon on the CNTs. However, the oxidizing reaction did not last long as it was not reversible. The reaction peaks was seen to attenuate over several cycles. Furthermore, there was no formation of the valleys, meaning the reaction is one-way, not reversible. The difference on the magnitude of current gap (between forward and back ward sweeping curves) is another sign showing that there are “additional reactions” happening in the functionalized CNT samples as compared to pristine CNT samples.

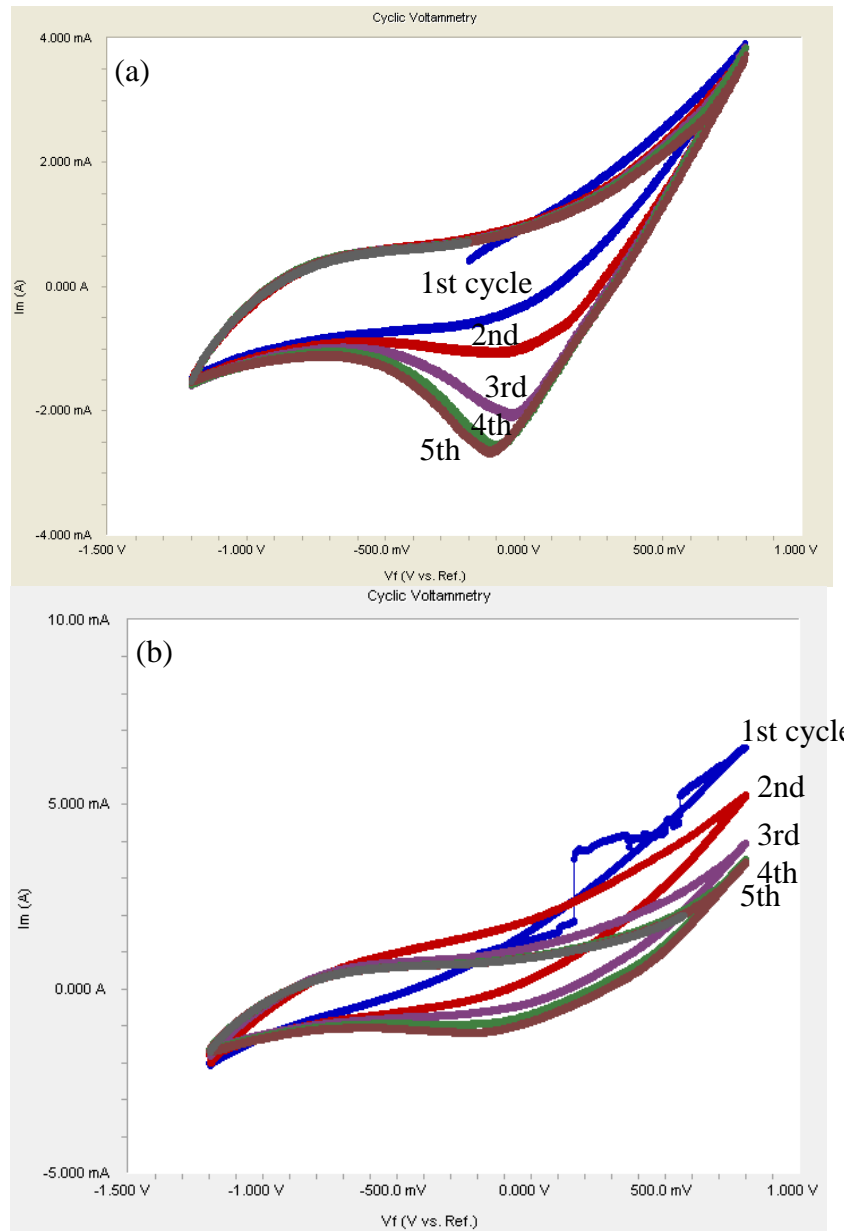


Figure 4.13. (a) Nickel oxidation by cyclic voltammetry and (b) a reference test on CNT sample without nickel. The jerk in 1st cycle of (b) is due to accidental mechanical interference.

4.4.2 Voltage Sensitivity

To confirm the changes of CV curves are indeed the result of nickel hydroxide, we explore the effect of voltage on supercapacitor. For an EDLC, voltage range dose not impact the capacitance ($C=\Delta V/\Delta q$). But for a pseudo capacitor, it may determine whether or not a redox reaction would happen or not. Figure 4.14 shows the CV curves of the functionalized samples at different voltage windows. As can be seen, when the bias voltage was low as shown in figure 4.14(a), Ni^{2+} didn't oxidize into Ni^{3+} such that the CV curve is similar to that of a traditional EDLC capacitor.

When the range of the bias voltage increased from -0.6~0.2V to -1~0.55V in Figure 4.14(b), the absolute magnitudes of the output current peaks and valleys increased. As we recall,

$$C = \frac{dq}{dV} = \frac{dq/dt}{dV/dt} = \frac{I}{dV/dt} \quad (4-2)$$

As dV/dt is 50mV/sec for all the tests, a higher current magnitude means a higher capacitance. With both direction considered, we define the current gap between forward and backward curve, $\Delta I = I_{\text{forward}} - I_{\text{backward}}$. It is clear that a higher ΔI means a higher capacitance. When the range of the biased voltage increased further as shown in figure 4.14(c) to -1.2 ~ 0.8V, more nickel hydroxide was involved in the reaction such that peaks and valleys on the CV curves were more visible. These changes imply that both the nickel hydroxide reducing and oxidizing reactions have involved in the operation of supercapacitors. The trends of (a)-(c) show that the peak and valleys are indeed the results of nickel hydroxide and they need a wide enough voltage windows to be active. In term of capacitance increase, figure 4.14(d) compared the ΔI , which is in proportion to the capacitance. As can be seen, (c) has a three times larger ΔI , meaning the nickel hydroxide increased the capacitance by two times.

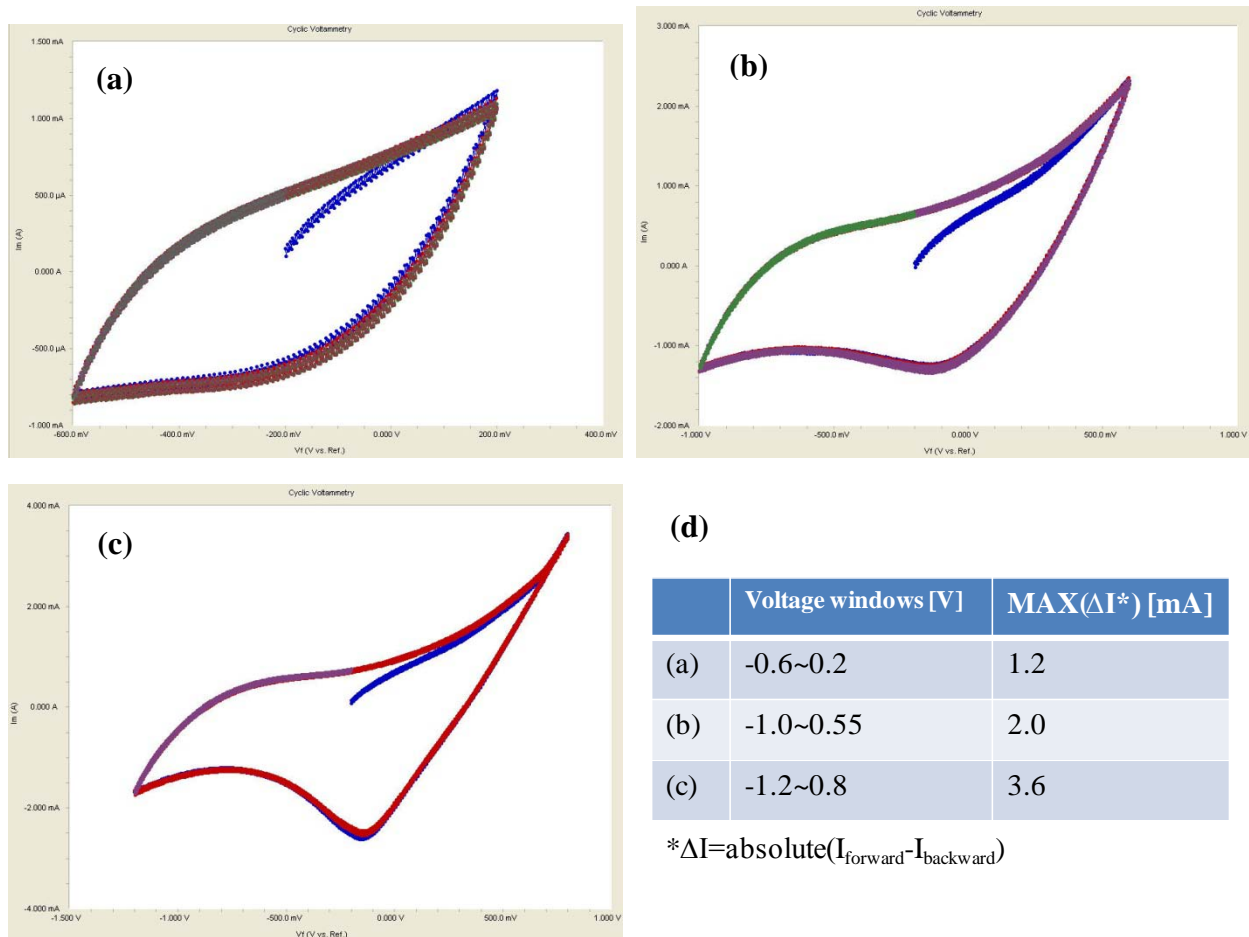


Figure 4.14. CV curves for different tests on the same sample with gradually increased applied voltage ranges from -0.6~0.2, -1~0.55, -1.2~0.8V. for (a), (b) and (c), respectively. (d) Summary of applied voltage range and maximum current differences of the forward and backward curves.

4.4.3 Cyclic voltammetry curves

Figure 4.15(a) shows the cyclic voltammetry tests of a prototype CNT supercapacitor with embedded nickel nanoparticles. The size of the sample is $5 \times 5 \text{ mm}^2$ with CNT forest of about $150 \mu\text{m}$ in thickness and embedded nickel nanoparticles of about 60 nm in diameter. The scanning rate was 100 mV/sec and electrolyte was 0.1 M KOH aqueous solution. It is observed that the addition of nickel nanoparticles (blue line) results in distorted shape with clear low valley configuration around zero bias voltage, indicating redox reactions. The testing results from CNT supercapacitor without the nickel nanoparticles (red line) show a more traditional profile closer to a rectangular shape. The pseudo-capacitor with nickel nanoparticles has much better energy storage performance as shown. At the bias voltage of 0 V , the capacitance of the supercapacitor with nickel nanoparticles (calculated as the distance between forward and backward sweeps) is increased by nearly one order of magnitude higher than the supercapacitor without nickel nanoparticles. Also shown in (a) is the CV curve of a Ni foil (green color). Because Ni foil has limited surface area compared to CNT, the CV is far less. But, as there are nickel hydroxide on its surface, it is still a simple pseudocapacitor and its CV curve is better than a plain metal surface, which, as previously shown in Chapter 3, be diminished into a "straight line". Figure 4.15(b) shows the CV test results of 100 charge/discharge tests. Good stability was confirmed as there was no apparent current magnitude change. Figure 4.15(c) shows CV test results from the first and last five cycles with a good match, clearly proving that there was little performance fluctuation due to the existence of Ni nanoparticles during the long-term tests.

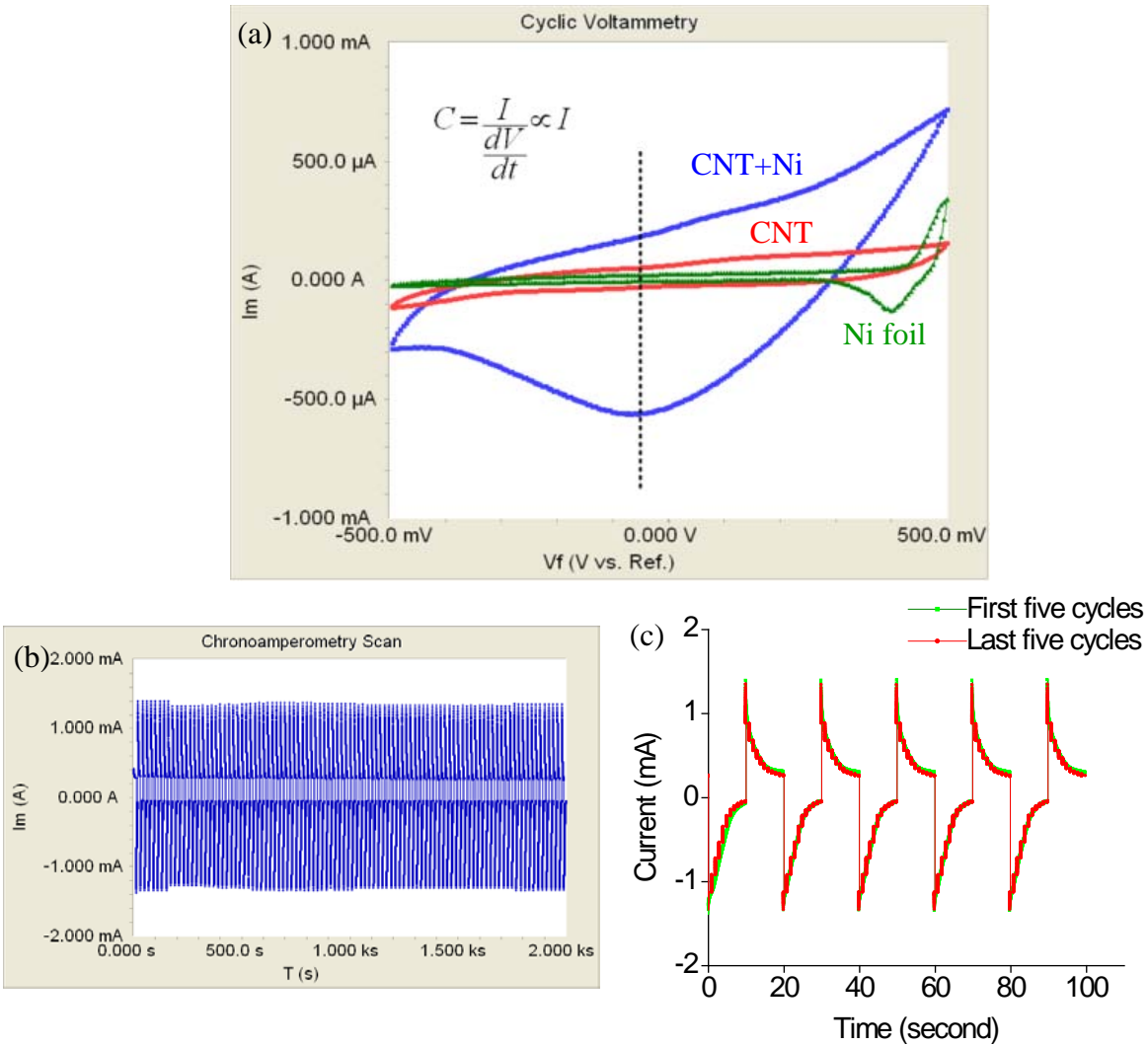


Figure 4.15. Performance of a prototype CNT supercapacitor with embedded nickel nanoparticles. (a) Cyclic voltammety curves with “CNT+Ni” (blue), CNT (red), and Ni foil (green) electrodes. Scanning rate was 100mV/sec and electrolyte was 0.1M KOH. (b) CV results showing 100 cycles of charge and discharge curves. (c) Charge/discharge curves for the first and last five cycles from (b).

4.5. Discussions

Some approximations have been made to roughly calculate the total capacitance from the sample in figure 4.15(a). First, the CV curve has been approximated as a triangle shape as shown in figure 4.16. The maximum distance between forward and backward scanning curve is about $800\mu\text{A}$. The minimum is apparently $0\mu\text{A}$ at the two ends. Therefore, the average current distance is approximated as $400\mu\text{A}$. Because the $400\mu\text{A}$ value is composed of both forward and backward directions, the current value can be estimated as $200\mu\text{A}$.

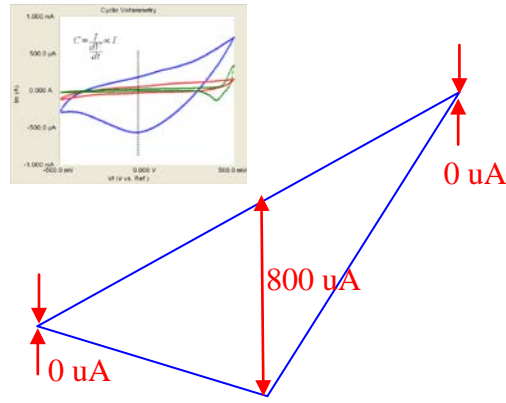


Figure 4.16. Rough estimation of the CV curve for capacitance calculation. The inset is figure 4.15(a) as a reference.

Since the scanning rate was 100mV/s, the total capacitance is calculated as:

$$C_{total} = \frac{I}{\frac{dV}{dt}} = \frac{200\mu A}{0.1V/s} = 2mF \quad (4-3)$$

The volumetric specific capacitance is calculated by accounting the volume of the CNT forest electrode. The prototype CNT samples have an area of $5 \times 5 \text{mm}^2$ in the KOH solution and the CNT thickness is $150\mu\text{m}$. Therefore,

$$V_{CNT} = 0.5\text{cm} \times 0.5\text{cm} \times 150 \times 10^{-4}\text{cm} = 3.75 \times 10^{-3}\text{cm}^3 \quad (4-4)$$

Since only half of the supercapacitor was measured in this work, the full supercapacitor should have the other same chip in operation and the total capacitance should be twice the capacitance from the measured single electrode results. Therefore, the volumetric specific capacitance for a whole capacitor is calculated as:

$$C_{sp} = \frac{2C_{total}}{V_{CNT}} = \frac{2 \times 2mF}{3.75 \times 10^{-3}\text{cm}^3} = 1.06F/\text{cm}^3 \quad (4-5)$$

4.5.1 Reliability

Cyclic tests have been conducted up to 1000 cycles, which last more than half a day. Figures 4.17 (a) and (b) show SEM pictures of cross sectional views of the CNT supercapacitor before and after the long cycling tests. It is observed that the morphology of these nanoparticles did not change before and after these tests.

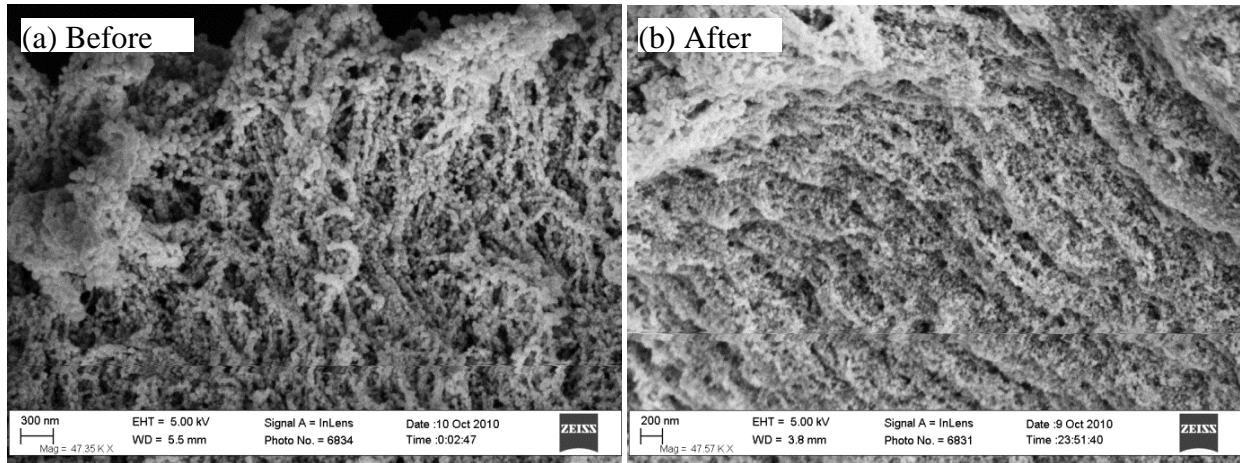


Figure 4.17. SEM of CNT forest with embedded nickel nanoparticles (a) before and (b) after 1000 cycles of CV tests.

4.5.2 Preservation of structural shape

It is well-known that CNT forests shrink and densify themselves during the air-drying process due to large surface tension force [18]. Figure 4.18 shows that CNT forests with embedded nickel nanoparticles could retain its original structural shape after the drying process without shrinkage. Obviously, the addition of nickel nanoparticles has strengthened the CNT forest structure.

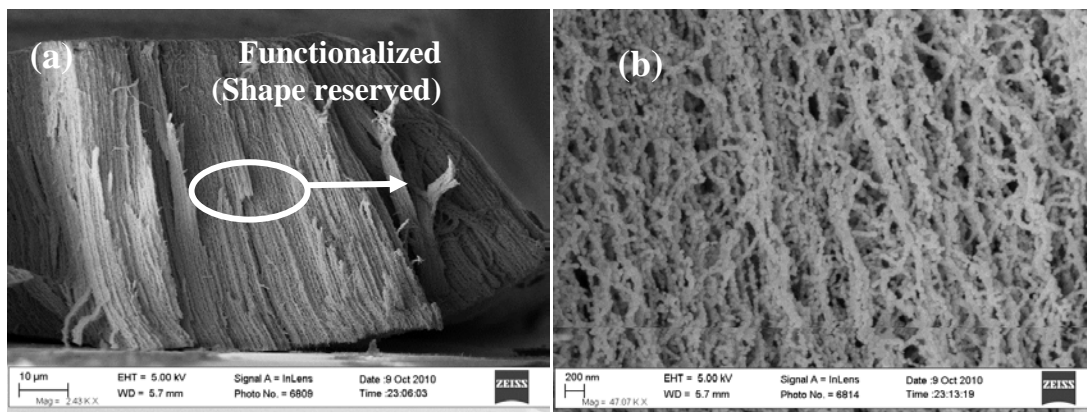


Figure 4.18. (a) Dried CNT forest with embedded nickel nanoparticles. (b) Close view SEM photo of the nickel nanoparticles embedded within the CNT forest with high porosity.

4.5.3 Other nanoparticles

The vacuum infiltration method used in this chapter is a general approach and can be applied to other materials. Here, zinc is used as one demonstration example in addition to nickel. The electroplating solution (8 oz Plug N' Plate® Zinc Solution, Caswell Inc.) was purchased. The results in Figures 4.19 show several interesting effects. First, rice-shaped zinc clusters have been found on top of the CNT forest as shown in figures 4.19 (a) & (b) and irregular zinc pieces have been deposited inside the CNT forest as shown in figure 4.19(c). It is believed that this approach of electroplating process can be applied to various nanomaterials. The functionalization process

would fundamentally change the mechanical, electrical, physical and chemical properties of the original CNT forests for different applications, such as multiplexing gas sensor arrays, catalyst loading, and synthesis of nanoparticles. Particularly, by uniformly coating CNT forests with nanomaterials on top of silicon substrates, the combination of CNT/nanoparticles may open up new possibilities in microelectronics and MEMS applications.

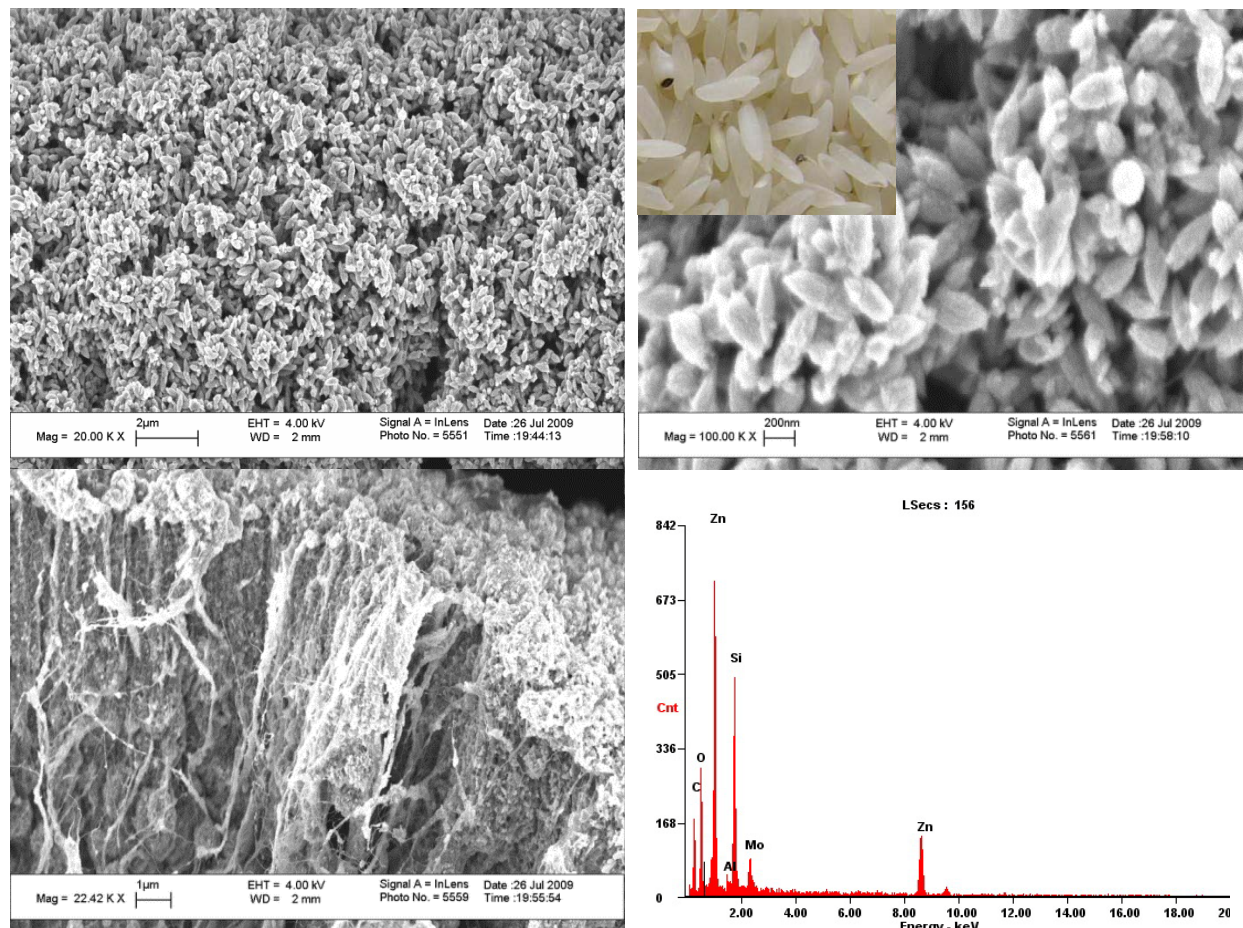


Figure 4.19. Zinc-coated CNT forests using vacuum infiltration and electroplating ($40\text{mA}/\text{cm}^2$, 2min). (a) top view; (b) close view of (a) with an inset of rice; (c) cross sectional view; (d) EDX result of Zinc-plated CNT forests.

References

- [1] B. E. Conway, *Electrochemical Supercapacitors: Scientific Fundamentals and Technological Applications*, Kluwer Academic/Plenum Publishers, New York, 1999.
- [2] B. E. Conway, V. Birss, and J. Wojtowicz, The role and utilization of pseudocapacitance for energy storage by supercapacitors, *J. Power Sources*, 1997, 66, pp.1
- [3] Patrice Simon and Yury Gogotsi, Materials for electrochemical capacitors, *Nature Materials*, 2008, 7, pp.845
- [4] K.-W. Nam et al., "X-ray absorption spectroscopy studies of nickel oxide thin film electrodes for supercapacitors", *Electrochim Acta*, 2002, 47, pp.3201

- [5] Mao-Sung Wu, Chen-Yu Huang, Kun-Hao Lin, Electrophoretic deposition of nickel oxide electrode for high-rate electrochemical capacitors, *Journal of Power Sources*, 2009, 186, pp.557
- [6] U.M. Patil, K.V. Gurav, V.J. Fulari, C.D. Lokhande, Oh Shim Joo, Characterization of honeycomb-like " β -Ni(OH)₂" thin films synthesized by chemical bath deposition method and their supercapacitor application, *Journal of Power Sources*, 2009, 188, pp.338
- [7] Y. Fan, B.R. Goldsmith, and P.G. Collins, "Identifying and counting point defects in carbon nanotubes", *Nat. Mater.*, 2005, 4, pp.906
- [8] T. M. Day et al., "Electrochemical Templating of Metal Nanoparticles and Nanowires on Single-Walled Carbon Nanotube Networks", *J. Am. Chem. Soc.*, 2005, 127, pp.10639
- [9] S. -B. Ma et al., "Synthesis and characterization of manganese dioxide spontaneously coated on carbon nanotubes", *Carbon*, 2007, 45, pp.375
- [10] W.-C. Fang et al, "Arrayed CN_x NT–RuO₂ nanocomposites directly grown on Ti-buffered Si substrate for supercapacitor applications", *Electrochem Commun*, 2007, 9, pp.239
- [11] A. Chandrashekar, S. Ramachandran, G. Pollack, J.-S. Lee, G.S. Lee, L. Overzet, Forming carbon nanotube composites by directly coating forests with inorganic materials using low pressure chemical vapor deposition, *Thin Solid Films*, 2008, 517, pp.525
- [12] W. Fang, H.-Y. Chu, W.-K. Hsu, T.-W. Cheng, and N.-H. Tai, "Polymerreinforced, aligned multiwalled carbon nanotube composites for microelectromechanical systems applications," *Adv. Mater.*, 2005, 17(24), pp.2987
- [13] Kenneth K. S. Lau, Jose Bico, Kenneth B. K. Teo, Manish Chhowalla, Gehan A. J. Amaratunga, William I. Milne, Gareth H. McKinley, and Karen K. Gleason, Superhydrophobic Carbon Nanotube Forests, *Nano Letters*, 2003, 3(12), pp.1701
- [14] S. Talapatra, S. Kar, S.K. Pal, R. Vajtai, L. Ci, P. Victor, M.M. Shaijumon, S. Kaur, O. Nalamasu and P.M. Ajayan, Direct growth of aligned carbon nanotubes on bulk metals, *Nature nanotechnology*, 2006, 1, pp.112
- [15] V.L. Pushparaj, M.M. Shaijumon, A. Kumar, S. Murugesan, L.J. Ci, R. Vajtai, R.J. Linhardt, O. Nalamasu, and P.M. Ajayan, Flexible energy storage devices based on nanocomposite paper, *PNAS*, 2007, 104, pp.13574
- [16] Yingqi Jiang, Pengbo Wang, and Liwie Lin, Characterizations of Contact and Sheet Resistances of Vertically Aligned Carbon Nanotube Forest with Intrinsic Bottom Contacts, *Nanotechnology*, 2011, 21, pp.365704
- [17] R.P. Deo, N.S. Lawrence, and J. Wang, Electrochemical detection of amino acids at carbon nanotube and nickel–carbon nanotube modified electrodes, *Analyst*, 2004, 129, pp.1076
- [18] D. N. Futaba, K. Hata, T. Yamada, T. Hiraoka, Y. Hayamizu, Y. Kakudate, O. Taniike, H. Hatori, Mo. Yumura, and S. Iijima, Shape-engineerable and highly densely packed single-walled carbon nanotubes and their application as super-capacitor electrodes, *Nature Materials*, 2006, 5, pp. 987

Chapter 5 Ultra long and densified CNT forests electrodes

Two ways to further improve the energy density of the supercapacitors are introduced in this chapter. The first one employs ultra-long CNT forests as the electrodes for supercapacitors. By using a water-assisted CVD method, 300 μm -long CNT electrodes have been manufactured and tested. Long CNT forests electrodes increase the total surface area and consequently enhance the device capacitance. The second approach utilized the air-drying, CNT densification process to reduce the volume of CNT electrodes. Preliminary experimental results have shown the height of CNT forests can be reduced to 1/16 of the original thickness. CV measurements show similar performance before and after the densification process. As such, the capacitance density for densified CNT electrodes is about 16 times higher than those CNT electrodes without going through the densification process.

5.1 Ultra-long CNT forests

5.1.1 Motivations

In order to further increase the capacitance of the CNT-forest supercapacitors, the fundamental capacitance equation is re-examined [1]:

$$C = \frac{\epsilon_0 \epsilon_r A}{d} \quad (5-1)$$

If the electrolyte is selected and electrode double layer is used as the basic operation principle, surface area is the last element to enhance the capacitance. One way to increase the surface area is to get longer CNTs. In chapter 2, a $\text{C}_2\text{H}_2 + \text{H}_2$ CVD deposition was used to synthesize CNT forests up to 80 μm in a 10-min deposition time. However, there are several issues:

(1) CNT Height

Numerous experimental trials show the height of CNT forests reaches a cap of about 100 μm and stop to grow further afterwards. This scene is also observed from other groups [2] and the reason is believed to be related to the lost activity of the catalyst [3]. Amorphous carbon, a by-product of the CVD process, could gradually cover the catalyst nanoparticles and block the catalyst nanoparticles from accessing external carbon precursor gas to stop CNT growth.

(2) Impurities

CNTs synthesized from CVD methods often contain impurities that may come from catalyst nanoparticles (e.g. Fe), supporting materials (e.g., Al, Si, etc.), amorphous carbon or other carbon by-products. These impurities are chemically active materials and could impact the performance of supercapacitors. For example, figure 4.13(b) in previous chapter has shown evidences of oxidizing peaks in the CV curves under high sweeping voltage. These peaks are the

results of impurities. Current solution is to conduct post-growth purification [4], which, however, often damages CNTs because of chemicals and manipulation.

Iijima's group has demonstrate the methodology to grow ultra-long CNTs in 2004 [3] by adding a controlled amount of water vapor into the carbon precursor. Water (essentially H⁺ ions at high temperature) acts as a weak oxidant during the CNT growth process to selectively remove amorphous carbon without damaging CNTs.

5.1.2 Experimental setup

A water-assisted CNT growth system has been constructed and tested. Essentially, one extra gas input line is added to the original system as shown in figure 5.1 and the growth recipe is listed in Table 5.1. Figure 5.2 illustrates fabricated samples.

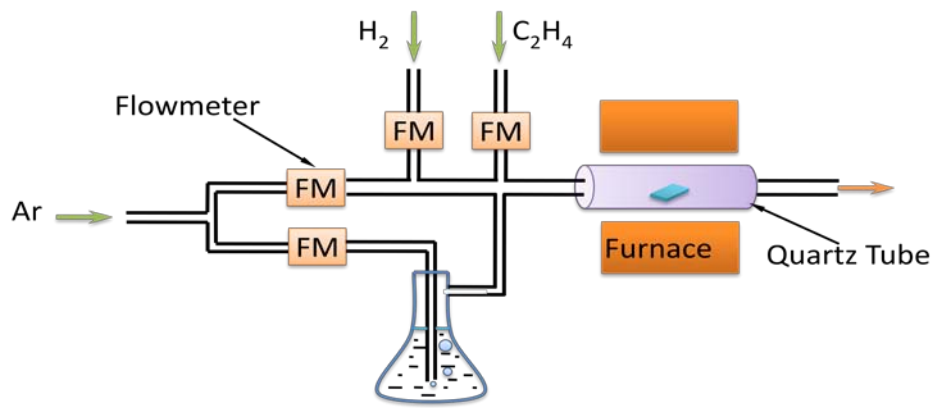


Figure 5.1. Schematic of experimental setup for the synthesis of ultra-long CNTs. A small amount of argon flows through a water-filled bottle to provide water vapor into the synthesis tube.

Table 5.1. Standard protocol for water-assisted ultra long CNT growth*

| |
|---|
| 1. Thermal oxidization of silicon wafer with 1000-2000Å oxide. |
| 2. Deposition of molybdenum (if a conductive substrate is needed), aluminum and iron in sequence with thicknesses of 50nm (or higher), 10nm, and 5nm, respectively, using e-beam evaporation. |
| 3. Placement of samples into a 2-inch quart tube. The tube is vacuumed and then filled with 99.9% hydrogen. Then the temperature is raised to 750°C . During the heating process, Ar and H₂ flow through the tube with a velocity of 440 and 176 sccm , respectively. |
| 4. The carbon precursor gases of C ₂ H ₄ (with Ar and H ₂ maintaining the same flow rates in #3) and a small amount of Ar are added into the system with a velocity of 100 and 15sccm , respectively. A 10-min growth results in a CNT height of 300µm (with Mo layer) or about 1mm (without Mo layer) . So far the highest height is about 3mm by growing CNTS for 30mins. |
| 5. The tube is pulled out of the furnace and cooled down with a fan to room temperature. |
| 6. The system is purged with Ar and the tube is opened to unload the samples. |

* Those differences from the original recipe in chapter 2 (table 2.1) are highlighted with bold and underline marks.

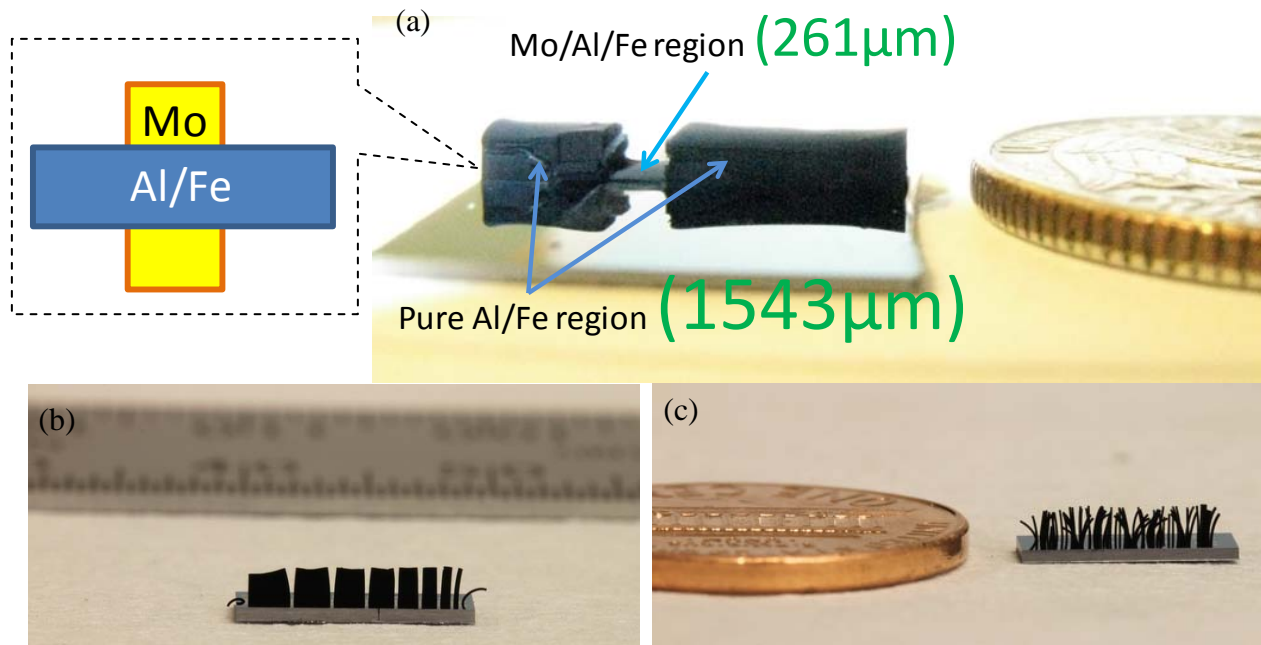


Figure 5.2. Synthesis of ultra-long CNTs. (a) Bulk growth of ultra-long CNTs. The CNT height measured under SEM is $261\mu\text{m}$ and $1543\mu\text{m}$ for the two Mo/Al/Fe and Al/Fe regions, respectively. The inset shows the schematic layout of the sample. (b) CNT “thin walls”; (c) CNT “hairs” (micropillar array). All the samples were grown for 30min to guarantee over 1mm in height.

5.1.3 Process discussions

There are several issues observed during our process developments. Firstly, after several runs, yellow junks can be found around the outlet area of the furnace tube and the junks are likely the carbon and water mixtures. Lowering the flow rate of argon gas that carries water vapor does not solve the problem. It is found that these yellow junks can be cleaned by opening the two ends of the tube and heating it to the temperature of 900°C . It is observed the yellow junks completely disappear.

Furthermore, it is found that Mo layer would significantly impact the CNT growth as shown in figure 5.2 (a). One possible explanation is the catalytic reactions. Experimental results show that freshly-made CNT samples tend to have drastic height differences. For example, if a sample is sitting in air environment for several days, the synthesis results show more uniform CNT thickness as shown in Figure 5.3. In this case, the CNT height is about $1\mu\text{m}$ throughout the areas with or without Mo layer.

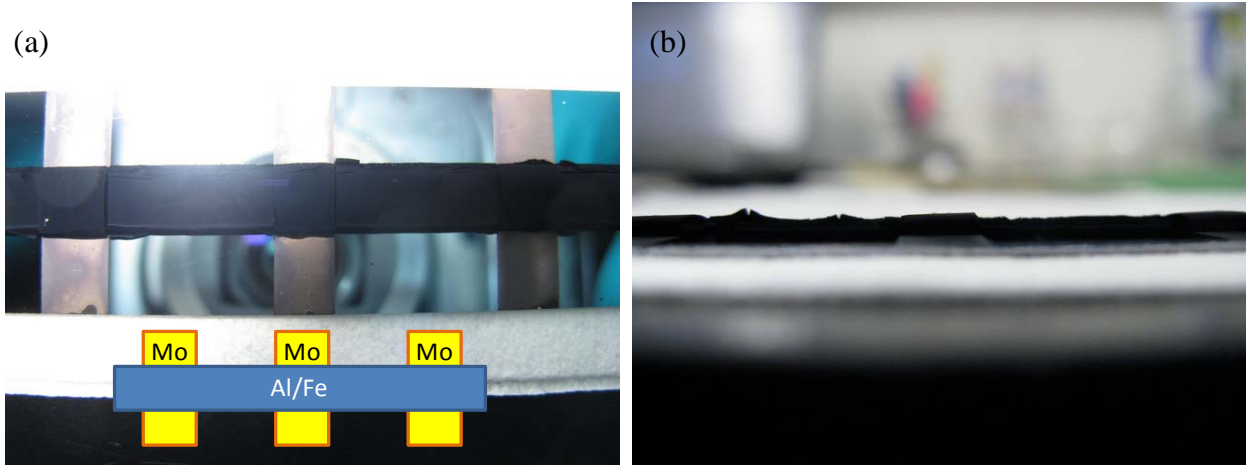


Figure 5.3. More uniform growth of ultra-long CNTs with and without Mo layer on aged sample. (a) top view. The inset is the schematic diagram of the metal patterns; (b) side view.

5.1.4 Supercapacitor application

Figure 5.4 shows the CV measurements of CNT supercapacitor made of ultra long CNT forests. It is observed the magnitude of current (capacitance) increased about 4 times as compared with the sample with short CNT forest electrode, matching well with the height increment (from $80\mu\text{m}$ to $300\mu\text{m}$). Figure 5.5 shows more than 100 cycles of CV measurement results with good stability. The small shifts at the beginning (-0.7V) and end (0.3V) of the CV curves are probably due to the oxidation reactions from impurities.

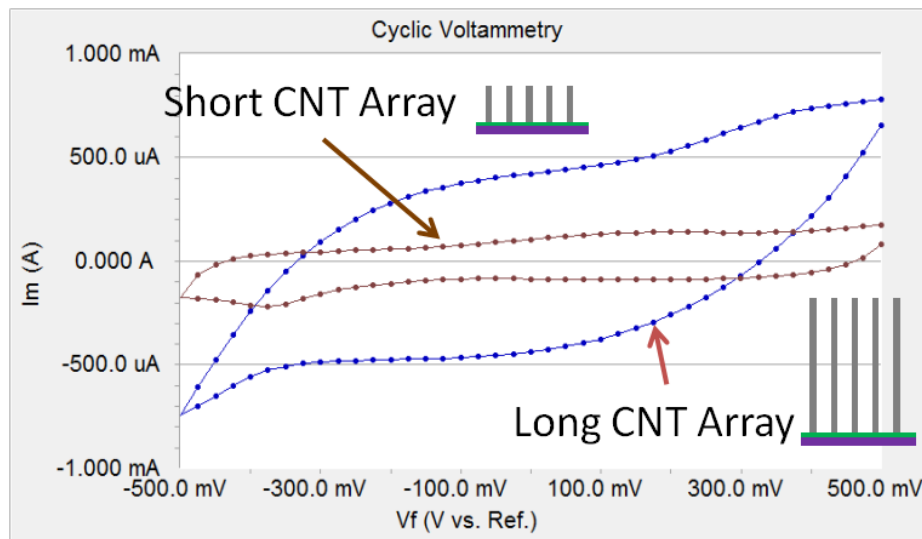


Figure 5.4. CNT supercapacitors with short CNT forest ($\sim 80\mu\text{m}$, brown color) and long CNT forest ($\sim 300\mu\text{m}$). The electrolyte is 0.1M KOH solution and scanning rate is 50mV/s .

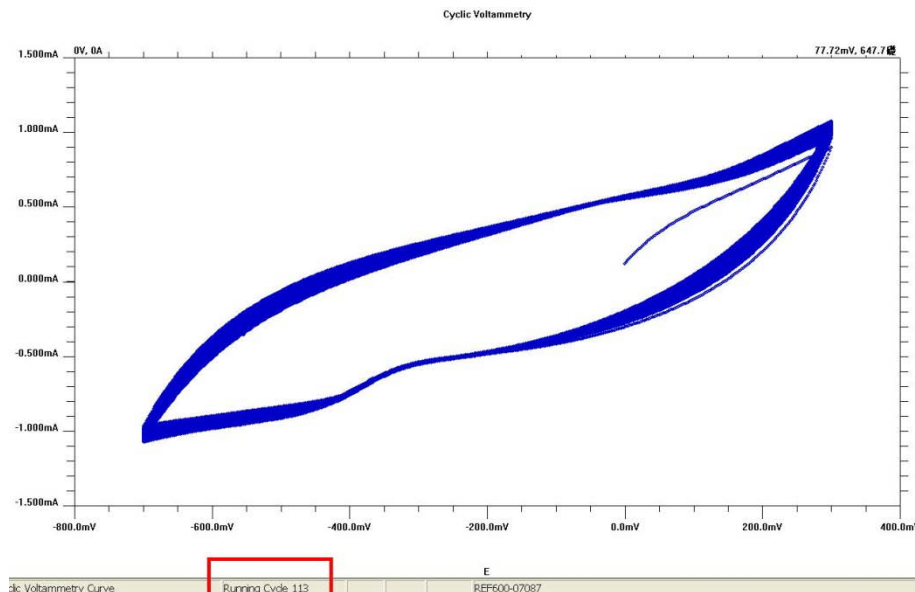


Figure 5.5. Long term (113 cycles) of cyclic voltammetry measurements with minor changes.

5.2 In-situ densification of CNT forest at large area

From the point of energy density, electrodes are characterized by volumetric specific capacitance that is defined as the total capacitance normalized by the volume of the electrodes. The efforts to reduce the volume while maintaining the total capacitance to enhance the magnitude of specific capacitance are discussed in this section.

5.2.1 Motivations

CNT forests have high porosity up to 99.6% [5] and the density of CNT forests could be as small as $0.01\text{-}0.02\text{g/cm}^3$ [6] which is much smaller than graphite, a common material in energy storage applications, with density at $2.09\text{-}2.23\text{ g/cm}^3$ [7]. High porosity is attractive for applications such as CNT-based sensors but it might not be desirable for applications in supercapacitors. Specifically, there are three types of pore sizes within a supercapacitor electrode: macropores ($>50\text{nm}$), mesopores ($50\text{nm}\sim 2\text{nm}$), and micropores ($<2\text{nm}$) [8]. In general, electrolytic ions have typical size of several nanometers. Spaces between micropores structures are too small for electrolytic ions to move in and out of the pores. On the other hand, the spaces between macropores structures are too big, resulting in poor volume utilization efficiency. As a result, mesopores-size is the best choice among the three sizes for supercapacitor applications. The as-grown CNT forests are very sparse with typical spaces around 100nm so they can be characterized as macropores structures. It would be desirable if the pore size of CNT forests can be further reduced to the mesopores range for possible better performances in supercapacitor applications.

Researchers have proposed different CNT structures to achieve porous yet high density systems. For example, M. Lu *et al.* used a dielectrophoresis process to realize the self-assembly of CNT film [9]. Oriented, compact, single-walled CNT films of $15\text{-}20\text{nm}$ thick were assembled after multiple processing steps. Iijima's group proposed a liquid densification method using the

zipping effect of liquids to condense porously-assembled CNTs during the evaporation process [10]. By dipping single-walled CNT forest samples into liquid and then left air dry, the interval space of CNTs decreased from 16nm to 3.7nm. Y. Hayamizu *et al.* used a similar principle and a hierarchical assembly scheme to guide thin CNT forest walls onto silicon wafers [11]. The densified CNT films were structured into discrete islands as “processable carbon nanotube wafers”. D. Wang *et al.* used the so-called "domino pushing" process to mechanically push down the CNT forest [12] to form an aligned bucky paper.

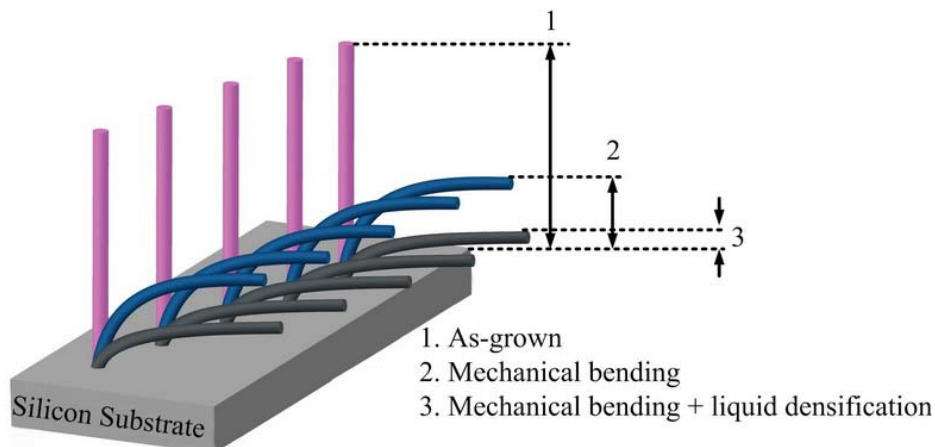


Figure 5.6. Schematic of the two-stage, self-aligned vertical densification process for as grown CNT forests. The as-grown CNT forest on top of silicon substrate is mechanically deformed downward from position “1” to “2” in the figure and further compressed by liquid densification from position “2” to “3” as shown.

In this section, a two-stage, self-aligned vertical densification process is demonstrated for as-grown CNT forests on silicon substrate for enhanced energy density in supercapacitor applications. It has the advantages [13] in contrast to the previous densification process [10] as: (1) no holding covers in the densification process, (2) self-aligned vertical densification, and (3) no breakage of original CNT contacts to the substrate. Specifically, the densification process is accomplished by two key steps as shown in figure 5.6. In the first step, the CNT film is gently bent by a mechanical force to the position marked as “2” in the figure using a plastic roller. The purpose of this step is to generate a downward movement of the CNTs. In the second step, the structure (without the plastic roller) is dipped into liquid and air dried. The surface tension force of the liquid is utilized to further condense the CNTs vertically into a dense solid film as marked “3” in the figure. The initial deformation of the CNT forest as result of the mechanical force in step 1 helps the surface tension force in step 2 to shrink CNTs in the vertical direction. Material characterizations of the densified film are reported in this section. Furthermore, the densified CNT forests on silicon substrate were demonstrated as the electrodes for supercapacitor applications.

5.2.2 Densification process

The CNT samples were grown by a thermal CVD method as presented in chapter 2 for about 10 minutes on top of oxidized silicon chips with a standard size of 10mm×5mm. This resulted in a thick CNT film with vertically aligned CNTs of about 320μm in height. It is noted that oxidized silicon was chosen here to achieve a thicker CNT forest. If a conductive substrate is desirable,

the direct growth process of CNT forests on conductive substrate has been demonstrated previously [14]. Afterwards, the liquid densification process was conducted to reduce the porosity of the CNT forest to achieve possible higher energy density in supercapacitor applications. In general, figure 5.7(a) illustrates the effect of surface tension force on CNTs during the drying process to contract CNTs in the lateral direction [10]. If the liquid densification process was conducted without the first step of mechanical deformation as the guidance, CNTs could randomly agglomerate and condense in the lateral direction as shown in figure 5.7(a). In the two-stage densification process in figure 5.7(b), the CNT forest was deformed in one direction initially as illustrated. The liquid densification process in the second stage was used to further condense the CNT forest in the vertical direction while keeping the original aligned CNT pattern in the new lateral direction as shown. In this process, CNT could form a thick, uniform film. Figure 5.7(c) and (d) are optical photos showing results after the liquid densification processes without and with the first-step mechanical bending process, respectively. Results clearly indicate that the proposed two-stage, self-aligned vertical densification process can produce continuous films in figure 5.7(d) without the random distribution of blocks of CNTs in figure 5.7(c).

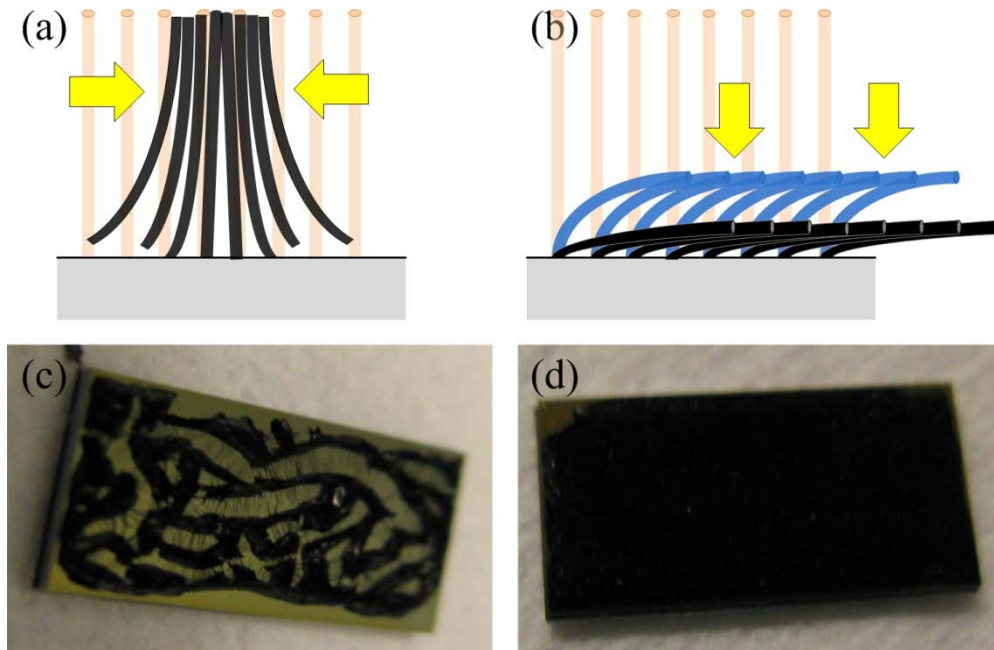


Figure 5.7. Schematic diagrams showing the liquid densification phenomena for (a) without and (b) with the proposed two-stage, self-aligned vertical densification process for CNT forest, respectively. Arrows in the figures are the contract directions of CNTs during the liquid densification process. The blue-colored CNTs in (b) illustrate the initial position of CNT forest after the first stage - mechanical bending process. Optical photos showing experimental results after the liquid densification process: (c) without and (d) with the two-stage (mechanical bending and liquid densification), self-aligned vertical liquid densification process, respectively. Samples were taken from the same growth batch of CNT forests with identical heights of about $320\mu\text{m}$. Randomly agglomerated CNT chunks were observed in (c) while a continuous CNT film was preserved in (d).

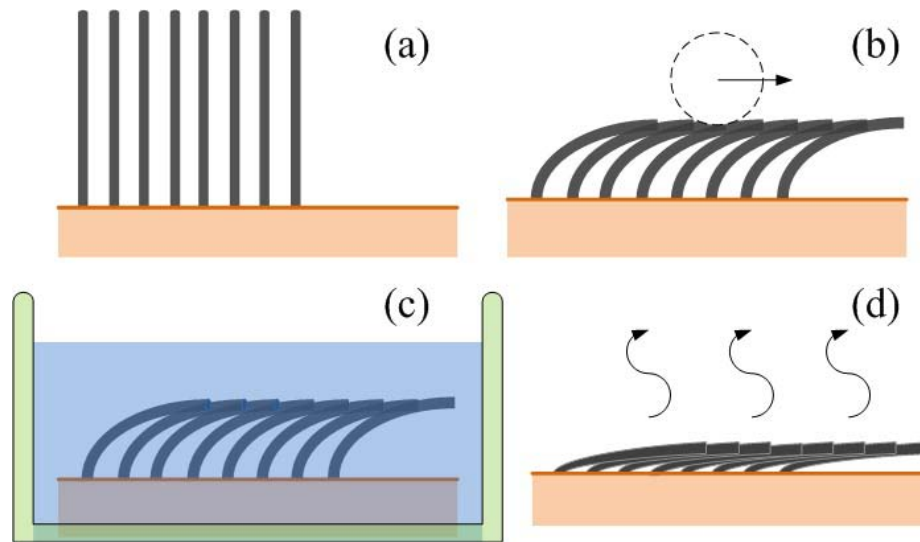


Figure 5.8. The two-stage, self-aligned vertical densification process for CNT forest on a silicon substrate. (a) CVD growth of CNT forest; (b) mechanical bending by using a roller; (c) dipping samples into liquid and (d) air dry.

The detailed process steps are shown in figure 5.8. First, the as-grown $320\mu\text{m}$ -thick CNT forest was synthesized on top of a silicon substrate using the thermal CVD method as illustrated in figure 5.8(a). CNTs were tangled to each other due to the strong van der Waals force and were individually in contact with the silicon substrate. The diameter of CNTs in the prototype experiment is about 20nm . In figure 5.8(b), a rod made of elastomer was used to roll over the CNT forest gently to create the initial downward deformation without the need to apply a strong force. Afterwards, the samples were dipped into liquid for about one hour as illustrated in figure 5.8(c). Figure 5.8(d) illustrates the further shrinkage process during the air-dry process. The liquid densification happens as the liquid-gas interface generates strong surface tension force during the liquid vaporization process. SEM characterizations of the fabricated samples were performed. Figure 5.9(a) compares the height changes before and after the densification process. The pristine, $320\mu\text{m}$ -thick CNT forest (left side) was seen to collapse into about $21\mu\text{m}$ -thick CNT film (right side). The 16 times height reduction ratio is in-line with Iijima's data [10], where about 20 fold reduction in the lateral dimension was measured. The slightly smaller ratio as obtained in this work can come from two areas: (1) vertical densification of as-grown CNT forest with fixed bottom contacts to the substrate in this work could be more difficult to condense as compared with the lateral densification of CNT forest without fixed bottom contacts in the previous work, and (2) multi-walled CNT forest samples were used in this work while the previous work used single-walled CNT forest samples.

A close view SEM photo of the cross section of the densified CNT forest is shown in figure 5.9(b), where the morphology suggests that the original vertically-aligned CNTs were now laterally-aligned in the horizontal direction. Furthermore, efforts of trying to break off the CNT sheet by using a probe tip can only poke open small areas instead of big pieces. This implies that the contacts between CNTs and the growth substrate were strong and likely preserved during the liquid densification process.

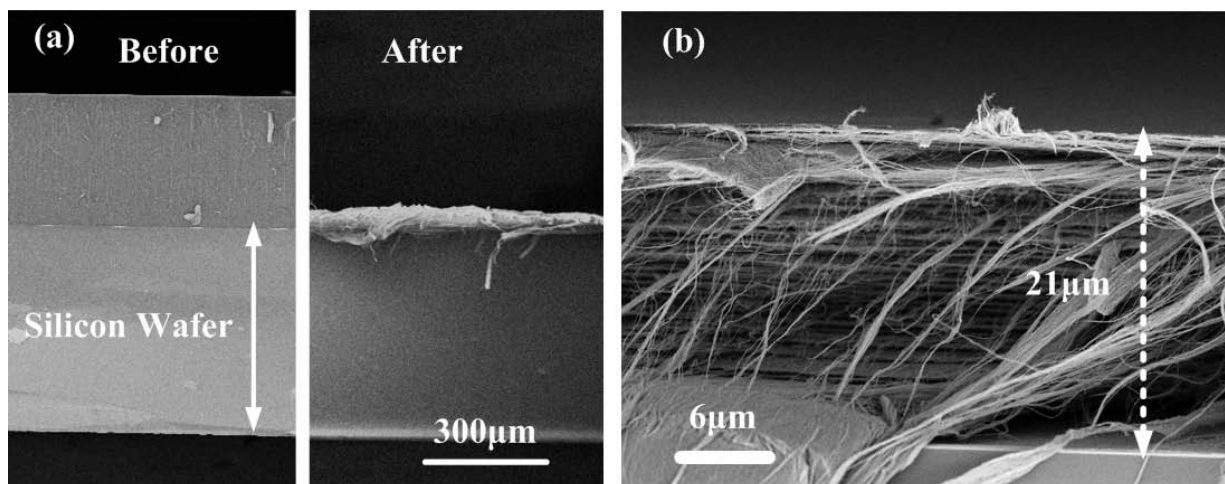


Figure 5.9. SEM photos of the fabricated CNT forests. (a) Contrast pictures before (left side) and after (right side) the two stage, self-aligned vertical densification process of CNT forests. The height of the CNT forest was reduced by about 16 times. The scale bar applies to both photos. (b) Close view SEM photo showing the cross section of the densified CNT forest. The originally vertically aligned CNTs were now laterally-aligned as shown in the horizontal direction.

Figures 5.10(a) and (b) are the top view SEM photos of samples before and after the proposed two-stage, self-aligned vertical densification process, respectively. The as-grown CNT forest is seen to have high-contrast color probably due to uneven top surface with high porosity. The densely packed CNT film, on the other hand, shows more uniform color, implying smoother surface with reduced porosity. Furthermore, the directionality of these CNTs is not distinguishable as the top view SEM photos only illustrate the very top surface of the CNT matrix, which shows randomly distributed CNTs at the top without showing the well-aligned patterns in the cross-sectional view in figure 5.9(b). Figure 5.10(c) is quantitative height results by using different liquids in the densification process. CNTs are intrinsically hydrophobic [15], but both water and less-polar alcohol seem to work well for the densification process. For example, the original height of the CNT forest is $320 \pm 20 \mu\text{m}$. After the densification process in alcohol and water, the newly reduced heights of the CNT forests are 21 ± 5 and $21 \pm 10 \mu\text{m}$, respectively.

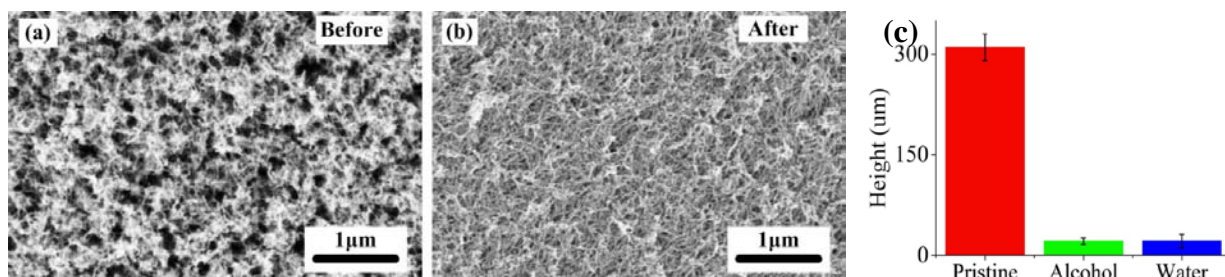


Figure 5.10. (a) and (b) SEM photos showing top views of CNT forest before and after the liquid densification process, respectively. (c) The thickness reduction of CNT forest of pristine CNT forest and after the liquid densification process by using Alcohol and water as the working liquids.

5.2.3 Supercapacitor application

Supercapacitors are surface area-based energy storage devices with possible advantages in high power density, high-cycle counts (millions of times for the charge/discharge cycles), simple configuration and good stability [16-18]. Structures with larger surface area-to volume ration could potentially increase the energy storage density of supercapacitors. Specifically, the energy density is proportional to the specific capacitance by the following equation:

$$E_{SP} = \frac{1}{2} C_{SP} V_{EL}^2 \quad (5-2)$$

where E_{SP} is the energy density, C_{SP} is the volumetric specific capacitance, and V_{EL} is the working voltage, mostly determined by the type of electrolytes used in the energy storage systems. The volumetric specific capacitance is defined as:

$$C_{SP} = \frac{C_{total}}{V} = \frac{(\frac{\epsilon A}{d})}{V} \quad (5-3)$$

where C_{total} is the total capacitance of the device, V is the volume of the electrode, A is the surface area of the electrode, ϵ is the permittivity of the electrolyte and d is the thickness of electrochemical double layer. The latter two parameters are determined by the type of electrolyte used in the system. Therefore, the ways to accomplish high C_{SP} in terms of structural designs include (1) to increase the surface area of the electrode, and (2) to decrease the volume of the electrode. CNT-based supercapacitors have drawn lots of attention recently because CNTs are natural one-dimensional structure with high surface area-to volume ratio [19-20]. The proposed two-stage, self-aligned vertical densification process could further reduce the electrode volume to increase the volumetric specific capacitance. The volume reduction is also favorable for MEMS (Microelectromechanical systems) applications to allow smaller form-factor in packaged systems. Here, supercapacitor electrodes made of the proposed two-stage, self-aligned vertical densification process for CNT forests are characterized.

After the liquid densification process, both as-grown and densified CNT electrodes were experimentally characterized using the 0.1M KOH aqueous electrolyte. A potentiostat, Reference 600 (Gamry Instruments, Inc, Warminster, PA) was used during the tests. Figure 5.11 shows the cyclic voltammetry (CV) curves of the supercapacitor samples on as-grown (light color) and the densified (dark color) CNT forest electrodes, respectively. The total device capacitance, C_{total} , is described by the equation:

$$C_{total} = \frac{dq}{dV} = \frac{I}{(\frac{dV}{dt})} \quad (5-4)$$

where dV/dt is the test setting parameter, 50mV/sec for all the tests, and I is the measured current. Experimental results show that both experiments have similar characteristics with similar current level. Using equation (3), the pristine CNT forest generated a total device capacitance of 8.04mF while the densified CNT forest got a device capacitance at 5.6mF. The slightly current decrease

of the densified sample is probably due to the fact that electrolyte could have difficulty in penetrating inside the highly-packed CNT electrode. This problem can be alleviated by using a vacuum-assisted assembly process to push electrolyte into the CNT matrix as demonstrated previously [21]. Nevertheless, the 16 times volume reduction significantly outweighs the minor reduction in device capacitance. When normalized to the volume (0.25 square centimeters area with 300 μm and 21 μm in height), the specific capacitance for the CNT forest electrodes without and with the densification process were 1.07F/cm³ and 10.7F/cm³, respectively. In other words, supercapacitor electrodes based on the densified CNT forest have about 10-times higher volumetric specific capacitance as compared with those of the pristine CNT forest electrodes. This implies about 10-times improvement in energy density after the densification process. An interesting observation of the CV curves is that the CV curve of the pristine CNT forest shows a pair of small peak (V=0.3V) and valley (V=-0.35V), deviating from the ideally rectangular shape. To our knowledge, only chemical redox reactions could be the reason of such voltage-sensitive current fluctuations. The reacting species could be Al supporting layer and Fe catalyst layer at the substrate. However, when the CNTs were densified, they hindered the electrolyte from accessing the substrate and, therefore, constrained these reactions from happening. This hypothesis agrees with the fact that the peak and valley were obviously suppressed in the densified mode.

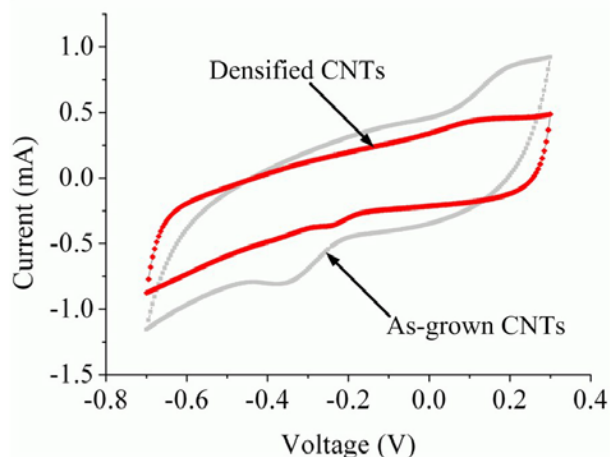


Figure 5.11. Cyclic voltammetry curves of the supercapacitor samples using as-grown (light color) and densified (dark color) CNT forest samples, respectively. Data were collected at 50mV/sec and the electrolyte was 0.1M KOH aqueous solution and the effective electrode area was 5mm \times 5mm for both cases.

Figure 5.12 shows the charge/discharge curves of CNT forest electrodes without (red color) and with (blue color) the two-stage, self-aligned vertical densification process. The abrupt voltage drops at the start of all discharge processes have been observed when the direction of current was reversed (from charge to discharge). This phenomenon is known as IR drops in supercapacitors. Its magnitude is in proportion to the internal resistance (R) of the electrode. For example, a previous work has demonstrated smooth charge/discharge characteristics with minimum IR drops for CNT forest-based supercapacitor electrodes sitting on top of a conductive metal layer [21]. In this work, the IR drops are much bigger as CNT forests are sitting on an insulating oxide layer and the densified sample has a value of 0.12V, which is smaller than those of the as-grown sample at about 0.16V. The 25% resistance deduction has been achieved after the densification process. There are two possibly factors contributing to the reduction of resistance.

First, CNTs are more closely packed after the densification process which could enhance contacts between CNTs to reduce the overall resistance. Second, the charge/discharge process will have current flowing in the lateral direction. These horizontally aligned CNTs as the result of the densification process could provide easier paths than vertically aligned CNTs for reduced resistance.

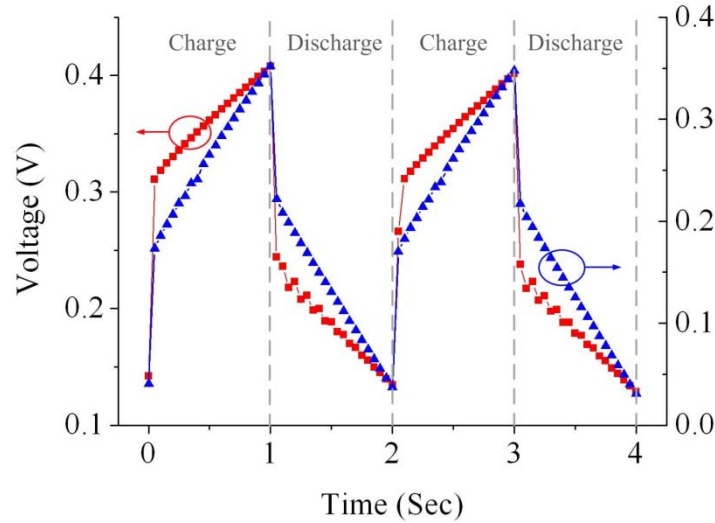


Figure 5.12. Charge and discharge characteristics of CNT forest electrodes using as-grown (red color and left Y axis), and densified electrodes (blue color and right Y axis), respectively. The input current is square-wave with a magnitude of 1mA and a period of 2 seconds. The IR drops happens at the moment that the current direction reverses (start of discharging process) and its magnitude corresponds to the internal resistance of the electrode. The densified CNT electrode has an IR drop of about 0.12V as compared with as-grown CNT forest at 0.16V.

Figure 5.13 shows the cyclic stability tests of the densified CNT forest electrode in the supercapacitor experiments for a total of 50 charge/discharge cycles. It is found that the capacitance of the system gradually increased. This could be the result as discussed earlier that electrolyte may have difficulty in penetrating the densified CNT film and the increased capacitance after multiple charge/discharge processes is probably the result of gradual penetration of electrolyte into the densified CNTs. It is worth pointing out that densified CNTs showed no sign of degradation during the one-hour cyclic tests, implying good structural stability.

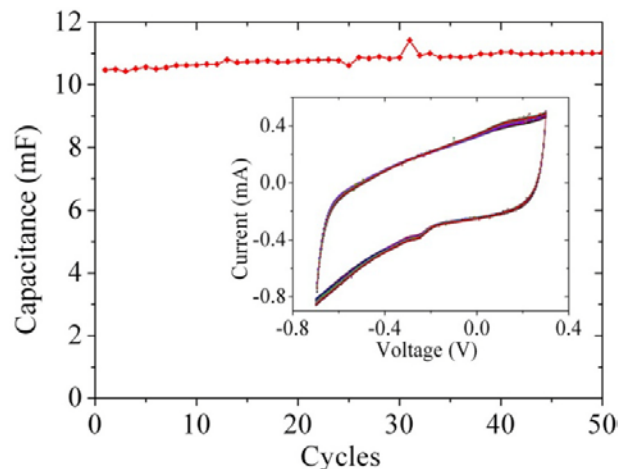


Figure 5.13. Cyclic tests for a densified CNT forest electrode for a total of 50 cycles. The inset shows overlapped cyclic voltammetry curves of the supercapacitor samples and very little changes were observed. Capacitance values at $V = -0.2V$ at each cycle were selected to represent the general capacitance variations.

In a word, a two-stage process combining mechanical bending and liquid densification to make self-aligned, vertical densification of CNT forests has been demonstrated on silicon substrates. A 16-fold height reduction has been achieved on samples with an area of $10\text{mm} \times 5\text{mm}$. One possible application of this method has been demonstrated as the electrode in the supercapacitor. Experimental results showed densified CNT forest electrodes had slightly reduced total capacitances as compared with electrodes from as-grown CNT forest while volumetric specific capacitance increased from $1.07\text{F}/\text{cm}^3$ to $10.7\text{F}/\text{cm}^3$ for densified CNT samples. This implies about 10 times enhancement of energy density of supercapacitor electrodes by using this densification process.

References

- [1] Patrice Simon and Yury Gogotsi, Materials for electrochemical capacitors, *Nature Materials*, 2008, 7, pp.845
- [2] YeoHeung Yun, Vesselin Shanov, Yi Tu, Srinivas Subramaniam, and Mark J. Schulz, Growth Mechanism of Long Aligned Multiwall Carbon Nanotube Arrays by Water-Assisted Chemical Vapor Deposition, *J. Phys. Chem. B*, 2006, 110, pp.23920
- [3] Kenji Hata, Don N. Futaba, Kohei Mizuno, Tatsunori Namai, Motoo Yumura, Sumio Iijima, Water-Assisted Highly Efficient Synthesis of Impurity-Free Single-Walled Carbon Nanotubes, *Science*, 2004, 306, pp.1362
- [4] K. Tohji, H. Takahashi, Y. Shinoda, N. Shimizu, B. Jeyadevan, and I. Matsuoka, Y. Saito, A. Kasuya, S. Ito, and Y. Nishina, Purification Procedure for Single-Walled Nanotubes, *J. Phys. Chem. B*, 1997, 101, pp.1974
- [5] O. Yaglioglu, R. Martens, A. John Hart, A.H. Slocum, Conductive carbon nanotube composite microprobes, *Adv. Mater.*, 2008, 20, pp.357
- [6] Z. Yang, L. Ci, J.A. Bur, S. Lin, P.M. Ajayan, Experimental observation of an extremely dark material made by a low-density nanotube array, *Nano Lett.*, 2008, 8, pp.446

- [7] <http://en.wikipedia.org/wiki/Graphite>
- [8] B.E. Conway, *Electrochemical supercapacitors: scientific fundamentals and technological applications*, Kluwer Academic/Plenum Publishers, New York, 1999.
- [9] M. Lu, M. Jang, G. Haugstad, S.A. Campbell, T. Cui, Well-aligned and suspended single-walled carbon nanotube film: directed self-assembly, patterning, and characterization, *Appl. Phys. Lett.*, 2009, 94, pp.261903
- [10] D.N. Futaba, K. Hata, T. Yamada, T. Hiraoka, Y. Hayamizu, Y. Kakudate, O. Tanaike, H. Hatori, M. Yumura, S. Iijima, Shape-engineerable and highly densely packed single-walled carbon nanotubes and their application as super-capacitor electrodes, *Nat. Mater.*, 2006, 5, pp.987
- [11] Y. Hayamizu, T. Yamada, K. Mizuno, R.C. Davis, D.N. Futaba, M. Yumura, K. Hata, Integrated three-dimensional microelectromechanical devices from processable carbon nanotube wafers, *Nat. Nanotechnol.*, 2008, 3, pp.289
- [12] D. Wang, P. Song, C. Liu, W. Wu, S. Fan, Highly oriented carbon nanotube papers made of aligned carbon nanotubes, *Nanotechnology*, 2008, 19, pp.075609
- [13] Y. Jiang, L. Lin, Densely packed carbon nanotube forest on silicon substrate for MEMS supercapacitor applications, in: Proceedings of *IEEE Transducers'11*, Beijing, China, June 5-9, 2011
- [14] Y. Jiang, P. Wang, L. Lin, Characterizations of contact and sheet resistances of vertically aligned carbon nanotube forests with intrinsic bottom contacts, *Nanotechnology*, 2011, 22, pp.365704.
- [15] K.K.S. Lau, J. Bico, K.B.K. Teo, M. Chhowalla, G.A.J. Amaratunga, W.I. Milne, G.H. McKinley, K.K. Gleason, Superhydrophobic carbon nanotube forests, *Nano Lett.*, 2003, 3, pp.1701
- [20] E. Frackowiak, F. Beguin, Carbon materials for the electrochemical storage of energy in capacitors, *Carbon*, 2001, 39, pp.937
- [21] A.G. Pandolfo, A.F. Hollenkamp, Carbon properties and their role in supercapacitors, *J. Power Sources*, 2006, 157, pp.11-27.
- [22] P. Simon, Y. Gogotsi, Materials for electrochemical capacitors, *Nat. Mater.*, 2008, 7, pp.845
- [23] K.H. An, W.S. Kim, Y.S. Park, Y.C. Choi, S.M. Lee, D.C. Chung, D.J. Bae, S.C. Lim, Y.H. Lee, Supercapacitors using single-walled carbon nanotube electrodes, *Adv. Mater.*, 2001, 13, pp.497
- [24] V.L. Pushparaj, M.M. Shaijumon, A. Kumar, S. Murugesan, L.J. Ci, R. Vajtai, R.J. Linhardt, O. Nalamasu, P.M. Ajayan, Flexible energy storage devices based on nanocomposite paper, *Proc. Natl. Acad. Sci.*, 2007, 104, pp.13574
- [25] Y. Jiang, P. Wang, L. Lin, 3D supercapacitor using nickel-electroplated vertical aligned carbon nanotube array electrode, in: Proceedings of *IEEE MEMS 2010*, Hong Kong, China, January 24-28, 2010

Chapter 6 Conclusions and future works

6.1 Conclusions

CNT forest-based supercapacitor electrodes have been studied in this work in four progressing stages to increase the energy density and system performance. First, single layer, interdigital pristine CNT forests have been used as supercapacitor electrodes as detailed in Chapter 3. Second, CNTs forests with embedded nickel nanoparticles have been studied as supercapacitor electrodes in Chapter 4. Third, ultra-long CNT forests electrodes have been characterized in Chapter 5. Forth, densified CNT forests electrodes have been proposed and demonstrated in Chapter 5.

The fundamental knowledge on the syntheses and properties of CNTs as well as working principles of supercapacitors has been introduced in Chapter 1. Specifically, common electrode materials of supercapacitors have been discussed. CNT forests could potentially provide large surface area to increase the energy density of supercapacitors such that they were chosen as the electrode materials in this work. The possibility to construct CNT forests electrodes with high bulky conductivity and low contact resistance provides further motivations for the study.

The syntheses and characterizations of the CNT forests as the electrode material for supercapacitors have been discussed in details in Chapter 2. These include comprehensive studies on the sheet and contact resistances with four distinct designs: (1) the transfer length method (TLM), (2) the contact chain method, (3) the Kelvin method, and (4) the four point probe method. Experimental results show that devices based on stripe-shaped CNT forests 100 μm in height and 100 μm in width have a sheet resistance of approximately 100 Ω/\square . The corresponding specific contact resistance to the molybdenum layer is roughly $5 \times 10^4 \Omega \cdot \mu\text{m}^2$. Consistency of the results from the four different methods validates the study. Furthermore, after two months of storage of CNT forest samples in open air, less than 0.9% resistance deviations were observed. Based on the results, I conclude that the current CNT synthesis process is reliable and consistent, and provides a low contact resistance. Therefore, it is suitable to act as electrodes of the supercapacitors.

In the first development stage of CNT forests electrodes, MEMS planar supercapacitors with the design of interdigital electrodes have been demonstrated utilizing pristine and highly porous CNT forests. Conductive substrates have been built by using the combination of Mo/Al/Fe metal stack layer for both good CNT forest synthesis and high electrical conductivity. Prototype devices have shown measured specific capacitances about 1000 times higher than those with plain metal electrodes without CNT forests. Furthermore, repeated charging/ discharging experiments show over 92% efficiency and robust cycling stability. I conclude that, as the first generation of MEMS supercapacitors, CNT forests have exerted their outstanding material advantages as expected and retained the common features of supercapacitor electrodes. Next step may be to discover the scientific reason of the success of the Mo/Al/Fe recipe and analyze what kind of role each metal plays. By doing so, we may discover a new substrate recipe with even lower internal resistance, which reduces the energy loss, another perspective to “increase” the energy density.

In Chapter 4, the second development stage of CNT forests electrodes emphasizes on the study of pseudo supercapacitors by using nickel-decorated CNT forests electrodes. Synthesis of nickel nanoparticles in as-grown CNT forests has been realized by using a vacuum infiltration method to overcome the hydrophobicity of CNTs. Experimental results show that nickel nanoparticles have been deposited uniformly within an 80 μm -high CNT forest structure by means of electroplating with average size of 30nm to 200nm in diameter which was controlled by the deposition chemistry, current density and time. These CNT forests electrodes with embedded nickel nanoparticles have measured electrochemical capacitance about one order of magnitude higher than those CNT forests electrodes without nickel nanoparticles. Furthermore, no visual morphologic change has been observed on the nanoparticles after 1000 cycles of cyclic voltammetry tests. From the results, I conclude that the pseudo capacitance has been successfully demonstrated on CNT forests. The vacuum infiltration-assisted electroplating method is a feasible and flexible tool to functionalize high aspect ratio nanomaterial beyond CNT forests and could find opportunities in other applications where functionalized nanomaterial is needed.

The third and fourth development stages for the CNT forests electrodes have been described in Chapter 5 to further improve the energy density of supercapacitors using ultra-long CNT and densified CNT forests electrodes, respectively. CNT forests were grown up to millimeter-level in thickness using the water-assisted CVD growth. Experimental results have confirmed that the capacitances of supercapacitors have been further increases roughly in proportion to the increment of the height of CNT forests. I conclude that preliminary success has been done on the synthesis of long CNT. However, the CNT growth on Mo/Al/Fe substrate is not as impressive on that on Al/Fe (300 μm vs. 3mm). In next step, we need once again to understand the role of metals and figure out a way to take full use of their advantages while preventing the negative impacts. Densified CNT forests electrodes were then introduced by a two-stage, self-aligned liquid densification process. By combining mechanical bending and liquid densification process, the vertical height of a 10mm \times 5mm in size, as-grown CNT forest collapsed from 320 μm to 21 μm in the prototype experiments. The densified CNTs maintained the film continuity and the self-alignment configuration as the CNT-silicon bottom contacts were preserved. Experimental results show densified CNT forest samples had slightly reduced total capacitances as compared with samples using as-grown CNT forests. However, the volumetric specific capacitance increased from 1.07F/cm³ to 10.7F/cm³ due to the shrinkage in total volume. From the observation, I conclude this method is a clear success not only in term of results but the explanation of the mechanism. An easy next step may be to combine stage 2 and stage 4, that is, the functionalization of densified CNT forests. The shrunken space between CNTs may impose challenge on local depletion of metal ions more often but improved mechanical property, on the other hand, may be good benefit.

In conclusion, CNT forests have been synthesized and characterized as electrodes for supercapacitors. The four development stages with different approaches all have reached the common goal, to enhance energy density of the supercapacitors, by times or even orders. Together, the four development stages have systematically explored the feasibility and opportunities of CNT forests electrodes for possible applications in supercapacitors.

6.2 Future directions

6.2.1 Integration for complete energy storage systems

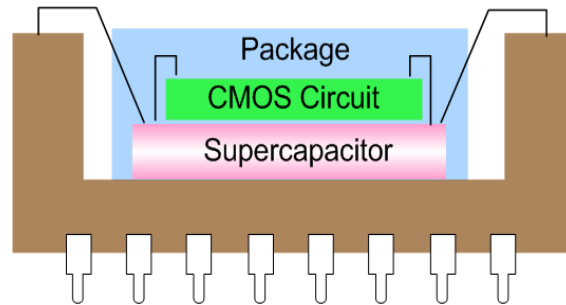


Figure 6.1. Schematic diagram of a complete and self-sustainable system using CNT forests electrodes in miniaturized supercapacitors to store energy possibly generated from MEMS energy harvesters. CMOS circuits could also include MEMS energy harvesters for energy generation, regulation to provide power for other system functionalities.

The study in this thesis focuses on CNT forests electrodes for supercapacitors and one future direction is to build on-chip energy storage systems. For example, it is reasonable to build an energy storage system including other parts such as energy harvesting components and power management circuits. There are existing energy harvesting systems built at relatively large scale [1, 2]. Therefore, the integration of those components together with the CNT supercapacitor on a single chip could result in a complete and self-sustainable system. Flip-chip method [3] may be considered to realize such a system-on-package (SOP) configuration as illustrated in Figure 6.1.

6.2.2 Flexible energy storage systems

In order to accommodate various application environments, it could be desirable to transfer CNT forests onto a flexible substrate. During experiments, it is found that the patterned CNT forests with the bottom Mo/Al/Fe metal layers are easily detached with the silicon substrate in water. One possible next step is to select a proper flexible substrate to firmly adhere the CNT forest film. Figure 6.2 illustrates a possible configuration of a flexible supercapacitor. In this configuration, the conventional sandwiched supercapacitor structure is illustrated. Densified CNT forests, as discussed in Chapter 5, might be preferred here as the densification process improves mechanical strength and prevent further deformation of the shape of CNT forests. The flexible electrolyte sheet can be realized by electrolyte-soaked polymer separator or solid (e.g. organic) electrolyte. The flexible supercapacitor structure can be further tailored in specific size and shape according to application requirements.

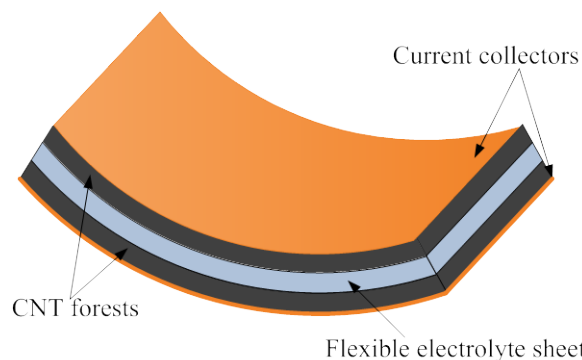


Figure 6.2. Schematic of a flexible CNT supercapacitor

6.2.3 Three dimensional CNT battery

While supercapacitors are simple with high power density, a micro battery with high energy density is preferred in many applications. The CNT forests electrodes with embedded nickel nanoparticles as reported in Chapter 4 are actually already close to the battery concept. For example, one might replace nickel hydroxide nanoparticles with battery-oriented materials. Possible candidates are: (1) silicon for Li-ion battery [4]; and (2) Ni and Zn metal (to realize Ni-Zn battery [5, 6]). In both cases, CNTs act as supporting backbones to collect and transport charges. It is noted that the advantage of the demonstrated electroplating process is the possibility to selectively deposit different nanomaterials in different regions utilizing voltage for local depositions. One example is illustrated in Figure 6.3 which has CNT forests deposited with two kinds of nanomaterials as cathodes and anodes, respectively for possible battery applications. Actually we are already on the way of making a real 3D battery. In Chapter 4, Zinc was electroplated on CNT forests. Appendix C presents our exploration on Silicon deposition on CNT forests.

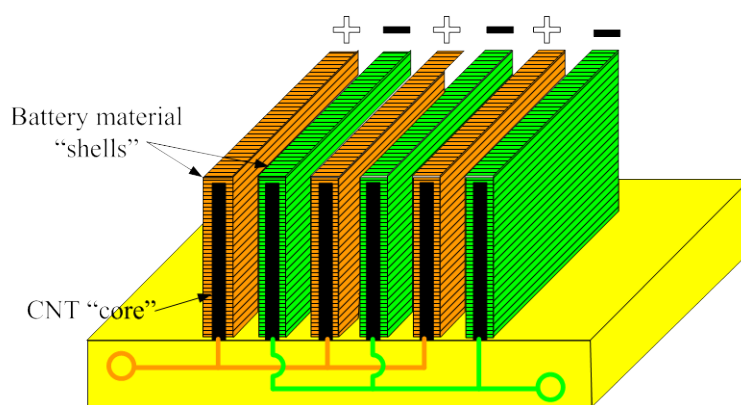


Figure 6.3. Three-dimensional CNT battery. The “walls” of CNTs are coated with different battery materials represented by orange and green colors, respectively. Selective depositions may be realized by applying voltage locally during an electroplating process.

6.2.4 Applications beyond supercapacitors

Knowledge and process tools on CNT forests have been developed to synthesize CNT forests with thickness ranging from 2 to 3000 μm . Other associated processes have also been established

in this work. These include: (1) techniques to uniformly decorate nanomaterials within the dense CNT forests; and (2) densification process to change the shape of the CNT forests network to be densely packed. These processes can be the foundations for other research projects, including as the basic building blocks for new MEMS devices such as MEMS cantilevers, resonators and other microstructures.

References

- [1] Rajeevan Amirtharajah and Anantha P. Chandrakasan, Self-Powered Signal Processing Using Vibration-Based Power Generation, *IEEE Journal of Solid-State Circuits*, 1998, 33(5), pp.687
- [2] M.E. Glavin, Paul K.W. Chan, S. Armstrong, and W.G Hurley, A Stand-alone Photovoltaic Supercapacitor Battery Hybrid Energy Storage System, 13th IEEE EPE-PEMC, 1-3 Sept. 2008, Poznan, Poland
- [3] K. Kordás, G. Tóth, P. Moilanen, M. Kumpumäki, J. Vähäkangas, A. Uusimäki, R. Vajtaia and P. M. Ajayan, Chip cooling with integrated carbon nanotube microfin architectures, *Applied Physics Letters*, 2007, 90, pp.123105
- [4] C. K. Chan, H. Peng, G. Liu, K. Mcilwrath, X. F. Zhang, R. A. Huggins, and Y. Cui, High-performance lithium battery anodes using silicon nanowires, *Nature Nanotechnology*, 2008, 3, pp.31
- [5] James McBreen, Nickel/zinc batteries, *Journal of Power Sources*, 1994, 51, pp.37
- [6] Paul H. Humble, John N. Harb, and Rodney LaFollette, Microscopic Nickel-Zinc Batteries for Use in Autonomous Microsystems, *Journal of The Electrochemical Society*, 2001, 148(12), pp.A1357

Appendix A CNT forest synthesis platform

The CNT samples in this study were synthesized using CVD method. Detailed theory and optimization procedure can be found in Chapter 1 and 2, respectively. Here we present how to build the practical system. As shown in figure A.1, the system can be divided into four parts.

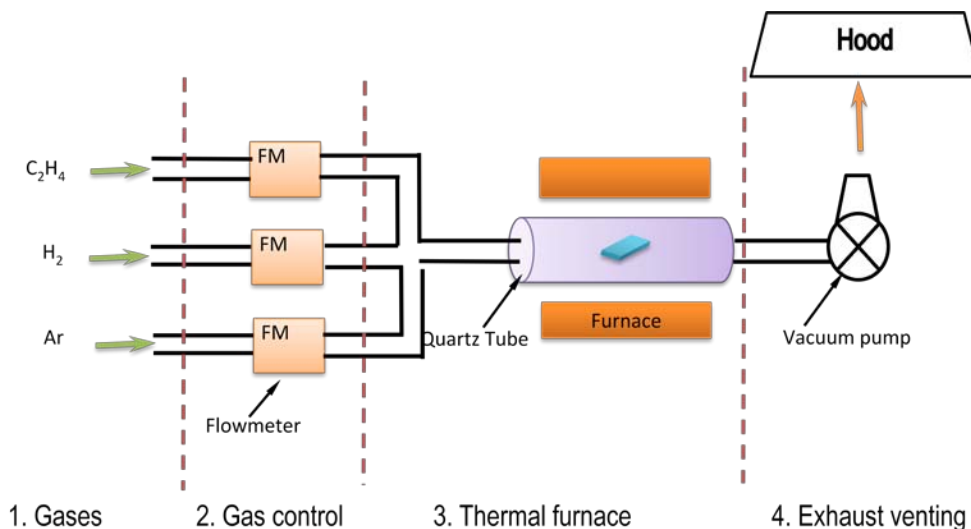


Figure A.1. Schematic of a CNT Synthesis System

A.1 Gases

Gases were purchased from Praxair Inc. There is no oxidizing gas used in the system so all cylinders can be placed together as shown in figure A.2.

- H_2 : K-type cylinder of Hydrogen gas (D1869345 102, K 196CF), 5.0 ultra high purity
- C_2H_4 : 99% or higher purity
- Ar: ARHY2C-K K-type cylinder of Argon/2%Hydrogen, certified



Figure A.2. Gases used in the experiments

A.2 Gas control

There are two generations of flowmeter that have been used as seen in figure A.3. The current version is digital.

(1) Mechanical: Purchased from Matheson Tri-Gas

- Type: High Accuracy - Model FM-1050
- Tube model: E100 (B)
- Part code: E1-4C251-E100

(2) Digital: Smart Trak 2 Model 100 Mass Flow Meters, Sierra Instruments, Inc.

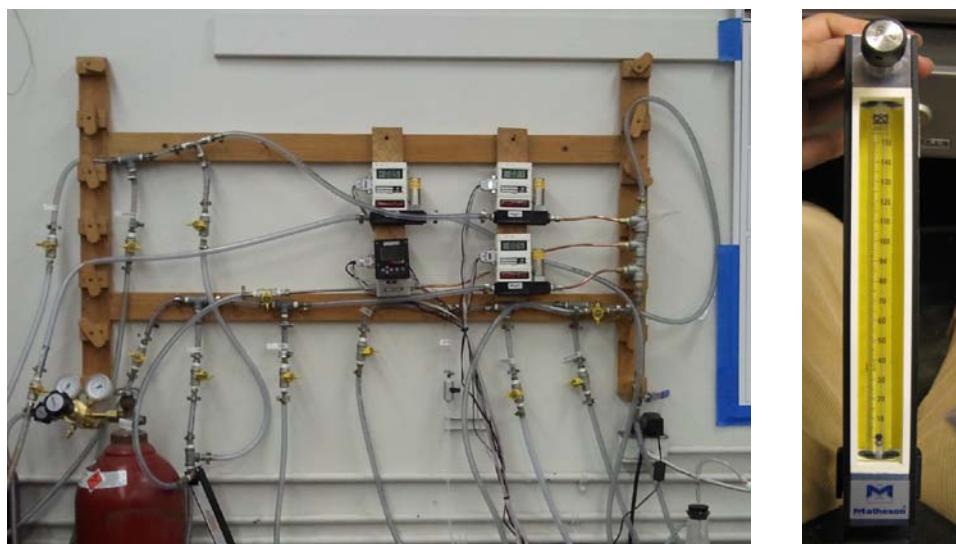


Figure A.3. Two types of flowmeter used in this study: current digital (left) and mechanical one (right).

A.3 Thermal furnace and vacuum pumps

The thermal CVD furnace (Lindberg/Blue M[®] three-zone tube furnace, Thermo Electron Corp., Asheville, NC) is shown in figure A.4. A specially-designed 6ft long and 2-inch in diameter quartz tube (National Scientific Co.) is the reaction chamber with both ends to be sealed during the growth. The quartz tube is intentionally made double the length of the furnace such that, during the cooling period, the whole heated section of the tube could be pulled out of the furnace and blown to a low temperature with fan quickly while the tube, as a whole, are not required to remove from the furnace. Samples were always placed at the very middle of the furnace to guarantee the best temperature uniformity. The sample loading and fabricated samples are shown in figure A.5. A vacuum pump (Welch Direct-Drive High Vacuum Pumps - Model 8907, Welch Allyn) used to purge the tube before loading carbon precursor and opening the heated tube.



Figure A.4. Thermal furnace loaded with a 2-inch quartz tube. The fan on the right side of the furnace is used to cool the 720°C tube into a temperature below 200°C within 10min.

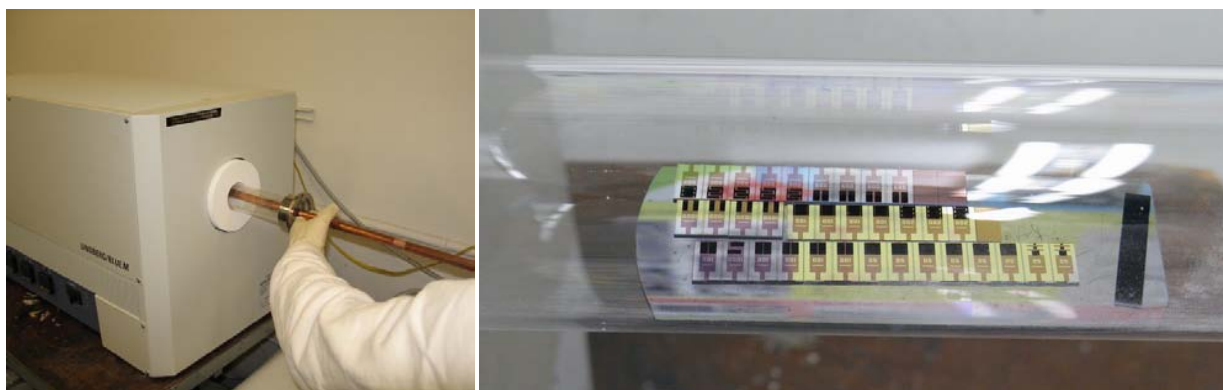


Figure A.5. Sample loading (left) and the grown CNT samples before unloading (right). A claw at the end of the loading rod was made to grab the boat during pushing in and pulling out. A reference sample (at the end of the silicon boat on right figure) is highly recommended as a reference to monitor the process stability.



Figure A.6. Vacuum pump to purge the tube

Appendix B Process flows of CNT supercapacitors

B.1 Pristine CNT electrodes

B.1.1 Process flow

| Step | Process | Equipment | Specifications/Ccomments |
|-----------------|---------|--------------------|--|
| S1 | PR SPIN | SVGCoat2 | 5 wafers, 1.3um G-line (5000 rpm). Soft bake hot plate 60s at 90°C. Chill plate 6s. |
| S2 | PR EXP | KSaligner | 5 wafers, Dummy mask, proximity mode, expose 30second |
| S3 ⁺ | PR SPIN | Svgcoat2 | 5 wafers, 1.1um I-line (4100 rpm). Soft bake hot plate 60s at 90°C. Chill plate 6s. |
| S4 | PR EXP | KSaligner | 5 wafers, Electrode mask, 20s, hard contact mode |
| S5 | PR DEV | SVGdev | Try one or two first before the rest wafers, Standard I-line develop, no bake |
| S6 | CHECK1 | Microscope check | |
| S7 | DEP | Edwardseb3 | 3 wafers, Mo: 50nm; Al: 10nm; Fe: 5nm; Temperature never go beyond 100°C due to the PR existence |
| S8 | LIFTOFF | Sink 432C | Lift off all three wafers with ultrasonic |
| S9 | PR SPIN | SVGCoat2 | Coat protective layer for dicing |
| S10 | DICING | Wafersaw | See Section B.1.3 |
| S11 | CLEAN | Sink 432C | Acetone+IPA+DI wafter |
| S12 | CVD | CVD furnace in lab | Standard recipe as table 2.1 in Chapter 2 |
| S13 | CHECK2 | Leo check | |

* Because edwardseb3 (e-beam evaporation) can handle 3 wafer at one time. We always use three wafers in a batch to maximum the productivity. It is recommended to have one or two reference (dummy) wafers as well.

+ To get the best results in lift-off (no metal residue on the edge), “G & I-Line Bi-Layer Method” in MOD18 is used, which requires lithography twice. (<http://nanolab.berkeley.edu/labmanual/chap1/1.3processmods.pdf>)

B.1.3 Wafer dicing guide

The numbers on the figure B.2 are the recommended dicing sequence. Lower numbers are diced first. To make the cleaning easy, do not cut through the wafer. Leave about 80 μ m silicon uncut on the wafer.

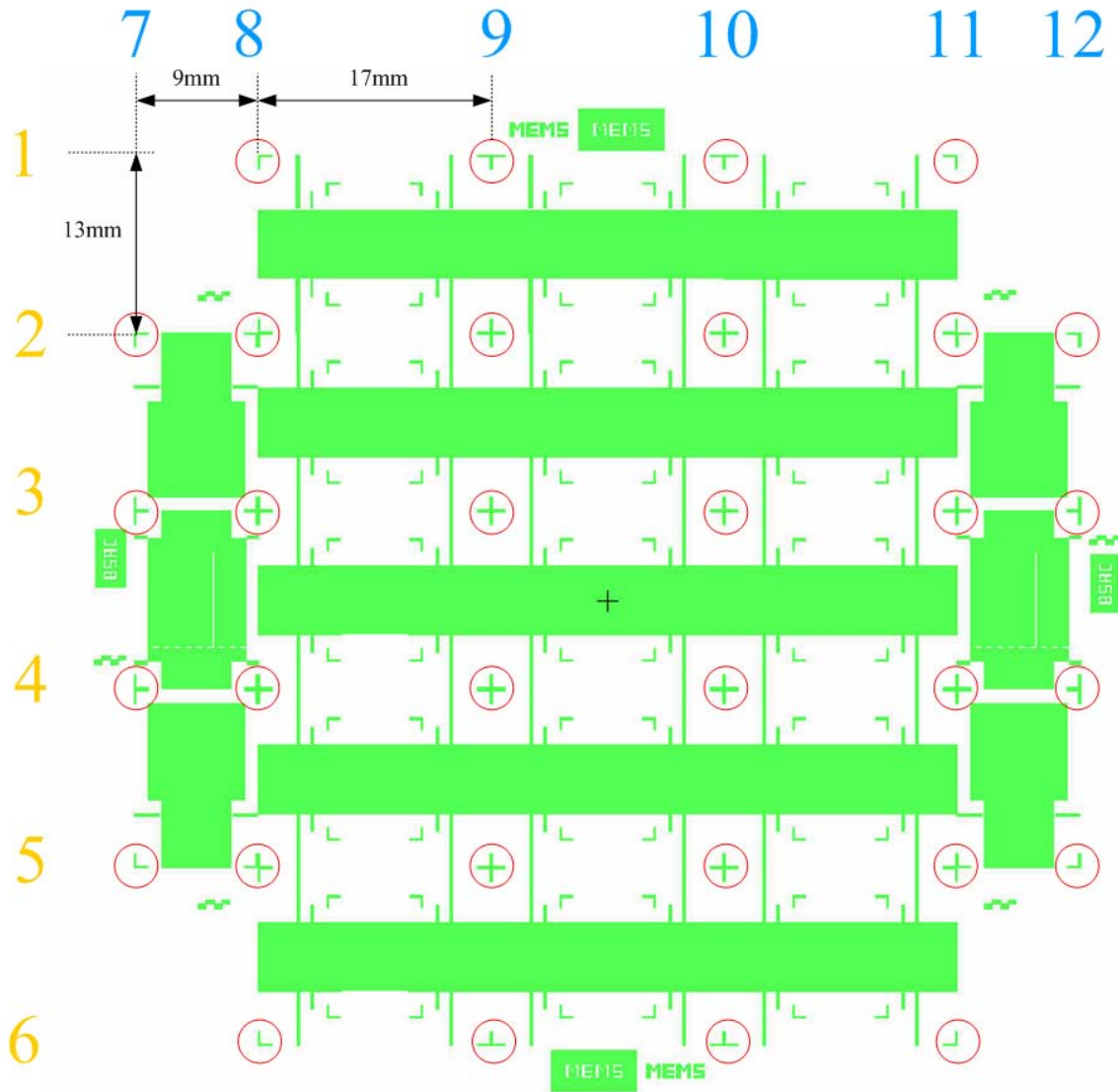


Figure B.2. Dicing guide of MEMS supercapacitors using pristine CNTs (the 1st stage)

B.2 Functionalized CNT electrodes

B.2.1 Process flowchart

| Step | Process | Equipment | Specification/comment |
|------|---------|------------------|--|
| S0 | OXIDE | Tystar3 | 1000-2000Å thermal oxide* |
| S1 | PR SPIN | SVGCoat2 | 5 wafers, 1.3um G-line (5000 rpm). Soft bake hot plate 60s at 90°C. Chill plate 6s. |
| S2 | PR EXP | KSaligner | 5 wafers, Dummy mask, proximity mode, expose 30second (flood expose) |
| S3 | PR SPIN | Svgcoat2 | 5 wafers, 1.1um I-line (4100 rpm). Soft bake hot plate 60s at 90°C. Chill plate 6s. |
| S4 | PR EXP | KSaligner | 5 wafers, Mask I (Mo layer), 20s, hard contact mode |
| S5 | PR DEV | SVGdev | Try one or two first before the rest wafers, Standard I-line develop, no bake |
| S6 | CHECK1 | Microscope check | |
| S7 | DEP | Edwardseb3 | 3 wafers, Mo: 50 or 80nm; Temperature never go beyond 100°C due to the PR existence |
| S8 | LIFTOFF | Sink 432C | Lift off all three wafers with ultrasonic |
| S9 | PR SPIN | SVGCoat2 | 5 wafers (2 dummy wafers+3 wafer from S8), 1.3um G-line (5000 rpm). Soft bake hot plate 60s at 90°C. Chill plate 6s. |
| S10 | PR EXP | KSaligner | 5 wafers, Dummy mask, proximity mode, expose 30second (flood expose) |
| S11 | PR SPIN | Svgcoat2 | 5 wafers, 1.1um I-line (4100 rpm). Soft bake hot plate 60s at 90°C. Chill plate 6s. |
| S12 | PR EXP | KSaligner | 5 wafers, Electrode mask, 20s, hard contact mode |
| S13 | PR DEV | SVGdev | Try one or two first before the rest wafers, Standard I-line develop, no bake |
| S14 | CHECK1 | Microscope check | |
| S15 | DEP | Edwardseb3 | 3 wafers, Al: 10nm, Fe: 5nm; Temperature never go beyond 100°C due to the PR existence |

| | | | |
|-----|---------|--------------------|---|
| S16 | LIFTOFF | Sink 432C | Lift off all three wafers with ultrasonic |
| S17 | PR SPIN | SVGCoat2 | Dicing protective layer |
| S18 | DICING | Wafersaw | See Section B.2.3 |
| S19 | CLEAN | Sink 432C | Acetone+IPA+DI wafer |
| S20 | CVD | CVD furnace in lab | Standard recipe as table 2.1 in Chapter 2 |
| S21 | CHECK2 | LEO check | |

* Si_3N_4 was once tried as the substrate but Mo has a poor adhesion on it such that Mo layer can be easily peeled off during the ultrasonic lift off step.

B.2.2 Parameter settings in e-beam evaporation

The parameters used in the machine (edwardseb3) setting is listed below:

Table B.1. Constant settings used in e-beam evaporation*

| | Density [$\text{g}\cdot\text{cm}^{-3}$] | Z Value | Tool factor | Typical evaporation current [mA] | Typical deposition speed [nm/s] |
|-----------------|---|---------|-------------|----------------------------------|---------------------------------|
| Mo | 10.2 | 34.3 | 0.8 | 160 | 0.33-0.37 |
| Al ⁺ | 2.70 | 8.2 | 0.8 | 30 | 0.04-0.07 [#] |
| Fe | 7.86 | 25.3 | 0.8 | 15-45 | 0.01-0.03 |

* Material properties (the first three columns) are from edwardseb3 manual. Other sources may provide slightly different numbers but these are recommended since they are directly from the manufacturer.

+ The evaporation process of Al often results in the crucible cracking after two or three time usage. It is caused by the interaction between Al and graphite and can only be fundamentally solved by purchasing a metal crucible.

For first time use of new target, 20mA is enough to generate a speed of 0.0-0.08nm/s

B.2.3 Wafer instruction and dicing guide

The green color is the Mo mask and blue color is the Al/Fe mask. Area I is for test structures. Area II is used for material characterization. Area III is the supercapacitor layout with design variations.

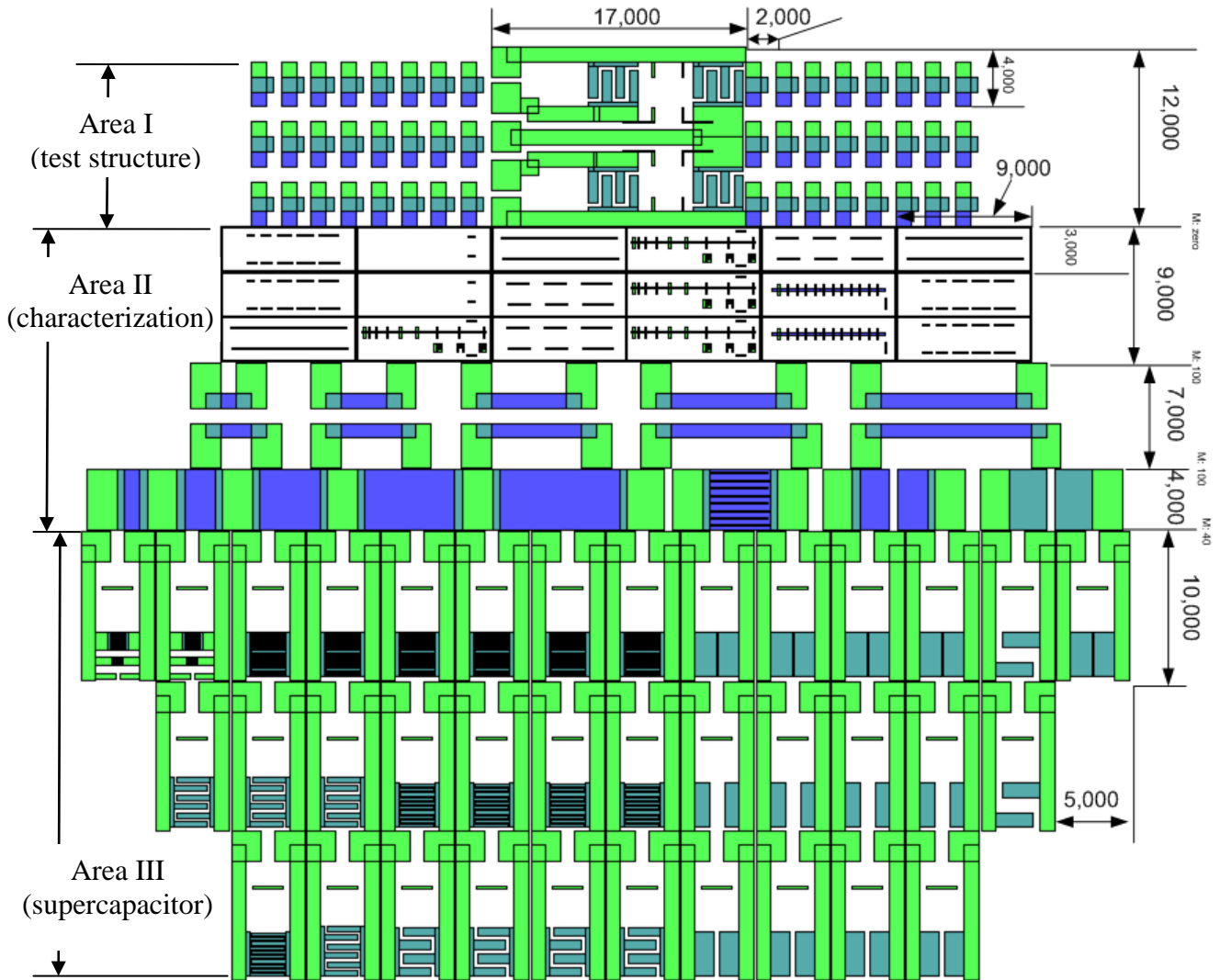


Figure B.3. Layout overview of MEMS supercapacitor using functionalized CNTs

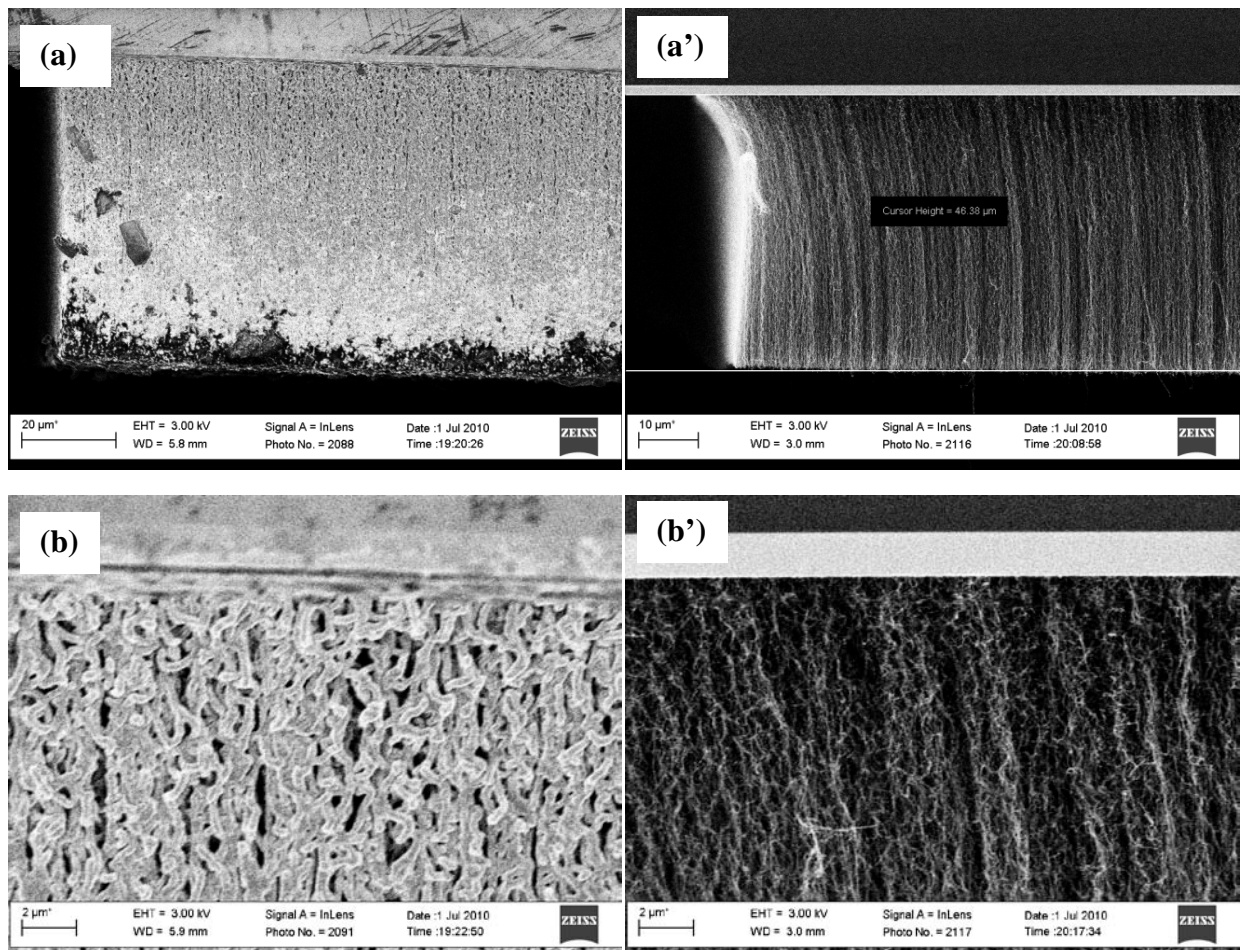
Appendix C Silicon-coated CNT forest using LPCVD

The results here are from the collaborative works with PhD candidate, Mr, Wei-chang Li in Prof. Clark Nguyen's group. The purpose of the project is to develop MEMS RF resonators using CNT forests as building materials.

C.1 Deposition on thick CNT forests

The LPCVD (low pressure chemical vapor deposition) process was done using the standard recipe of Tystar 16 in Berkeley Nanolab. The deposition time runs from 15mins to two hours.

Figure C.1 shows a set of SEM pictures of the amorphous silicon-coated CNT samples with a height of about 60 μm . The right column is the counter parts of a reference CNT sample without silicon coating at roughly the same scale. The pictures show that LPCVD is able to penetrate the 60 μm thick CNT film, though the deposition is thicker near the surface and attenuate as it goes deeper into the inside. It is understandable as the silicon keep being consumed along its path moving inside.



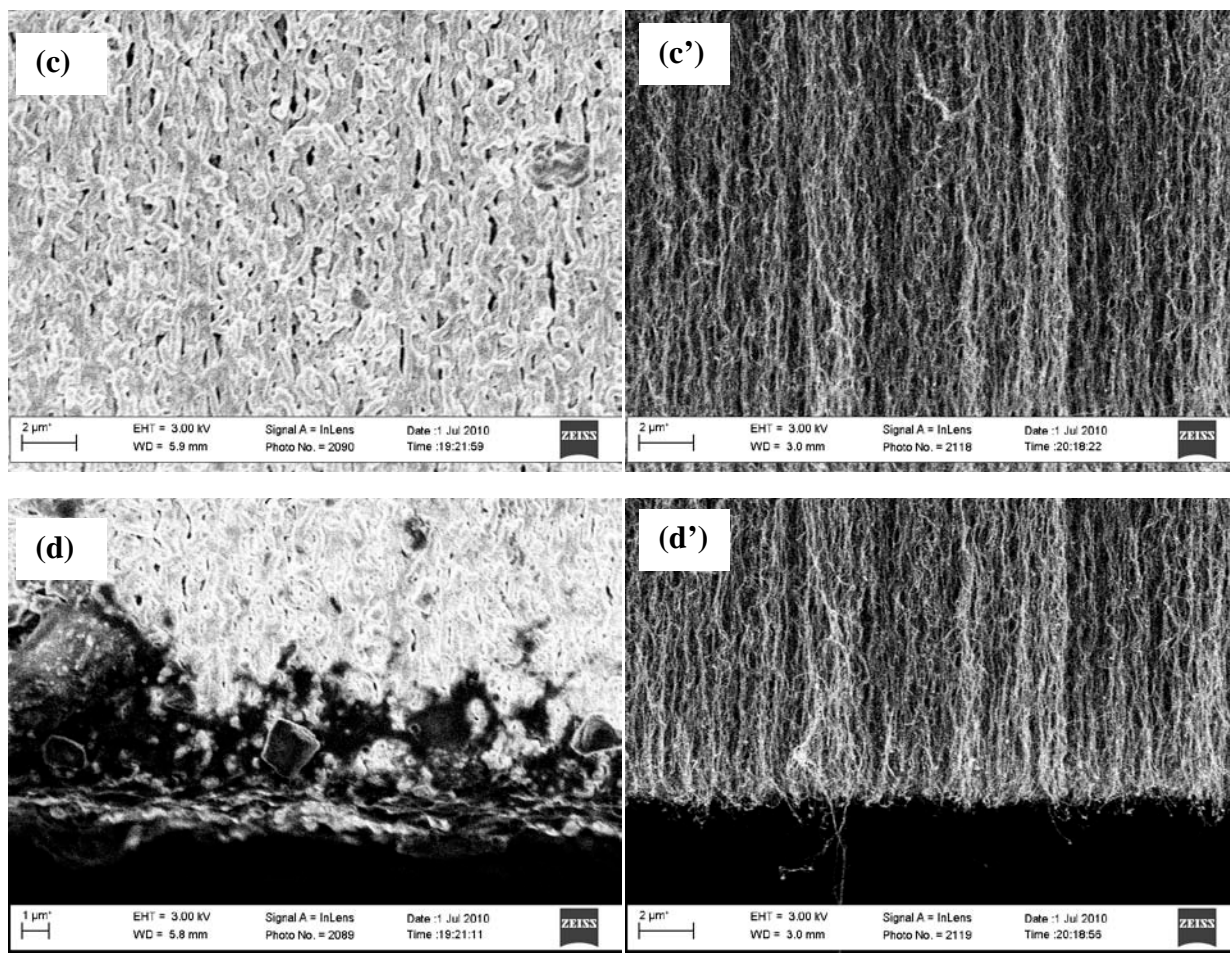


Figure C.1. Silicon-coated 60μm-high CNT forest. (a) Overview; (b)-(d) cross section view of the bottom, middle and top areas of (a). (a')-(d') are the counterpart pictures of a reference CNT sample without silicon coating.

C.2 Deposition on shallow CNT forests

Figure C.2 shows the thickness tuning on $2\mu\text{m}$ -thick shallow CNT forests by adjusting the LPCVD deposition time. The forest was seen to change from porous network to a solid nanocomposite. As long as the CNT is shallow, the uneven thickness issue is not apparent. Figure C.2(d) shows the silicon-coated MEMS structure with $1\mu\text{m}$ gap. The profile looks to be preserved well.

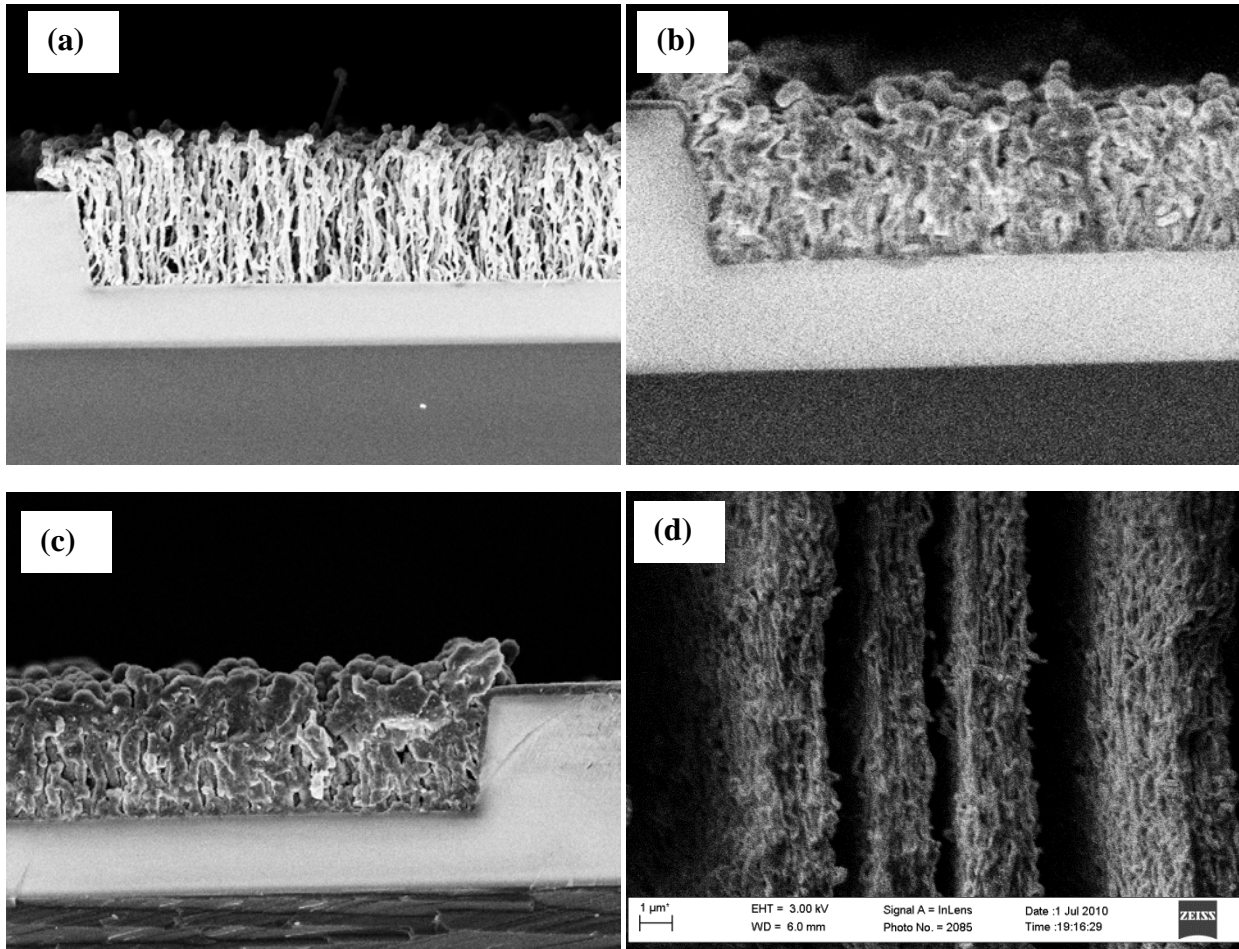


Figure C.2. Poly-Si thickness tuning by changing the deposition time: (a) 1hr, (b) 2hr, and (c) 3hr. The standard recipe of Tystar 16 was used with a deposition rate of about 100nm/hr . (d) is the silicon coating on MEMS structure with $1\mu\text{m}$ gap. CNT profiles are seen to preserve well.